Experiments in Cavity QED:
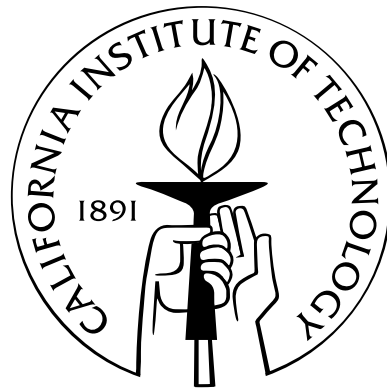# Exploring the Interaction of Quantized Light with a Single Trapped Atom

Thesis by

Andreea Boca

In Partial Fulfillment of the Requirements

for the Degree of

Doctor of Philosophy

California Institute of Technology

Pasadena, California

2005

(Defended May 26, 2005)

ii

Acknowledgements

I would like to thank the people who made this work possible: Jeff, Jason, Dave, Kevin, Russ, Cristoph, Tracy, Joe, Christina, Ron, Win, Kaiwen, James, Theresa, Dominik, Alex, Jun, Dave V., and all other members of the Caltech Quantum Optics Group.

Abstract

The experiments discussed in this thesis focus on the interaction of a single trapped atom with the single mode of a high-finesse optical cavity, in the regime of strong coupling.

Chapter 1 gives a brief introduction, after which Chapter 2 describes our recent measurements of the transmission spectrum of the atom-cavity system. The spectrum exhibits a clearly resolved vacuum-Rabi splitting, in good quantitative agreement with theoretical predictions. A new Raman scheme for cooling atomic motion along the cavity axis enables a complete spectrum to be recorded for an individual atom trapped within the cavity mode, in contrast to all previous measurements of this type that have required averaging over $10^3 - 10^5$ atoms.

Chapter 3 discusses our observations of photon blockade for the transmitted light in the presence of one trapped atom. Excitation of the atom-cavity system by a first photon blocks the transmission of a second one, thereby converting an incident Poissonian stream of photons into a sub-Poissonian, anti-bunched stream, as confirmed by measurements of the photon statistics of the transmitted field. The intensity correlations of the cavity transmission also reveal the energy distribution for oscillatory motion of the trapped atom.

Chapter 4 details a set of simple but necessary measurements of relevant experimental parameters such as cavity geometry, linewidth, mirror properties, birefringence, and detection efficiency. The thesis concludes with Appendix A, describing the efficient laser setup we use for our magneto-optical traps.

Contents

List of Figures

List of Tables

Chapter 1

Introduction

1.1 Brief overview of the experiment

The cavity QED system consists of an atom coupled to a single mode of the elec-
tromagnetic field in a cavity. This system is interesting for a number of reasons.
To start with, it is a simple quantum mechanical entity, reduced to elementary con-
stituents: atoms and photons; thus, it is often possible to predict its behavior with
an easily manageable theoretical model. Also, in the regime of strong coupling, the
rate of interaction between the atom and the field is the dominant parameter in the
problem, meaning that dissipative mechanisms do not wash out the coherent evolu-
tion of the system. In addition, the cavity output consists of a well-defined, single
spatial mode, allowing the photon detection efficiency to be far superior to that in
free-space, hence making cavity QED an ideal platform for the study of quantum
optics. This system also lends itself well to the conversion of stationary qubits of
quantum information, as encoded in long-lived atomic states, into "flying" qubits,
represented by easily-transported photonic states. This makes it an attractive setup
for the implementation of quantum networking and of other quantum information
science protocols.

Our experiment studies the interaction of a single Cesium atom with the quantized
mode of an optical cavity. The heart of the experimental apparatus is the physics
cavity, a 42 μm-long high-finesse Fabry-Perot resonator (see Fig. 1.1). The atom is
localized within the cavity mode by means of an intra-cavity far-off-resonance trapping
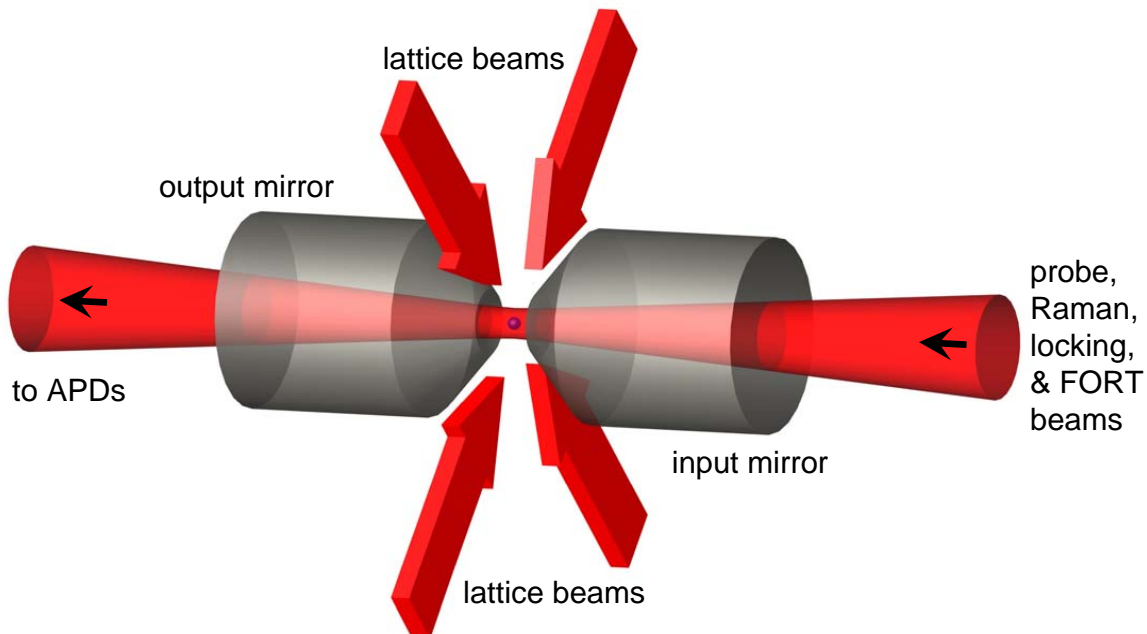
Figure 1.1: Cartoon representation of our experiment, showing the atom and the cavity, as well as the various laser beams illuminating them.

(FORT) beam, essentially forming "optical tweezers" for the atom. The geometry of the cavity, the quality of its dielectric mirrors, and the FORT parameters are such that the rate g of coherent interaction between the atom and the cavity field far exceeds all relevant loss rates due to dissipation. These losses are the cavity decay rate κ, the spontaneous emission rate γ, and the atom loss rate $1/T$ due to a finite trapping lifetime. For our experiment, typical values are $g = 2\pi \times 34$ MHz, $\kappa = 2\pi \times 4$ MHz, $\gamma = 2\pi \times 2.6$ MHz, and $T = 2 - 3$ s, thus $g \gg (\kappa,\ \gamma,\ 1/T)$. This parameter regime is known as strong coupling.

The cavity is locked to a fixed length by monitoring the transmission of a locking beam, which is, like the FORT field, resonantly coupled to the cavity and far detuned from any Cesium transitions, but too weak to alter significantly the trapping potential. Cold atoms are delivered to the intra-cavity FORT by being dropped from a magneto-optical trap (MOT) above the cavity. The falling velocity of the atoms is cooled by two pairs of beams in a $\sigma^+\sigma^-$ optical lattice configuration, which illuminate from the side (i.e., transversely to the cavity axis) the space between the mirrors. Once an

atom is loaded in the FORT, we use lasers to drive the cavity QED system in order to study the atom-field interaction, as inferred from the output photon stream. The driving field can address either the atom, by illuminating the system from the side with lattice or linearly polarized beams, or the cavity, usually by way of a linearly polarized probe beam coupled to one of the longitudinal cavity modes, and near-resonant with a Cesium transition (usually at 852 nm). Scattering the driving field photons typically heats the atom, so in order to maintain a long trapping lifetime, we counteract this effect with various cooling beams. Radial cooling is achieved by the lattice beams, whereas axial cooling is done in a Raman sideband configuration involving a separate beam coupled off-resonantly to the same longitudinal cavity mode as the FORT. The light emerging from the cavity as a Gaussian beam is coupled into a fiber beam splitter, which leads to two single photon avalanche photo-detectors (APDs). The APD pulses signalling photon detection events are time-stamped and recorded by a computer data acquisition card. The experimental timing is set with the help of a computer-controlled programmable multi-channel TTL pulse generator.

For more details on the lab setup, please see Ref. [1], Chapter 2, and references within.

1.2 Recent progress: A summary

Before joining the cavity lab in 2002, I worked for three years in what is now known as the atomic ensemble lab, which at the time was being built from the ground up by Dave Boozer, with the help of Christoph Nägerl, Jason McKeever, Ron Legere, Win Goh, Kaiwen Xu, and myself. We implemented a number of useful techniques, some of which ended up being adapted for the cavity lab or for the collective enhancement experiment in the ensemble lab. Here are a few examples: we phase locked two diode lasers separated in frequency by the Cesium ground state hyperfine splitting (~ 9.2 GHz) and used them to drive Raman transitions in cold atomic clouds. With this Raman setup, we detected Ramsey fringes, Rabi flopping, and Zeeman spectra as a way of determining the population distribution among ground state sublevels, and

hence of measuring the ambient magnetic fields *in situ*. We also loaded a running-wave optical trap from a MOT and saw significant atom-survival probabilities after a few seconds. In addition, we were able to load a MOT from the background gas in one vacuum chamber, then push the atoms up against gravity with a resonant beam into a different chamber at much lower pressure, where they were caught into a second MOT. This setup was intended for loading a long-lifetime optical trap, in which Raman sideband cooling would eventually be studied.

In the meantime, however, people in one of the two cavity QED labs in our group had been working hard trying to improve the lifetime of their intra-cavity FORT. The breakthrough [2] came when Jason McKeever and Joe Buck switched to a wavelength that provides nearly equal trapping potentials for the ground and excited state of the cavity QED transition, and that is not plagued by heating mechanisms associated with high cavity finesse. The first experiment they did using this long-lifetime, state-insensitive trap involved continuously probing the atom-cavity system near resonance, and inferring the number of atoms in the trap from the detected probe transmission [3]. It was around this time that Joe graduated, Dave joined the cavity QED experiment as a theorist, data analysis guru, and all-around big-picture guy, and I became Jason's apprentice in the cavity lab. We proceeded to implement the one-atom laser in the strong coupling regime [4]. This experiment consisted of driving the atom and observing the photon stream emerging from the cavity, which exhibited thresholdless emission and non-classical statistics. We were then joined by Russ Miller in the lab, and together used a pulsed pumping scheme for driving the atom, which enabled deterministic single-photon generation with near-unit inferred production efficiency [5]. For more information on these experiments, please refer to Jason's thesis [1].

To summarize: at this point, our lab had the capability of keeping atoms in the trap for $2 - 3$ s "in the dark," i.e., in the absence of near-resonant driving; also, we knew how to measure the number of atoms interacting with the cavity QED field. But no attempt had been made at controlling the magnetic sublevel of the atomic state, or at the related issue of controlling the polarization of photons emerging from

the cavity. When continuously driving the atom, the radial cooling beams would significantly decrease the trapping lifetime, and we did not know whether this was due to a residual magnetic field adversely affecting the Sisyphus cooling, or to axial heating. We had never obtained a convincing signature of the atomic motion within the trap, nor had we tried to cool the axial temperature, or to measure the atomic energy distribution. Finally, we had no way of telling "which well" the atom was loaded in, i.e., what the strength of the cavity QED interaction was at the atomic location.

We were joined at this point by Kevin Birnbaum, who left his own cavity lab to become a theorist and take over much of the numerical modeling for our experiment. In the lab, with Jason away writing his thesis, we started working on a scheme designed by Dave, which was promising to solve most, if not all, of the above-mentioned problems.

The scheme involved driving Raman transitions between the atomic ground states, using the intra-cavity FORT in conjunction with another beam off-resonantly coupled to the same cavity mode. The results obtained to date with the Raman approach are described in detail in Dave's thesis [6]. In brief, thanks to the Raman transitions, we are now able to control precisely the magnetic fields at the location of the atom within the cavity, including the inhomogeneous pseudo-field due to imperfections in the FORT polarization. With these stray bias fields properly nulled, the radial cooling beams no longer significantly reduce the trapping lifetime. We can also measure the population in each ground state magnetic sublevel; we have verified that we can optically pump the atomic population into a single such sublevel with good efficiency, meaning that we have a better handle than ever before on the atomic internal state. Furthermore, we have observed Rabi oscillations between the $F = 3$ and $F = 4$ ground hyperfine levels, which promise the ability to synthesize arbitrary superpositions of the two atomic ground states in the near future. Most importantly, we have some preliminary evidence of axial Raman sideband cooling, allowing for lifetimes comparable to those in the dark even in the presence of short pulses of resonant or near-resonant probing.

This latter capability enabled us to do the vacuum-Rabi experiment [7], which consisted of driving the cavity with a probe of varying detuning from the atomic transition, and recording the resulting transmission spectrum for each atom. This measurement allowed us to determine the atom-cavity coupling strength g on an atom-by-atom basis, which means that, for that particular experimental protocol, we have solved the "which-well" problem. The data indicate that we can select those atoms which are well coupled to the cavity QED field, and which populate only the bottom tenth of the trapping well. Chapter 2 elaborates on this topic.

Our next experiment was the photon blockade [8], which further investigated the Jaynes-Cummings ladder of atom-cavity eigenstates. While quantifying the vacuum-Rabi spectrum was only concerned with the lowest excitation manifold, the photon blockade measurement explored what happens when one tries to climb the ladder by probing the system resonantly on one of the vacuum-Rabi sidebands. Due to an-harmonicity of the level structure, population in the two-excitation manifold is suppressed, so that the coherent-state probe is converted by the atom-cavity system into a sub-Poissonian, anti-bunched photon stream. We used motion-induced modulation on the probe transmission to make another temperature estimate, the result of which was consistent with the previous one mentioned above. Chapter 3 describes these measurements in much more detail, while Chapter 4 dwells on estimating a few lab parameters relevant for both the vacuum-Rabi and the photon blockade experiments.

The near-future outlook for our lab is to focus on perfecting the various preliminary results involving Raman transitions. We have concrete plans to eliminate the technical noise which we suspect now constitutes the limitation on these techniques. We would then expect to be able to optimize and characterize fully the axial sideband cooling, and to synthesize arbitrary superpositions of the ground states. We should also work on improving the efficiency of our optical pumping, since a useful starting point for experiments is with all the atomic population being in a known, single magnetic sublevel. With the problems of cooling and state preparation solved, we would be in the enviable position of having control over both the internal and the motional state of our atom, in addition to the already-existing ability to measure its

interaction with the cavity mode.

From that point on, the sky is the limit. There have been numerous proposals to implement diverse quantum information science protocols in cavity QED. These include reversible conversion of a stationary qubit, as encoded in the atomic state, into a flying qubit, given by the polarization or number state of a photon [9]; atom-photon entanglement [9]; quantum non-demolition measurement of a single photon, as well as single and two-qubit gates for computation [10]; teleportation of an atomic state into a photon and vice-versa; and ultimately quantum networking, with high-finesse optical cavities at the nodes, and optical fibers as interconnects [11, 12].

Chapter 2

Vacuum-Rabi experiment

This chapter includes a couple of very basic theoretical models relevant to the vacuum-Rabi spectrum of a strongly coupled atom-cavity system, as well a discussion of the experiment we did for measuring this spectrum on an atom-by-atom basis.

2.1   Jaynes-Cummings Hamiltonian

A two-level stationary atom interacting with a single mode of the electromagnetic field is described by the Jaynes-Cummings Hamiltonian [13] (after setting $\hbar = 1$, and in the rotating wave approximation):

$$H = \omega_A \sigma_+ \sigma_- + \omega_C a^\dagger a + g(a^\dagger \sigma_- + a \sigma_+). \tag{2.1}$$

The atomic raising and lowering operators are

$$\sigma_+ = \frac{1}{2}(\sigma_x + i\sigma_y) = |e\rangle\langle g| \quad \text{and} \quad \sigma_- = \frac{1}{2}(\sigma_x - i\sigma_y) = |g\rangle\langle e|, \tag{2.2}$$

where $|g\rangle$ and $|e\rangle$ are the atomic states, separated by ω_A, and $\sigma_{x,y}$ are the Pauli spin matrices,

$$\sigma_x = |e\rangle\langle g| + |g\rangle\langle e| \quad \text{and} \quad \sigma_y = -i|e\rangle\langle g| + i|g\rangle\langle e|. \tag{2.3}$$

The field, thought of as a single mode of an ideal cavity, is taken to be at frequency ω_C, and its raising and lowering operators are $a^\dagger$ and a, with matrix elements between Fock states given by

$$\langle n-1|a|n\rangle = \sqrt{n} \quad \text{and} \quad \langle n+1|a^\dagger|n\rangle = \sqrt{n+1}\,. \tag{2.4}$$

The first term of the Hamiltonian in (2.1) represents the atomic internal energy, the second term describes the energy in the field excitation, and the third term governs the interaction between the atom and the cavity field, with strength given by the coupling constant g.

Let us choose a basis made up of tensor products of atomic and Fock states, $\{|g,0\rangle, |g,1\rangle, |e,0\rangle, |g,2\rangle, |e,1\rangle, \ldots\}$, which diagonalizes the uncoupled Hamiltonian, obtainable from (2.1) by setting $g = 0$. The coupled Hamiltonian with $g > 0$ is block-diagonal in this basis, being made up of 2×2 blocks (except for the 1×1 block corresponding to $\langle g,0|H|g,0\rangle$) along the diagonal of H, of the type:

$$H_n = \begin{pmatrix} \omega_C n & g\sqrt{n} \\ g\sqrt{n} & \omega_A + \omega_C(n-1) \end{pmatrix}, \tag{2.5}$$

and with zeros everywhere else. The H_n block corresponds to n total excitations shared by the atom and the field, i.e., to the states $\{|g,n\rangle, |e,n-1\rangle\}$, and can be easily diagonalized, yielding eigenvalues and corresponding eigenvectors

$$
\begin{aligned}
E_{n\pm} &= \frac{1}{2}\left(2n\omega_C - \delta_{CA} \pm \sqrt{4g^2 n + \delta_{CA}^2}\right) \\
|\pm\rangle_n &\propto \left(\delta_{CA} \pm \sqrt{4g^2 n + \delta_{CA}^2}\right)|g,n\rangle + 2g\sqrt{n}|e,n-1\rangle\,,
\end{aligned} \tag{2.6}
$$

which are all eigenenergies and respectively eigenstates of the original Hamiltonian H as well; here we defined the detuning between the field and the atom to be $\delta_{CA} = \omega_C - \omega_A$. For $n = 1$, depending on the sign of δ_{CA}, one of the $|\pm\rangle_1$ dressed states will have a larger coefficient for $|g,1\rangle$, making it the "cavity-like" state, in the sense that the excitation resides primarily in the field, whereas the other will have a larger
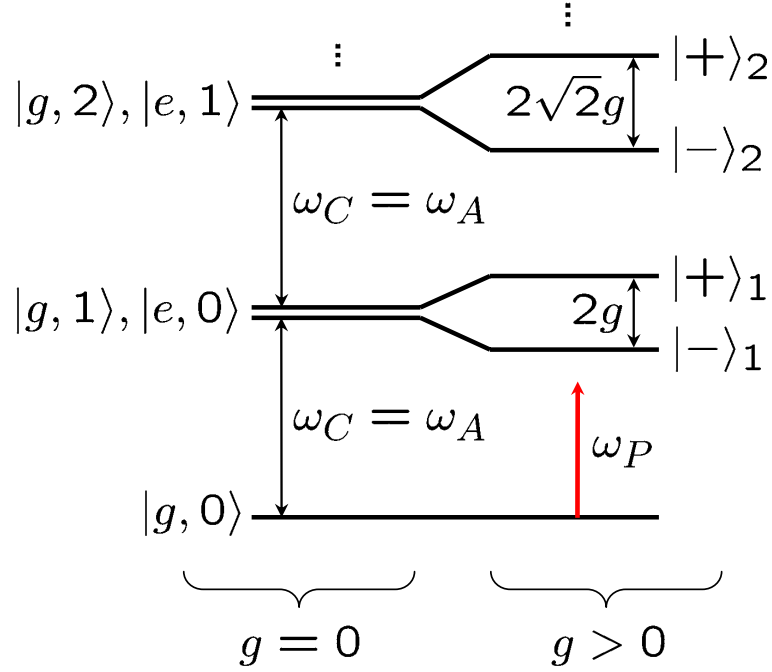
Figure 2.1: Jaynes-Cummings ladder of states.

$|e, 0\rangle$ component, making it the "atom-like" state, with most of the excitation stored in the atom's internal state.

If the cavity is tuned to the atomic resonance $\omega_C = \omega_A = \omega$, so that $\delta_{CA} = 0$, we get the Jaynes-Cummings ladder shown in Fig. 2.1, with energies and states given by

$$
\begin{aligned}
E_{n\pm} &= n\omega \pm g\sqrt{n} \\
|\pm\rangle_n &= \frac{1}{\sqrt{2}} \left(|g, n\rangle \pm |e, n-1\rangle \right) .
\end{aligned}
\tag{2.7}
$$

Note that this ladder is anharmonic, in the sense that neither $\{|+\rangle_n\}$ nor $\{|-\rangle_n\}$ are evenly spaced sets of states, since levels $E_{n\pm}$ are separated from the harmonic ladder level corresponding to n uncoupled excitations by $\pm g\sqrt{n}$. If we limit ourselves just to the first excitation, the separation between the dressed states is $2g$, known as the vacuum-Rabi splitting.

We can already get some intuition about how the system would behave if the cavity mode were to be driven with a probe field at frequency ω_P, even though this

drive is not yet included in the Hamiltonian. Namely, we would expect the cavity to show high transmission when driven near a resonance, i.e., near an eigenstate of H. Thus we expect that in the absence of coupling to an atom, the probe transmission will be high near the uncoupled states at $\omega_P = \omega_C$, whereas in the presence of the atom, we should get high transmission near the $|\pm\rangle_1$ levels at $\omega_P = \omega_C \pm g$.

2.2   Master equation and the weak driving limit

One step away from the idealized Jaynes-Cummings picture and closer to reality would be to include the effects of dissipation due to atomic spontaneous emission and to cavity decay, as well as a drive term in the Hamiltonian. This leads us to the master equation for ρ, the density operator of the system [14]:

$$
\begin{aligned}
\frac{d\rho}{dt} &= -i[H,\rho] + \kappa(2a\rho a^\dagger - a^\dagger a\rho - \rho a^\dagger a) + \gamma(2\sigma_-\rho\sigma_+ - \sigma_+\sigma_-\rho - \rho\sigma_+\sigma_-) \\
&= \mathcal{L}\rho,
\end{aligned}
\tag{2.8}
$$

where κ is the cavity field decay rate, γ is the amplitude spontaneous emission rate, $\mathcal{L}$ is the Liouvillian superoperator governing the density matrix dynamics, and the interaction-picture Hamiltonian is

$$
H = \delta_{AP}\sigma_+\sigma_- + \delta_{CP}a^\dagger a + g(a^\dagger\sigma_- + a\sigma_+) + (Ea^\dagger + E^*a).
\tag{2.9}
$$

Here the detunings are defined as $\delta_{AP} = \omega_A - \omega_P$ between the atomic resonance and the probe laser, and $\delta_{CP} = \omega_C - \omega_P$ between the cavity field and the probe. As before, the first two terms in (2.9) represent the energy stored within the free atom and field, and the third term represents their interaction. The last term describes the drive of the cavity mode, with E proportional to the amplitude of the coherent-state probe at optical frequency ω_P.

One can use the master equation to derive equations of motion for the relevant operators and their expectation values (ensemble averages). For instance, let the

lowering operators' expectation values be $\langle a \rangle = \alpha$ and $\langle \sigma_- \rangle = \beta$. Then it follows that

$$\dot{\alpha} = \text{Tr}[a\dot{\rho}], \text{ and } \dot{\beta} = \text{Tr}[\sigma_- \dot{\rho}]. \tag{2.10}$$

One can imagine plugging the expression for $\dot{\rho}$ from the master equation (2.8) into (2.10), and using the cyclic property of the trace

$$\text{Tr}[ABC] = \text{Tr}[BCA] = \text{Tr}[CAB], \tag{2.11}$$

together with the commutator and anticommutator relations

$$\begin{aligned}
[a, a^\dagger] &= 1 \\
[a, \sigma_\pm] &= 0 \\
\{\sigma_+, \sigma_-\} &= 1,
\end{aligned} \tag{2.12}$$

to simplify things a bit. However, the resulting expressions for $\dot{\alpha}$ and $\dot{\beta}$ will still be rather complicated, involving the expectation values of operators other than just a and σ_-. In general, the operator equations of motion will not form a closed system, and one will need to make approximations to obtain a solution.

One such approximation, when the steady-state solution can be found analytically, is the weak driving limit. The assumption in this limit is that there is at most one excitation in the system, thus we can truncate the state space to $\{|g, 0\rangle, |g, 1\rangle, |e, 0\rangle\}$. In this basis,

$$a^2 = \sigma_-^2 = a\sigma_- = 0 , \tag{2.13}$$

so that the equations of motion become simply:

$$\begin{aligned}
\dot{\alpha} &= -(\kappa + i\delta_{CP})\alpha - ig\beta - iE \\
\dot{\beta} &= -ig\alpha - (\gamma + i\delta_{AP})\beta .
\end{aligned} \tag{2.14}$$

The steady state solution can be found by setting $\dot{\alpha} = 0$ and $\dot{\beta} = 0$, and gives for the
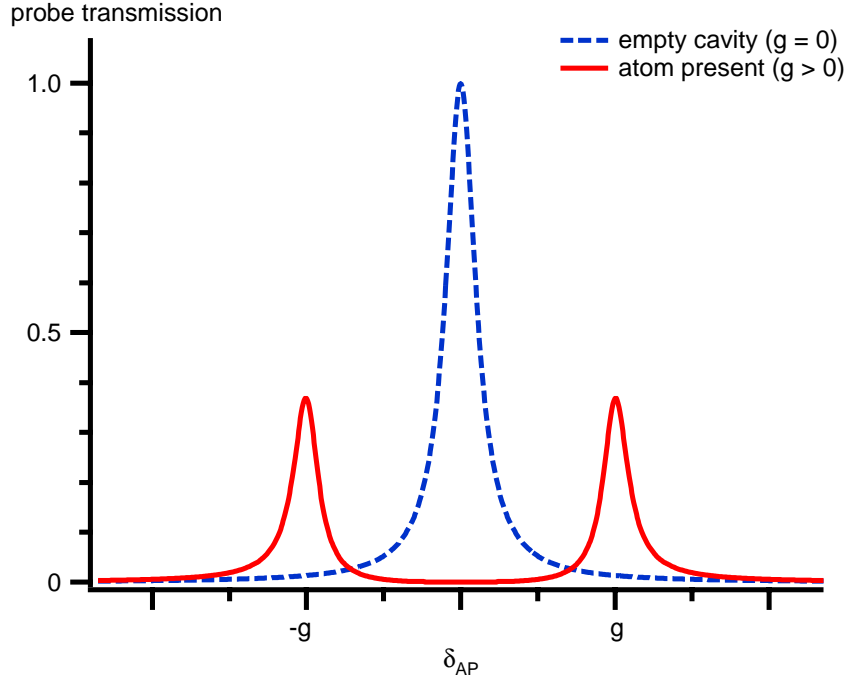
Figure 2.2: Vacuum-Rabi spectrum in the weak driving limit, plotted for $g = 2\pi \times 34$ MHz, $\kappa = 2\pi \times 4$ MHz, $\gamma = 2\pi \times 2.6$ MHz, and $\delta_{CA} = 0$.

cavity field amplitude:

$$\alpha_{ss} = \frac{-iE(\gamma + i\delta_{AP})}{g^2 + (\gamma + i\delta_{AP})(\kappa + i\delta_{CP})} \ . \tag{2.15}$$

The steady state intracavity photon number expectation value is $n_{ss} = \langle a^\dagger a \rangle_{ss}$, which in the weak driving limit is simply given by $|\alpha_{ss}|^2$. For fixed ω_C and ω_A, n_{ss} is proportional to the cavity-atom system's transmission spectrum as a function of the probe frequency, which is normalized to 1 for the uncoupled cavity driven on resonance:

$$T = n_{ss}(\kappa^2/|E|^2) = \frac{\kappa^2(\gamma^2 + \delta_{AP}^2)}{(g^2 - \delta_{AP}\delta_{CP} + \gamma\kappa)^2 + (\gamma\delta_{CP} + \kappa\delta_{AP})^2} \ . \tag{2.16}$$

As shown by the "atom present" curve in Fig. 2.2, when the cavity is tuned to the atomic resonance $\delta_{CA} = \delta_{CP} - \delta_{AP} = 0$, the probe spectrum is double-peaked and symmetric about $\delta_{AP} = 0$. The peak separation is $2g$, recovering the vacuum-Rabi
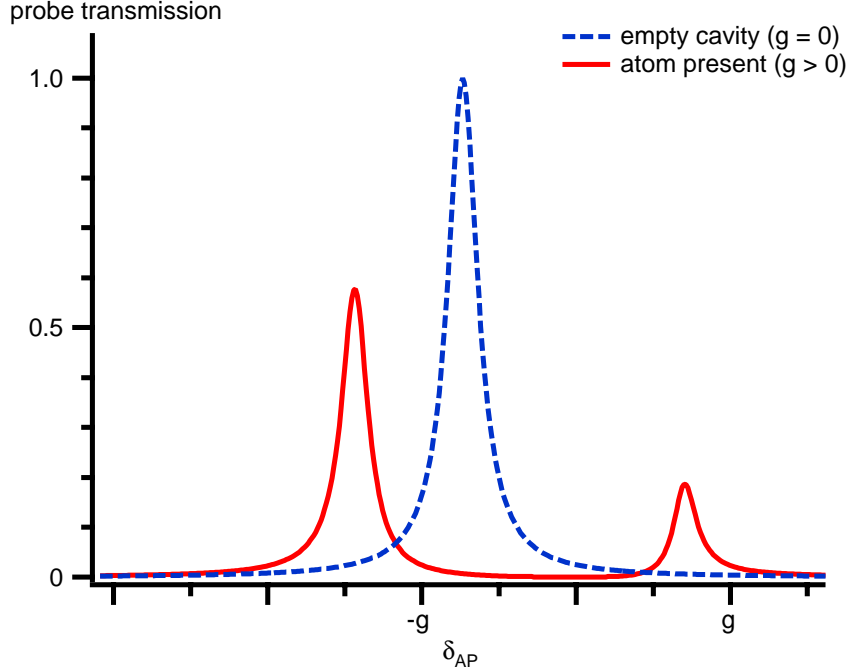
Figure 2.3: Vacuum-Rabi spectrum in the weak driving limit, plotted for $g = 2\pi \times 34$ MHz, $\kappa = 2\pi \times 4$ MHz, $\gamma = 2\pi \times 2.6$ MHz, and $\delta_{CA} = 2\pi \times 25$ MHz.

splitting we saw in the Jaynes-Cummings Hamiltonian picture. The two peaks are well resolved in the regime where $g \gg (\kappa, \gamma)$, known as strong coupling, when their half widths are approximated by $(\gamma + \kappa)/2$. For $g = 0$, the transmission spectrum from (2.16) reduces to the familiar Lorentzian centered at $\delta_{CA} = 0$, with half width at half maximum κ, shown in Fig. 2.2 as the "empty" (i.e., uncoupled) cavity curve.

If the cavity is tuned away from the atomic resonance, as shown in Fig. 2.3, the vacuum-Rabi spectrum is no longer symmetric about $\delta_{AP} = 0$, nor about $\delta_{AP} = \delta_{AC}$, and it recovers the atom-like / cavity-like structure of the eigenstates in Eqn. 2.6. The vacuum-Rabi sidebands are now separated by $(4g^2 + \delta_{CA}^2)^{1/2}$, and the empty cavity peak is also shifted by δ_{CA} from the atomic resonance, as expected.
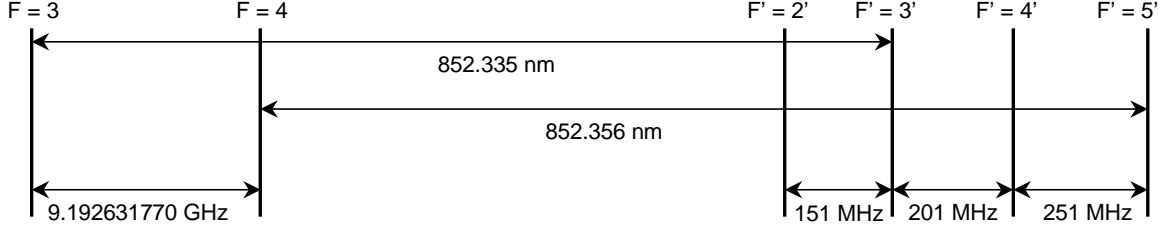
Figure 2.4: Cesium level structure for the D2 line.

2.3 Lab numbers: What to expect

How do these simple models relate to the situation we have in the lab? There will be several deviations from the two-level atom, single-mode models of Secs. 2.1 and 2.2, many of which are taken into consideration in a rigorous fashion in the simulations presented in Kevin Birnbaum's thesis [9] and in Sec. 2.5. The present section only attempts to list the necessary extensions to the simplest model, and hopefully to give us some intuitive understanding of what to expect from the lab data.

Take first the two-state atom assumption. The atom we work with is Cesium, which has many more states than just two. If we were to tune our probe and cavity near the $F = 4 \rightarrow F' = 5'$ transition within the D2 line at $\lambda_{D2} = 852$ nm (see Fig. 2.4), we could imagine ignoring any of the levels not directly involved in this transition. Still, if we count in all the Zeeman sublevels, that leaves nine ground states and eleven excited states which should be included in the Hamiltonian and master equation, if a quantitative prediction of the vacuum-Rabi spectrum is to be made.

As for the strong coupling regime, we should start by estimating the rate of coherent interaction set by g, in order to compare it to the known dissipation rates $\kappa \simeq 2\pi \times 4$ MHz and $\gamma = 2\pi \times 2.6$ MHz. Since g is the strength of the dipole interaction between the atom and the quantized field, one can show that:

$$g(4, m_F \rightarrow 5, m_F + q) = 2\pi \times \langle F = 4, m_F; 1, q | F = 5, m_F + q \rangle \, \mu_0 \sqrt{\frac{2c}{\epsilon_0 h V \lambda}} \, , \quad (2.17)$$

for a particular pair of levels within the $F = 4$ and the $F' = 5'$ manifolds. Here
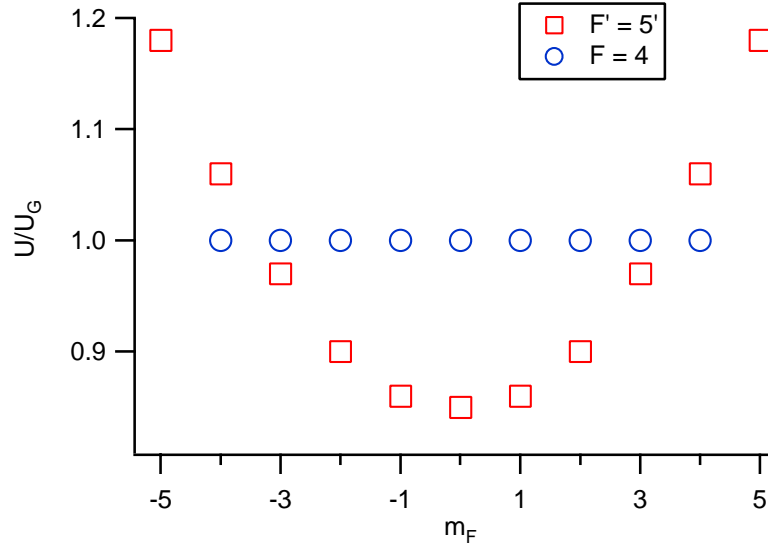
Figure 2.5: Ground and excited state trap depth, relative to the ground state's, as a function of the m_F quantum number.

$q = 0, \pm 1$ for field polarization $\pi, \sigma^{\pm}$ respectively, $V = \pi w_0^2 l_{\text{eff}}$ is the mode volume associated with mode waist w_0 and effective cavity length l_{eff} (see Secs. 4.1 and 4.2), λ is the electromagnetic field's wavelength, and $\mu_0 = 3.167 \, ea_0$ is the electric dipole matrix element for the D2 transition, with e the electron charge and a_0 the Bohr radius. The largest Clebsch-Gordan coefficient, hence the biggest g, occurs for circularly polarized light driving a closed transition, with $\langle 4, 4; 1, 1 | 5, 5 \rangle = 1$ and $g(4, 4 \rightarrow 5', 5') = 2\pi \times 33.8$ MHz. However, for technical reasons it is convenient to use a linearly polarized probe in the lab, with the highest matrix element being $\langle 4, 0; 1, 0 | 5, 0 \rangle = \sqrt{5}/3$, and $g(4, 0 \rightarrow 5', 0') = 2\pi \times 25.2$ MHz. Either of these values for g satisfies the $g \gg (\kappa, \gamma)$ condition, so our system is well within the strong coupling regime. Therefore, we expect the vacuum-Rabi spectrum to exhibit two well-resolved peaks.

Now let us consider the single-mode assumption. Our cavity is a Fabry-Perot resonator of very high finesse, for which the linewidth κ at λ_{D2} is much smaller than either the transverse or the longitudinal mode spacings (see Secs. 4.1, 4.2 and 4.3). This would seem to indicate that the single-mode picture is correct. However, the cavity supports two orthogonally polarized, nondegenerate modes (see Sec. 4.6),
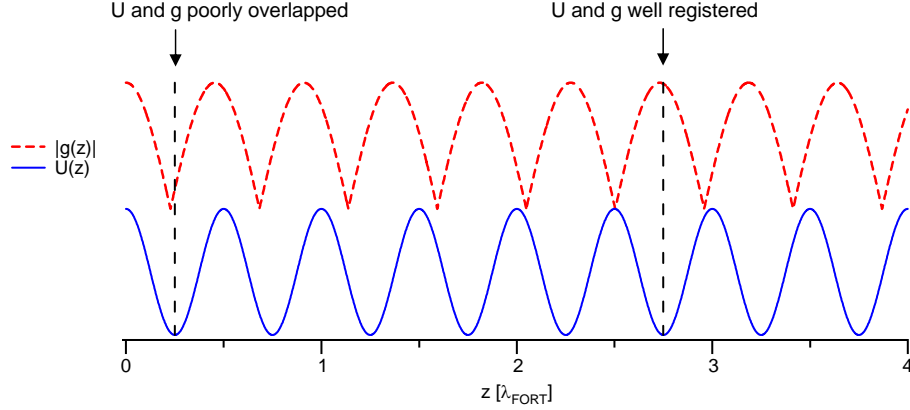
Figure 2.6: Axial registration: due to different mode numbers, the FORT and the cavity QED pancake structures in the cavity do not normally overlap.

both of which should be accounted for in the model. A master equation calculation [9] will show that even in the absence of a birefringent splitting or of any AC Stark shifts due to the trapping potential, the vacuum-Rabi spectrum of a multi-level atom coupled to two independent cavity modes will be qualitatively quite different from that obtained with a single-mode model. The most significant difference is that the spectrum, though still symmetric about $\delta_{AP} = 0$, now has not two, but four peaks. The atomic population is redistributed by the probe among the various sublevels, each of which couples to each of the two cavity modes with a potentially different matrix element, which leads to the more complex spectrum.

An added complication is introduced by the dipole trap. Our FORT wavelength $\lambda_{FORT} = 936$ nm was carefully chosen so that the ground $F = 4, 6S_{1/2}$ and excited $F' = 5', 6P_{3/2}$ states are nearly equally shifted by the dipole potential. However, the emphasis here is on "nearly." Though all the m_F sublevels of the ground state experience equal AC Stark shifts in a linearly polarized trap, the excited states do have a residual quadratic dependence on the magnetic quantum number. This dependence was calculated by Jason McKeever et al. in Ref. [2], and is shown in Fig. 2.5. As a consequence, each sublevel will have a different effective atom-cavity detuning δ_{AC}, which in conjunction with the probe's optical pumping of the atomic population among the various m_F-levels should lead to an asymmetric vacuum-Rabi spectrum,
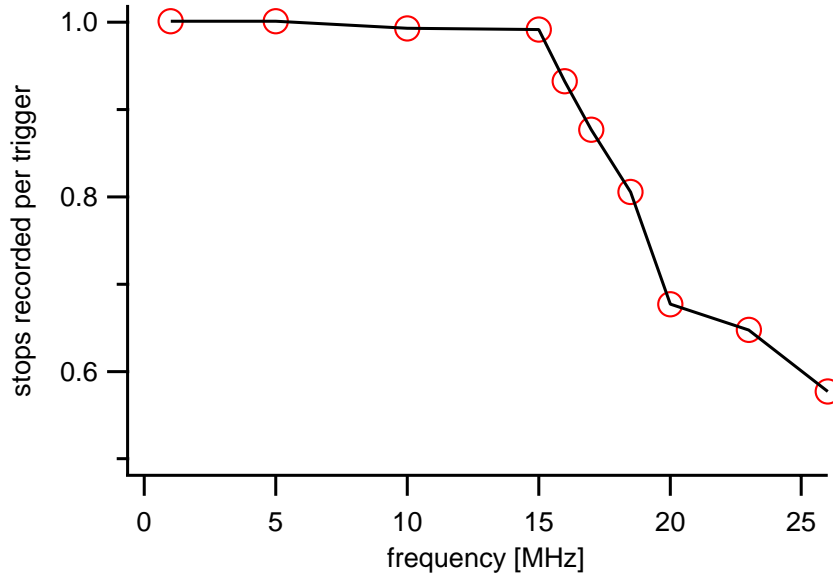
Figure 2.7: Measured probability of counting a "stop", given a trigger, for the P7888 data acquisition card, as a function of the input RF frequency.

as suggested by Fig. 2.3.

One also needs to consider the effects of the imperfect registration between the FORT and the probe sinusoidal patterns inside the cavity. The mode order at λ_{FORT} is even (see Sec. 4.1), so that the spatial dependence of the FORT depth on the axial coordinate z is $\sin^2(2\pi z/\lambda_{\mathrm{FORT}})$, where we took the cavity center to be located at $z = 0$. At λ_{D2} however, the mode order is odd, so that the strength of the CQED interaction g goes like $\cos(2\pi z/\lambda_{D2})$, as shown in Fig. 2.6. Thus if the FORT and the cavity QED start out overlapped at some point on the cavity axis, they will come completely out of registration after only a few wavelengths. Different FORT wells that the atom might get loaded into will have potentially different couplings to the cavity field, hence different transmission spectra as set by $|g|$ in Eqn. (2.16). We expect this inhomogeneity to lead to a broadening of the vacuum-Rabi peaks, to a shift of their peak centers towards the origin, i.e., towards smaller $|g|$, and to increased on-resonance transmission reminiscent of the empty-cavity curve in Fig. 2.3. But even an ideally coupled atom, i.e., one with maximal g at the bottom of its well, will move around within this well and experience a distribution of g values
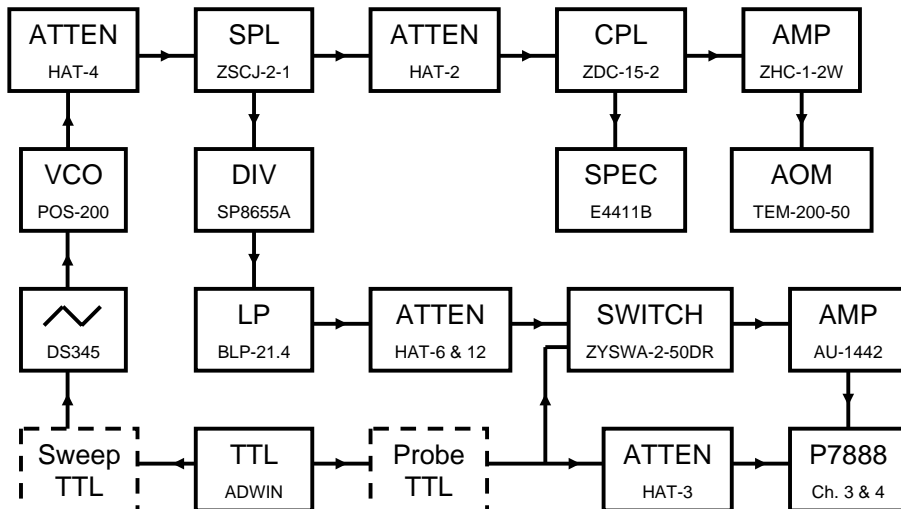
Figure 2.8: Electronics setup for digitizing the probe frequency *in situ*.

depending on the temperature (wider for the hotter atoms), which should further broaden the vacuum-Rabi sidebands.

2.4 Experimental details

The main challenge to measuring the vacuum-Rabi spectrum of one-and-the-same atom is being able to hold on to the said atom for long enough to obtain quantitative information about it, in spite of heating induced by the probe. Two major advances in our lab have made this possible. The first was extending the trapping lifetime "in the dark," i.e., in the absence of any near-resonant light, to $2 - 3$ s, which was enabled by the state-insensitive dipole trap, and which is discussed in detail by Jason McKeever in his thesis [1]. The second was cooling the atomic motion, which is done with blue-Sisyphus [15] near-resonant light for the radial direction, and via a Raman sideband mechanism involving the FORT and another far detuned beam, for the axial direction. David Boozer talks about this axial cooling scheme in detail in his thesis [6], so I will not elaborate on this topic here. The vacuum-Rabi experiment was an opportunity to demonstrate the capabilities of this new axial cooling method, before even attempting to fully characterize it.
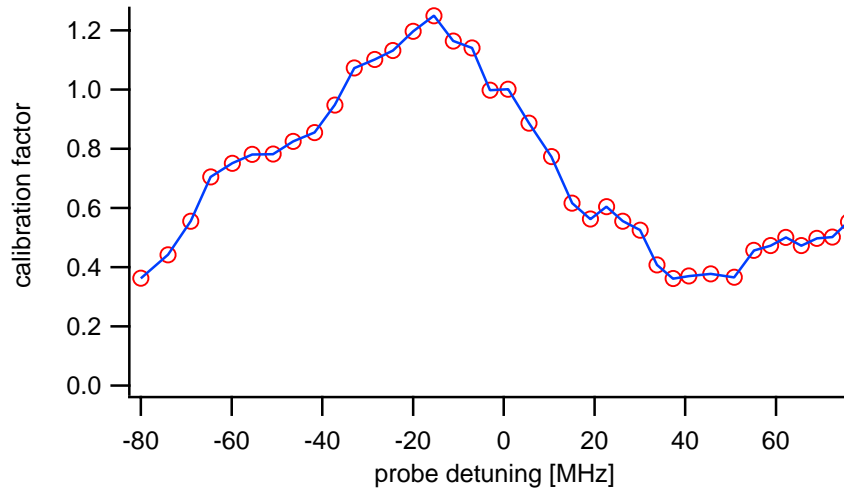
Figure 2.9: Normalization curve for detected probe power, as a function of detuning from atomic resonance.

One remaining technical challenge involved scanning the probe frequency in a controllable way. In order to cover a ~ 140 MHz range around the atomic resonance, we needed to scan the RF supply to one of the double-passed AOMs that the probe goes through, in a range roughly from 135 to 205 MHz. Since we wanted the option of doing that scan several times a second, we decided for a POS-200 voltage-controlled oscillator (VCO) as the RF source, because VCOs can cover a large frequency range of 100 MHz or more, and they can do it fast, albeit not quite linearly with the input voltage. We used the P7888 pulse counting card that does our data acquisition to measure the VCO frequency *in situ*. As shown in Fig. 2.7, when connected to our 2.8 GHz Pentium IV computer, the card can count the pulses in an RF signal of up to 15 MHz with less than 1% error, but it drops a significant fraction of the triggers for larger input frequencies[1]. To bridge the gap between the VCO frequency and the computer card, we employed a $\div 32$ frequency divider chip, as shown schematically in Fig. 2.8. Note that we only acquire the divided frequency during those intervals when the probe is on (see Fig. 2.10), which gives the P7888 card enough time in between to write the pulses to the hard drive. Both the physics cavity and the probe are independently locked to Cesium, which means that once the probe AOM frequency

---

[1]Measured on 9/8/04.

Cooling:
radial: 4→4'
axial: Raman
2.9 ms

Probing:
probe: 4→5'
repump: 3→4'
0.1 ms

Probe
Detuning
[MHz]

+70

-70

time [s]

0

1.2
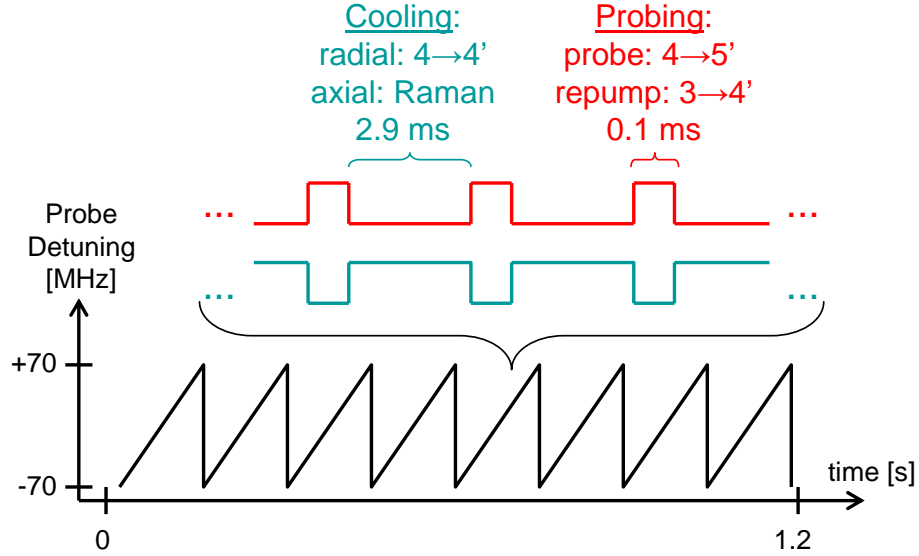
Figure 2.10: Timing diagram for the vacuum-Rabi experiment.

is known, so are the cavity-probe and atom-probe detuning.

Another issue is related to the AOM resonance curve, which makes the input power to the cavity change as the probe frequency is being scanned. In addition, as the frequency changes, so does the probe beam alignment after the AOM, hence its coupling efficiency to the cavity. Both these effects can be however easily taken into account by acquiring a calibration curve, analogous to that from Fig. 4.3, and using it to normalize all probe spectra. At each point, for a particular probe detuning from the D2 line, the cavity is tuned to be in resonance with the light, and its transmission is recorded with the avalanche photodetectors. The calibration curve[2] we took for the vacuum-Rabi experiment is shown in Fig. 2.9.

For acquiring the vacuum-Rabi spectrum[3] of Sec. 2.5, the probe, the FORT and the locking laser all have the same linear polarization, perpendicular to that of the Raman beam, all set by the glan-laser polarizer angle at the cavity input. The probe polarization is close to one of the birefringent axes, namely to the one with the higher resonance frequency (the "blue" mode). The $\lambda/2$ waveplate at the cavity output is set so as to maximize the empty cavity (i.e., no atom present) probe transmission on

[2]Measured on 9/29/04.
[3]Measured on 9/28/04.
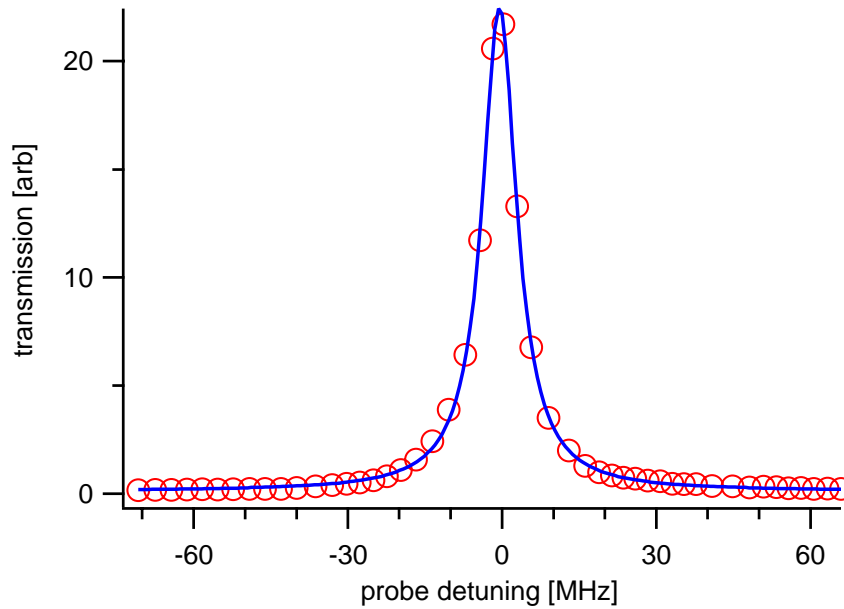
Figure 2.11: Empty cavity data acquired with the probe scanning protocol of Sec. 2.5. Fit yields $\kappa = 2\pi \times 4.1$ MHz.

resonance. After each trap loading attempt, we scan the probe frequency, while at the same time shuttering it on and off, in order to intersperse the cooling intervals. The timing diagram for the experiment is shown schematically in Fig. 2.10, and will be described in more detail in the next section. During each $100~\mu$s probing interval, both the probe and its repumper are turned on. We chose the $F = 3 \rightarrow F' = 4'$ transition frequency for the repumper, because it has no dark states, hence it is an effective way to maximize the time the atom spends in the cavity-coupled, hence useful $F = 4$ state. Shuttering for all beams is done with RF switches at the AOM inputs. The FORT beam is on all the time.

One might notice that some of the values for the experimental parameters quoted in Sec. 2.5 (e.g., the various efficiencies, mode waists, and κ) are slightly different from those given in Chapter 4. In all cases the values cited in the paper [7] and repeated in Sec. 2.5 below were those we thought to be correct at the time. Most of the discrepancies are insignificant and would not modify the theoretically predicted spectra in any noticeable way. The only difference worth mentioning is that of $\kappa =$

$2\pi \times 3.3$ to 3.6 MHz in Chapter 4, as opposed to 4.1 MHz in Sec. 2.5. The latter value was determined by fitting a Lorentzian to empty cavity data obtained in the same manner as the vacuum-Rabi spectrum data, as shown in Fig. 2.11. More specifically, the probe frequency was scanned linearly over the ~ 137 MHz range eight times in 1.2 s, and the resulting transmission spectra were averaged, then normalized by the curve shown in Fig. 2.9. The fit gives $\kappa = 2\pi \times (4.08 \pm 0.03)$ MHz for the Lorentzian half-width.

2.5 Observation of the vacuum-Rabi spectrum for one trapped atom

This section is reproduced almost verbatim from Ref. [7].

A cornerstone of optical physics is the interaction of a single atom with the electromagnetic field of a high quality resonator. Of particular importance is the regime of strong coupling, for which the frequency scale g associated with reversible evolution for the atom-cavity system exceeds the rates (γ, κ) for irreversible decay of atom and cavity field, respectively [16]. In the domain of strong coupling, a photon emitted by the atom into the cavity mode is likely to be repeatedly absorbed and re-emitted at the single-quantum Rabi frequency $2g$ before being irreversibly lost into the environment. This oscillatory exchange of excitation between atom and cavity field results from a normal mode splitting in the eigenvalue spectrum of the atom-cavity system [13, 17, 18], and has been dubbed the vacuum-Rabi splitting [17].

Strong coupling in cavity QED as evidenced by the vacuum-Rabi splitting provides enabling capabilities for quantum information science, including for the implementation of scalable quantum computation [19, 10], for the realization of distributed quantum networks [11, 12], and more generally, for the study of open quantum systems [20]. Against this backdrop, experiments in cavity QED have made great strides over the past two decades to achieve strong coupling [21]. The vacuum-Rabi splitting for single intracavity atoms has been observed with atomic beams in both the optical

[22, 23, 24] and microwave regimes [25]. The combination of laser cooled atoms and large coherent coupling has enabled the vacuum-Rabi spectrum to be obtained from transit signals produced by single atoms [26]. A significant advance has been the trapping of individual atoms in a regime of strong coupling [27, 2], with the vacuum-Rabi splitting first evidenced for single trapped atoms in Ref. [27] and the entire transmission spectra recorded in Ref. [28].

Without exception these prior single atom experiments related to the vacuum-Rabi splitting in cavity QED [22, 25, 23, 24, 26, 27, 2, 28] have required averaging over trials with many atoms to obtain quantitative spectral information, even if individual trials involved only single atoms (e.g., 10^5 atoms were required to obtain a spectrum in Ref. [25] and $> 10^3$ atoms were needed in Ref. [28]). By contrast, the implementation of complex algorithms in quantum information science requires the capability for repeated manipulation and measurement of an individual quantum system, as has been spectacularly demonstrated with trapped ions [29, 30] and recently with Cooper pair boxes [31, 32].

With this goal in mind, we describe here measurements of the spectral response of single atoms that are trapped and strongly coupled to the field of a high finesse optical resonator. By alternating intervals of probe measurement and of atomic cooling, we record a complete probe spectrum for one and the same atom. The vacuum-Rabi splitting is thereby measured in a quantitative fashion for each atom by way of a protocol that represents a first step towards more complex tasks in quantum information science. An essential component of our protocol is a new Raman scheme for cooling atomic motion along the cavity axis, that leads to inferred atomic localization $\Delta z_{\text{axial}} \simeq 33$ nm, $\Delta \rho_{\text{transverse}} \simeq 5.5$ μm.

A simple schematic of our experiment is given in Fig. 2.12 [1], showing a single atom trapped inside our optical cavity in the regime of strong coupling by way of an intracavity far-off-resonance trap (FORT) driven by the field $\mathcal{E}_{\text{FORT}}$. The transmission spectrum $T_1(\omega_p)$ for the atom-cavity system is obtained by varying the frequency ω_p of the probe beam $\mathcal{E}_p$ and recording the output with single-photon detectors. Cooling of the radial atomic motion is accomplished with the transverse fields Ω_4,
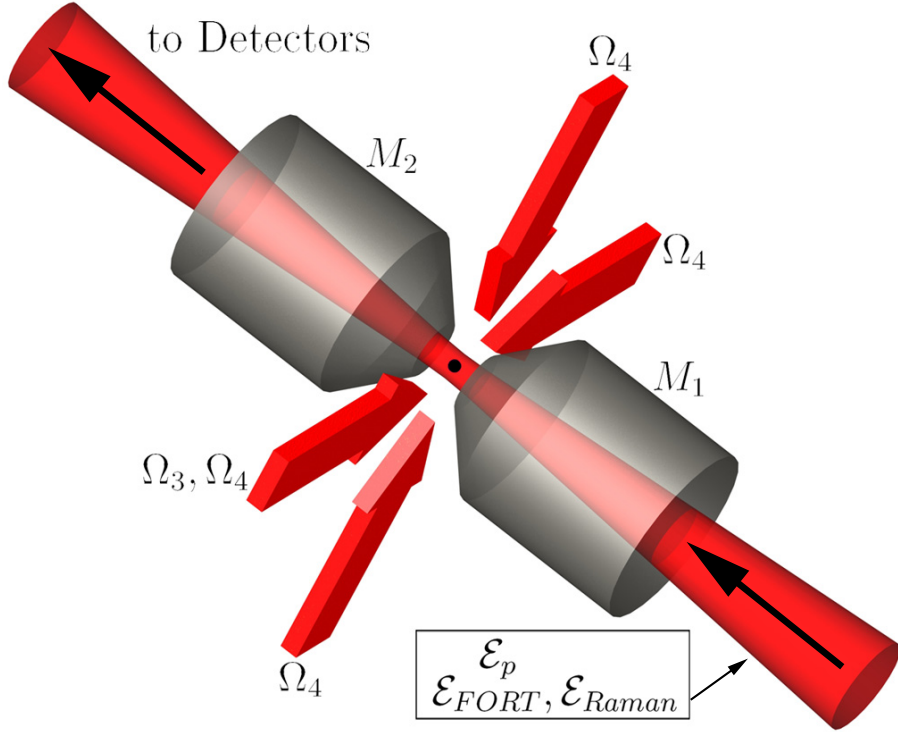
Figure 2.12: Schematic of the vacuum-Rabi experimental setup.

while axial cooling results from Raman transitions driven by the fields $\mathcal{E}_{\text{FORT}}$, $\mathcal{E}_{\text{Raman}}$. An additional transverse field Ω_3 acts as a repumper during probe intervals.

After release from a magneto-optical trap (MOT) located several mm above the Fabry-Perot cavity formed by mirrors (M_1, M_2), single Cesium atoms are cooled and loaded into the intracavity FORT and are thereby strongly coupled to a single mode of the cavity. Our experiment employs the $6S_{1/2}, F = 4 \rightarrow 6P_{3/2}, F' = 5'$ transition of the $D2$ line in Cesium at $\lambda_A = 852.4$ nm, for which the maximum single-photon Rabi frequency is $2g_0/2\pi = 68$ MHz for $(F = 4, m_F = \pm 4) \rightarrow (F' = 5', m'_F = \pm 5)$. The transverse decay rate for the $6P_{3/2}$ atomic states is $\gamma/2\pi = 2.6$ MHz, while the cavity field decays at rate $\kappa/2\pi = 4.1$ MHz. Hence our system is in the strong coupling regime of cavity QED $g_0 \gg (\gamma, \kappa)$ [16].

The intracavity FORT is driven by a linearly polarized input field $\mathcal{E}_{\text{FORT}}$ at $\lambda_F = 935.6$ nm, resulting in nearly equal AC-Stark shifts for all Zeeman states in the $6S_{1/2}, F = 3, 4$ manifold [33]. At an antinode of the field, the peak value of the

trapping potential for these states is $U_0/h = -39$ MHz for all measurements presented in this section. Zeeman states of the $6P_{3/2}, F' = 5'$ manifold likewise experience a trapping potential, albeit with a weak dependence on m'_F [2]. Birefringence in the mirrors leads to two nondegenerate cavity modes with orthogonal polarizations $\hat{l}_\pm$ and mode splitting $\Delta\nu_{C_1} = 4.4 \pm 0.2$ MHz at 852 nm. The fields $\mathcal{E}_{\text{FORT}}$ and $\mathcal{E}_{\text{Raman}}$ are linearly polarized and aligned close to the two orthogonal polarizations $\hat{l}_+$ and $\hat{l}_-$ of the higher, respectively the lower frequency mode. The cavity length is independently stabilized to length $l_0 = 42.2$ μm such that a TEM_{00} mode at λ_{C_1} is resonant with the free-space atomic transition at λ_A and another TEM_{00} mode at λ_{C_2} is resonant at λ_F. At the cavity center $z = 0$, the mode waists are $w_{C_{1,2}} = \{23.4, 24.5\}$ μm at $\lambda_{C_{1,2}} = \{852.4, 935.6\}$ nm.

As illustrated in Fig. 2.12, we record the transmission spectrum $T_1(\omega_p)$ for a weak external probe $\mathcal{E}_p$ of variable frequency ω_p incident upon the cavity containing one strongly coupled atom. $T_1(\omega_p)$ is proportional to the ratio of photon flux transmitted by M_2 to the flux $|\mathcal{E}_p|^2$ incident upon M_1, with normalization $T_0(\omega_p = \omega_{C_1}) \equiv 1$ for the empty cavity. Our protocol consists of an alternating sequence of probe and cooling intervals. The probe beam is linearly polarized and is matched to the TEM_{00} mode around λ_{C_1}. Relative to $\hat{l}_\pm$, the linear polarization vector $\hat{l}_p$ for the probe field $\mathcal{E}_p$ is aligned along a direction $\hat{l}_p = \cos\theta\hat{l}_+ + \sin\theta\hat{l}_-$, where $\theta = 13°$ for Fig. 2.13; however, the theoretical model we will discuss below maintains that the spectrum is relatively insensitive to θ for $\theta \lesssim 15°$. The probe field $\mathcal{E}_p$ illuminates the cavity for $\Delta t_{\text{probe}} = 100$ μs, and the transmitted light is detected by photon counting. The efficiency for photon escape from the cavity is $\alpha_{e2} = 0.6 \pm 0.1$. The propagation efficiency from M_2 to detectors (D_1, D_2) is $\alpha_P = 0.41 \pm .03$, with then each detector receiving half of the photons. The avalanche photodiodes (D_1, D_2) have quantum efficiencies $\alpha_P = 0.49 \pm 0.05$. During each probing interval a repumping beam Ω_3, transverse to the cavity axis and resonant with $6S_{1/2}, F = 3 \rightarrow 6P_{3/2}, F' = 4'$, also illuminates the atom. In successive probe intervals, the frequency ω_p is linearly swept from below to above the common atom-cavity resonance at $\omega_A \simeq \omega_{C_1}$. The frequency sweep for the probe is repeated eight times in $\Delta t_{\text{tot}} = 1.2$ s, and then a new loading cycle is
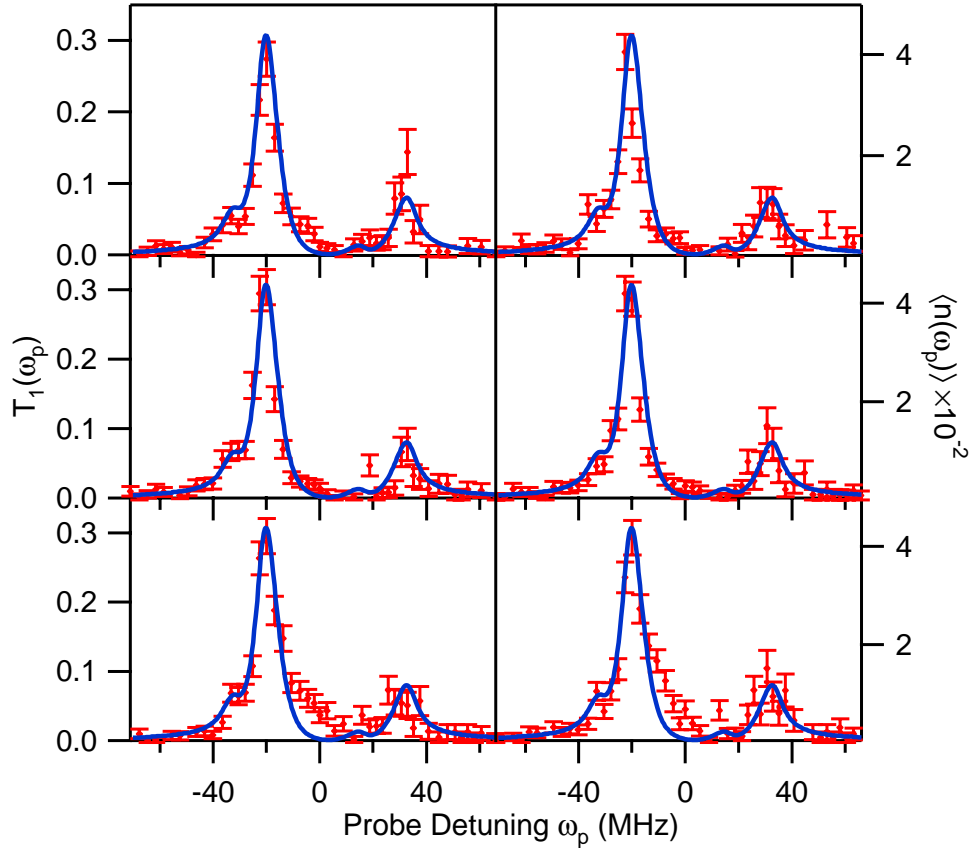
Figure 2.13: Transmission spectrum $T_1(\omega_p)$ for six randomly drawn atoms, and steady-state solution to the master equation, for comparison.

initiated.

Following each probe interval, we apply light to cool both the radial and axial motion for $\Delta t_{\text{cool}} = 2.9$ ms. Radial cooling is achieved by the Ω_4 beams consisting of pairs of counter-propagating fields in a $\sigma_\pm$ configuration perpendicular to the cavity axis, as shown in Fig. 2.12. The Ω_4 beams are detuned $\Delta_4 \simeq 10$ MHz to the *blue* of the $4 \rightarrow 4'$ transition to provide blue Sisyphus cooling [15] for motion transverse to the cavity axis.

To cool the axial motion for single trapped atoms, we have developed a new scheme that employs $\mathcal{E}_{\text{FORT}}$ and an auxiliary field $\mathcal{E}_{\text{Raman}}$ that is frequency offset by $\Delta_{\text{Raman}} = \Delta_{HF} + \delta$ and phase locked to $\mathcal{E}_{\text{FORT}}$. Here, $\Delta_{HF} = 9.192632$ GHz is the hyperfine splitting between $6S_{1/2}, F = 3, 4$. The fields $\mathcal{E}_{\text{FORT}}$, $\mathcal{E}_{\text{Raman}}$ drive Raman

transitions between the $F = 3, 4$ levels with effective Rabi frequency $\Omega_E \sim 200$ kHz. By tuning δ near the $\Delta n = -2$ motional sideband (i.e., $-2\nu_0 \sim \delta = -1.0$ MHz, where ν_0 is the axial vibrational frequency at an antinode of the FORT), we implement sideband cooling via the $F = 3 \to 4$ transition, with repumping provided by the Ω_4 beams. The Raman process also acts as a repumper for population pumped to the $F = 3$ level by the Ω_4 beams. Each cooling interval is initiated by turning on the fields Ω_4, $\mathcal{E}_{\text{Raman}}$ during Δt_{cool} and is terminated by gating these fields off before the next probe interval Δt_{probe}.

Fig. 2.13 displays normalized transmission spectra T_1 and corresponding intra-cavity photon numbers $\langle n(\omega_p) \rangle$ for six randomly drawn individual atoms, acquired via our protocol of alternating probe and cooling intervals. In each case, $T_1(\omega_p)$ is obtained for one-and-the-same atom, with the two peaks of the vacuum-Rabi spectrum clearly evident. The error bars reflect the statistical uncertainties in the number of photocounts. Also shown is the predicted transmission spectrum obtained from the steady-state solution to the master equation for one atom strongly coupled to the cavity, as discussed below. The quantitative correspondence between theory and experiment is evidently quite reasonable for each atom. Note that m_F-dependent Stark shifts for $F' = 5'$ in conjunction with optical pumping caused by $\mathcal{E}_p$ lead to the asymmetry of the peaks in Fig. 2.13 via an effective population-dependent shift of the atomic resonance frequency. The AC-Stark shifts of the $(F' = 5', m'_F)$ states are given by $\{m'_F, U_{m'_F}\} = \{\pm 5, 1.18U\}, \{\pm 4, 1.06U\}, \{\pm 3, 0.97U\}, \{\pm 2, 0.90U\}, \{\pm 1, 0.86U\}$, and $\{0, 0.85U\}$.

To obtain the data in Fig. 2.13, $N_{\text{load}} = 61$ atoms were loaded into the FORT in 500 attempts, with the probability that a given successful attempt involved 2 or more atoms estimated to be $P_{\text{load}}(N \geq 2) \lesssim 0.06$. Of the N_{load} atoms, $N_{\text{survive}} = 28$ atoms remained trapped for the entire duration Δt_{tot}. The six spectra shown in Fig. 2.13 were selected by a random drawing from this set of N_{survive} atoms. Our sole selection criterion for presence of an atom makes no consideration of the spectral structure of $T_1(\omega_p)$ except that there should be large absorption on line center, $T_1(\omega_p = \omega_{C_1}) \leq T_{\text{thresh}} \approx 0.2$. Transmission spectra $T_1(\omega_p), \bar{T}_1(\omega_p)$ are insensitive over a range of
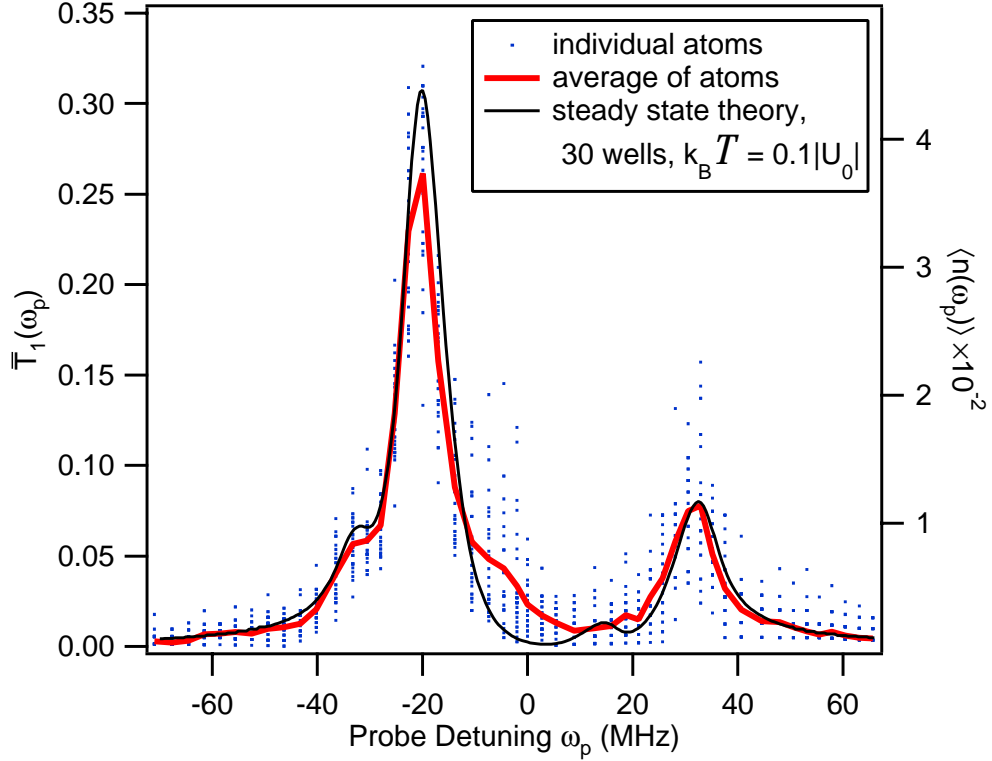
Figure 2.14: Individual transmission spectra $T_1(\omega_p)$ (dots), their average $\bar{T}_1(\omega_p)$ (thick trace), and the steady-state solution to the master equation (thin trace).

selection criteria $0.02 \leq T_{\text{thresh}} \leq 0.73$. Note that an atom trapped in the FORT in the absence of the cooling and probing light has lifetime $\tau_0 \simeq 3$ s, which leads to a survival probability $p(\Delta t_{\text{tot}}) \simeq 0.7$.

In Fig. 2.14 we collect the results for $T_1(\omega_p)$ for all $N_{\text{survive}} = 28$ atoms, and display the average transmission spectrum $\bar{T}_1(\omega_p)$, as well as a scatter plot from the individual spectra. Also shown for comparison is the steady-state solution to the master equation, already displayed in Fig. 2.13. The only free parameters in the theory are the temperature and the range of FORT antinodes; the vertical scale is absolute. This comparison demonstrates that the vacuum-Rabi spectrum observed for any particular atom represents with reasonable fidelity the spectrum that would be obtained from averaging over many atoms, albeit with fluctuations due to Poisson counting and optical pumping effects over the finite duration of the probe. The total acquisition time associated with the probe beam for the spectrum of any one atom is

only 40 ms.

We have also acquired transmission spectra $T_1(\omega_p)$ for operating conditions other than those in Figs. 2.13 and 2.14, including intensities $|\mathcal{E}_p|^2$ varied by factors of 2, $\frac{1}{2}$, and $\frac{1}{4}$, and atom-cavity detunings $\Delta_{AC} = \omega_A - \omega_{C_1} = \pm 13$ MHz. We will describe these results elsewhere.

The full curves in Figs. 2.13, 2.14 are obtained from the steady state solution of the master equation including all transitions $(F = 4, m_F) \leftrightarrow (F' = 5', m'_F)$ with their respective coupling coefficients $g_0^{(m_F, m'_F)}$, as well as the two nearly degenerate modes of our cavity. For the comparison of theory and experiment, we reemphasize that the parameters $(g_0^{(m_F, m'_F)}, \gamma, \kappa, \Delta_{AC}, \omega_p - \omega_A, \Delta\nu_{C_1}, |\mathcal{E}_p|^2, U_0)$ are known in absolute terms without adjustment. However, we have no a priori knowledge of the particular FORT well into which the atom is loaded along the cavity standing wave, nor of the energy of the atom. The FORT shift and coherent coupling rate are both functions of atomic position $\mathbf{r}$, with

$$U(\mathbf{r}) = U_0 \sin^2(k_{C_2} z) \exp(-2\rho^2 / w_{C_2}^2), \tag{2.18}$$

$$g^{(m_F, m'_F)}(\mathbf{r}) = g_0^{(m_F, m'_F)} \psi(\mathbf{r}), \tag{2.19}$$

where $g_0^{(m_F, m'_F)} = g_0 G_{m_F, m'_F}$ with $G_{i,f}$ related to the Clebsch-Gordan coefficient for the particular $m_F \leftrightarrow m'_F$ transition. Here

$$\psi(\mathbf{r}) = \cos(k_{C_1} z) \exp(-\rho^2 / w_{C_1}^2), \tag{2.20}$$

where ρ is the transverse distance from the cavity axis z, and $k_{C_{1,2}} = 2\pi / \lambda_{C_{1,2}}$.

As discussed in connection with Fig. 2.15 below, for the theoretical curves shown in Figs. 2.13, 2.14, we have chosen only the 30 out of 90 total FORT wells for which $|\psi(\mathbf{r}_{\text{FORT}})| \geq 0.87$, where $\mathbf{r}_{\text{FORT}}$ is such that $U(\mathbf{r}_{\text{FORT}}) = U_0$. Furthermore, for these wells we have averaged $T_1(\omega_p)$ over a Gaussian distribution in position $\mathbf{r}$ consistent with a temperature $k_B \mathcal{T} = 0.1 U_0$ (~ 200 μK). Since all parameters are known except for those that characterize atomic motion, the good agreement between theory and
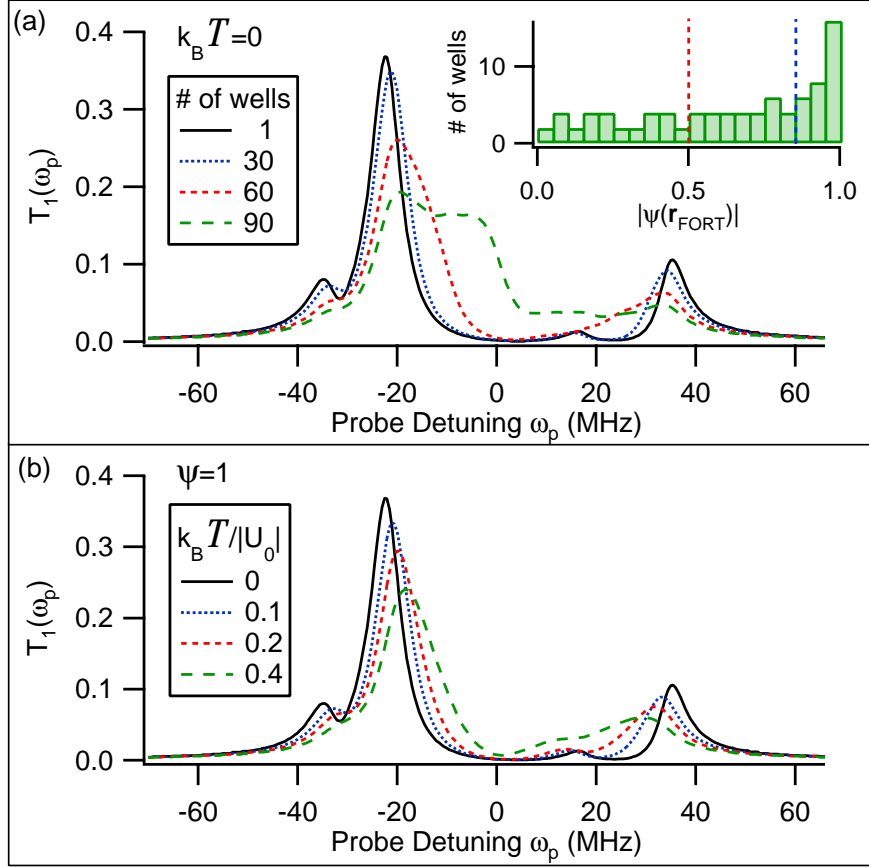
Figure 2.15: Theoretical plots for $T_1(\omega_p)$: (a) zero temperature, spectrum dependence on probe-FORT registration; (b) perfect registration, dependence on temperature.

experiment allows us to infer that our cooling protocol together with the selection criterion $T_{\text{thresh}} = 0.2$ results in individual atoms that are strongly coupled in one of the "best" FORT wells (i.e., $|\psi(\mathbf{r}_{\text{FORT}})| \gtrsim 0.87$) with "temperature" $\sim 200~\mu\text{K}$. In Figs. 2.13 and 2.14, the discrepancy between experiment and the *steady-state* theory for $\bar{T}_1(\omega_p)$ around $\omega_p \sim 0$ can be accounted for by a *transient* solution to the master equation which includes optical pumping effects over the probe interval Δt_{probe}. Also, although the spectra are consistent with a thermal distribution, we do not exclude a more complex model involving probe-dependent heating and cooling effects.

In support of these assertions, Fig. 2.15 (a) explores the theoretical dependence of $T_1(\omega_p)$ on the set of FORT wells selected, and hence on the distribution of values for $|\psi(\mathbf{r}_{\text{FORT}})|$ in the ideal zero-temperature case $\mathcal{T} = 0$. The transmission $T_1(\omega_p)$

predicted by the steady-state solution of the master equation is calculated from an average over various FORT antinodes along the cavity axis, with the inset showing the associated distribution of values for $|\psi(\mathbf{r}_{\text{FORT}})|$. Extending the average beyond the 30 "best" FORT wells leads to spectra that are inconsistent with our observations in Figs. 2.13 and 2.14. Fig. 2.15 (b) likewise investigates the theoretical dependence of $T_1(\omega_p)$ on the temperature $\mathcal{T}$ for an atom at an antinode of the FORT with optimal coupling (i.e., $|\psi(\mathbf{r})| = 1$). Now $T_1(\omega_p)$ is computed for various temperatures from an average over atomic positions within the well. For temperatures $\mathcal{T} \gtrsim 200$ μK, the calculated spectra are at variance with the data in Figs. 2.13 and 2.14, from which we infer atomic localization $\Delta z \simeq 33$ nm in the axial direction and $\Delta x = \Delta y \simeq 3.9$ μm in the plane transverse to the cavity axis. Beyond these conclusions, a consistent feature of our measurements is that reasonable correspondence between theory and experiment is only obtained by restricting $|\psi(\mathbf{r})| \gtrsim 0.8$.

Our experiment represents an important advance in the quest to obtain single atoms trapped with optimal strong coupling to a single mode of the electromagnetic field. The vacuum-Rabi splitting is the hallmark of strong coupling for single atoms and photons, and all measurements until now have required averaging over many atoms for its observation. By contrast, we are able to observe spectra $T_1(\omega_p)$ on an atom-by-atom basis with clearly resolved normal-mode splittings. These spectra contain detailed quantitative information about the coherent coupling $g(\mathbf{r})$ and FORT shifts for each atom. This information indicates that the coupling g is in a narrow range of near-maximal values. Our observations are made possible by the implementation of a new scheme to cool both the radial and axial atomic motion. The capabilities demonstrated by this experiment should provide the tools necessary to implement diverse protocols in quantum information science [19, 10, 11, 12, 20].

Chapter 3

Dark-mode up-goers and photon blockade

This chapter describes our recent experiment studying the photon statistics of light transmitted by the atom-cavity system when driven on the red vacuum-Rabi sideband. We start by introducing a simple theoretical model justifying the non-classical character of the emitted light field, and then we describe the experimental protocol and data analysis method in detail. We conclude by discussing the experimental results, including the observation of sub-Poissonian and anti-bunched photon statistics, as well as motional effects leading to an estimate of the atomic temperature.

3.1   Master equation, revisited

Let us go back to the simple theoretical model describing a two-level atom strongly coupled to a single cavity mode (see Sec. 2.1 and 2.2). Recalling the Jaynes-Cummings picture in Fig. 2.1, we see that the $|\pm\rangle_1$ states are separated by $2g$, whereas the $|\pm\rangle_2$ splitting is $2\sqrt{2}g$. Now suppose that the probe laser frequency is tuned to resonance with one of the vacuum-Rabi sidebands, say the red one at $\omega_P = \omega_A - g$. If the system is excited to the $|-\rangle_1$ state, then the anharmonicity of the ladder will make it difficult for another excitation to occur, since the probe light is detuned from state $|-\rangle_2$ by $(2 - \sqrt{2})g$, which, for strong coupling, is much greater than the state's linewidth. Since two-excitation atom-cavity states are unlikely to be populated, the probability of the cavity emitting two photons at the same time is sup-

pressed. One can think of this as a "photon blockade," in the sense that absorption of the first photon from an incoming Poissonian stream will block the absorption of a second one, leading to sub-Poissonian statistics in the output field. It can be shown (see e.g., Ref. [34], Sec. 12.10.3) that if the photon statistics for a light field are sub-Poissonian, the state of that field cannot be described by a classical probability functional. Hence, this state is interesting, from a quantum optics perspective.

For a more quantitative description of what is going on, let us consider the correlations between pairs of photons transmitted by the driven atom-cavity system. We will compute here the zero-delay second-order intensity correlation function $g^{(2)}(0)$, in the case of weak driving. Obviously the truncated three-state basis of Sec. 2.2 is insufficient for observing coincidences, so we will enlarge the state space to allow for two quanta of energy as well: $\{|g, 0\rangle, |g, 1\rangle, |e, 0\rangle \, |g, 2\rangle, |e, 1\rangle\}$. The Hamiltonian and master equation are still those from Eqns. (2.8) and (2.9), which we used in Chapter 2 to derive the vacuum-Rabi spectrum.

In this five-state basis, the only non-zero matrix elements for the relevant operators are:

$$
\begin{aligned}
\langle g, 1|a^\dagger \sigma_-|e, 0\rangle &= \langle e, 0|a\sigma_+|g, 1\rangle &= 1 \\
\langle g, 2|a^\dagger \sigma_-|e, 1\rangle &= \langle e, 1|a\sigma_+|g, 2\rangle &= \sqrt{2} \\
\langle e, 0|\sigma_+\sigma_-|e, 0\rangle &= \langle e, 1|\sigma_+\sigma_-|e, 1\rangle &= 1 \\
\langle g, 1|a^\dagger a|g, 1\rangle &= \langle e, 1|a^\dagger a|e, 1\rangle &= 1 \\
\langle g, 2|a^\dagger a|g, 2\rangle &= 2 \, .
\end{aligned}
\tag{3.1}
$$

Also, for weak driving $E/\kappa \ll 1$, the density operator for the atom-cavity system is of the form

$$
\rho = |\psi\rangle\langle\psi|,
\tag{3.2}
$$

that is, despite dissipation, the system can be described by a pure state [35, 36]:

$$
\psi = |g, 0\rangle + a_1|g, 1\rangle + a_2|e, 0\rangle + a_3|g, 2\rangle + a_4|e, 1\rangle \, ,
\tag{3.3}
$$

where the single and double excitation components scale linearly and quadratically, respectively, with the drive strength:

$$a_1, a_2 \propto \frac{E}{\kappa} \qquad\qquad a_3, a_4 \propto \left(\frac{E}{\kappa}\right)^2, \qquad (3.4)$$

so that $|\psi\rangle$ is normalized to first order in the drive strength. We can now use the master equation for ρ to derive equations of motion for the a_{1-4} coefficients. From the first column of the Liouvillian, keeping only terms to leading order in the drive parameter E/κ, we have:

$$
\begin{aligned}
\dot{a}_1 &= -(\kappa + i\delta_{CP})a_1 - iga_2 - iE \\
\dot{a}_2 &= -iga_1 - (\gamma + i\delta_{AP})a_2 \\
\dot{a}_3 &= -i\sqrt{2}Ea_1 - 2(\kappa + i\delta_{CP})a_3 - i\sqrt{2}ga_4 \\
\dot{a}_4 &= -iEa_2 - i\sqrt{2}ga_3 - (\gamma + i\delta_{AP})a_4 - (\kappa + i\delta_{CP})a_4 .
\end{aligned}
\qquad (3.5)
$$

Note that the first two equations in (3.5), describing the evolution of a_1 and a_2, are identical to Eqns. (2.14) for $\alpha = \langle a \rangle$ and $\beta = \langle \sigma_- \rangle$, which is not surprising since to first order in E/κ, $\alpha = a_1$ and $\beta = a_2$.

If all we are interested in is computing $g^{(2)}(0)$, then we only need the steady state solution, which we get by setting the left hand side of all equations in (3.5) to zero:

$$
\begin{aligned}
a_1^{ss} &= \frac{-iE\tilde{\gamma}}{g^2 + \tilde{\kappa}\tilde{\gamma}} \\
a_2^{ss} &= \frac{-Eg}{g^2 + \tilde{\kappa}\tilde{\gamma}} \\
a_3^{ss} &= \frac{E^2(g^2 - \tilde{\gamma}(\tilde{\kappa} + \tilde{\gamma}))}{\sqrt{2}(g^2 + \tilde{\kappa}\tilde{\gamma})(g^2 + \tilde{\kappa}(\tilde{\kappa} + \tilde{\gamma}))} \\
a_4^{ss} &= \frac{iE^2 g(\tilde{\kappa} + \tilde{\gamma})}{(g^2 + \tilde{\kappa}\tilde{\gamma})(g^2 + \tilde{\kappa}(\tilde{\kappa} + \tilde{\gamma}))} ,
\end{aligned}
\qquad (3.6)
$$

where we have defined $\tilde{\kappa} \equiv \kappa + i\delta_{CP}$ and $\tilde{\gamma} \equiv \gamma + i\delta_{AP}$. Note that all a_{1-4} coefficients have the correct scaling with the driving strength, consistent with Eqn. (3.4). Armed with this steady state solution, we can readily compute expectation values of
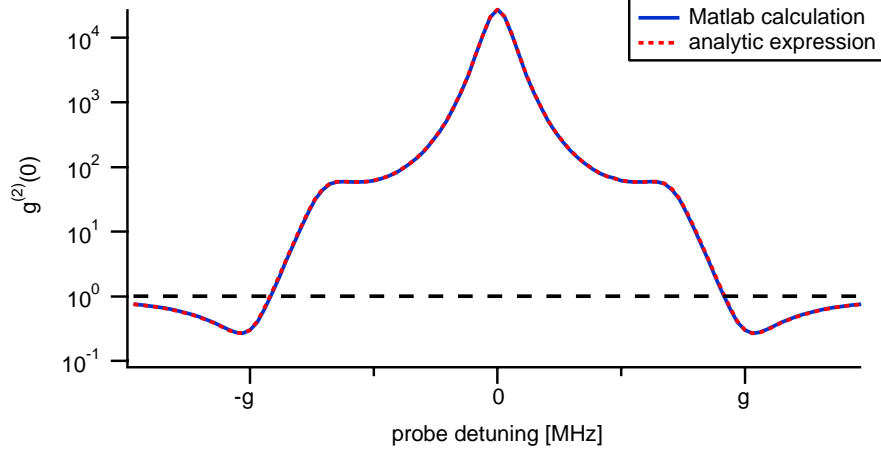
Figure 3.1: $g^{(2)}(0)$ as a function of probe detuning from the atomic resonance.

operators.

The second-order normalized intensity correlation function at zero delay is by definition given by

$$g^{(2)}(0) = \frac{\langle a^{\dagger 2} a^2 \rangle}{\langle a^\dagger a \rangle^2} , \qquad (3.7)$$

where the expectation value is to be taken in the steady state $|\psi\rangle^{ss}$ as set by Eqns. (3.6). Given the known scaling with the drive parameter from Eqn. (3.4), we find:

$$g^{(2)}(0) = \frac{2|a_3^{ss}|^2}{(|a_1^{ss}|^2 + 2|a_3^{ss}|^2 + |a_4^{ss}|^2)^2} \simeq \frac{2|a_3^{ss}|^2}{|a_1^{ss}|^4}, \qquad (3.8)$$

which for small E is independent of the driving strength.

This derivation was done with the help of *Mathematica* [37], and in the most part following Refs. [35, 36], which deal with the more general, many-atom case, and with delayed coincidences. These papers also have a different phase convention for a and $a^\dagger$, and a somewhat less algebra-intensive way of obtaining the steady-state solution, namely by first setting $\delta_{CP} = \delta_{AP} = 0$ in the Hamiltonian, and then only for the final result making the formal substitutions $\kappa \to \tilde{\kappa}$ and $\gamma \to \tilde{\gamma}$ (note the typo in Eqn. (38) of Ref. [36]).

Now we can evaluate $g^{(2)}(0)$, by plugging experimentally relevant parameter values into Eqns. (3.6) and (3.8). Fig. 3.1 shows the dependence of $g^{(2)}(0)$ on the probe's

detuning from atomic resonance, for $g = 2\pi \times 34$ MHz, $\kappa = 2\pi \times 4.1$ MHz, $\gamma = 2\pi \times 2.6$ MHz, and $\delta_{CP} = \delta_{AP}$. Note in the region near $\delta_{CP} = \delta_{AP} = \pm g$, the curve dips below the dashed line at unity, i.e., $g^{(2)}(0) < 1$, reaching a minimum of $g^{(2)}(0) \simeq 0.27$. This means that if we drive the atom-cavity system on either of the two vacuum-Rabi sidebands (recall Fig. 2.2), the emerging photon stream will exhibit sub-Poissonian statistics. This is precisely what we implied in the intuitive discussion at the beginning of this section.

Fig. 3.1 also shows the result of a numerical Matlab [38, 39] calculation[1], using Kevin Birnbaum's jaynescummings_w_suffix.m script [9]. The code uses a truncated six-state space $\{|g\rangle, |e\rangle\} \otimes \{|0\rangle, |1\rangle, |2\rangle\}$, and a drive strength of $E/\kappa = 0.01$ (empty cavity photon number on resonance $(E/\kappa)^2 = 10^{-4}$). Note that the two curves in Fig. 3.1 represent nearly the same weak-field approximation, so not surprisingly they are very close (almost indistinguishably so in the log-scale figure), differing by at most 5% over the entire range of possible detunings.

The experimental results we present in Sec. 3.6 show that the photon stream emerging from our real-life atom-cavity system also has manifestly non-classical statistics near the red vacuum-Rabi sideband, as evidenced by the sub-Poissonian and anti-bunched character of the detected light. The model which quantitatively predicts a value for $g^{(2)}(0)$ consistent with what we observe in the lab is rather complicated [9]. However, our simple model presented above is sufficient to predict the qualitative behavior of the system, namely the non-classical character of the photon statistics at the cavity output.

---

[1]This curve also appears in Sec. 3.6 Fig. 3.16 (a), for slightly different parameters $g = 2\pi \times 33.9$ MHz and $E/\kappa = 0.1$. Please also see discussion therein.
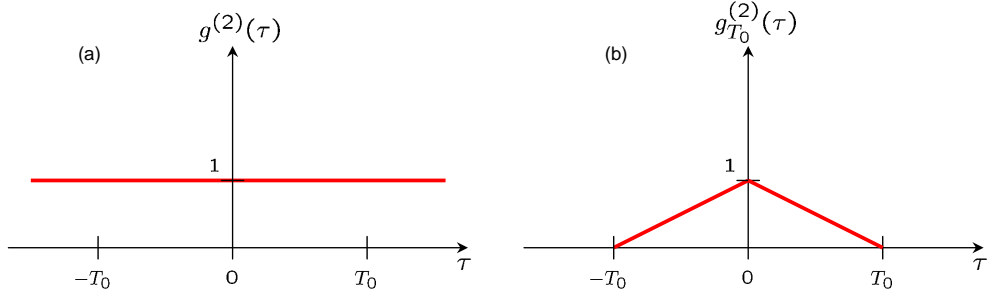
Figure 3.2: Second-order normalized intensity correlation function for (a) a constant signal; (b) a square pulse.

3.2 Turning coincidences into $g^{(2)}(\tau)$

The normalized second-order intensity correlation function corresponding to a classical field of intensity $I(t)$ is defined as

$$g^{(2)}(t,\tau) = \frac{\langle I(t)I(t+\tau)\rangle}{\langle I(t)\rangle\langle I(t+\tau)\rangle} \,, \tag{3.9}$$

where the $\langle\ \rangle$ brackets denote ensemble averages. Often one deals with stationary processes, for which the ensemble averages do not depend on the origin of time, making $g^{(2)}(t,\tau)$ is a function of τ alone. Also, the field is usually ergodic, meaning that ensemble averages can be replaced by averages over all time:

$$\langle I(t)I(t+\tau)\rangle = \lim_{T\to\infty}\frac{1}{T}\int_{-T/2}^{T/2}I(t)I(t+\tau)\,\mathrm{d}t$$

$$\langle I(t)\rangle = \langle I(t+\tau)\rangle = \lim_{T\to\infty}\frac{1}{T}\int_{-T/2}^{T/2}I(t)\,\mathrm{d}t\,. \tag{3.10}$$

For times long compared with the coherence time of the signal, the numerator in Eqn. (3.9) factorizes, so that the normalized intensity correlation function asymptotes to unity:

$$\langle I(t)I(t+\tau)\rangle = \langle I(t)\rangle\langle I(t+\tau)\rangle \implies g^{(2)}(\tau\to\infty) = 1. \tag{3.11}$$

As an example, let us consider a constant signal, $I(t) = I_0$ for all time. Then trivially from Eqns. (3.9, 3.10), we find $g^{(2)}(\tau) = 1$ identically.

The trouble with this picture is that one cannot sample a signal for all time; rather, one would typically measure it for a finite interval of length T_0, and construct signal averages in the following way:

$$\langle I(t)I(t+\tau)\rangle_{T_0} = \frac{1}{T_0} \int_{-T_0/2}^{T_0/2} I(t)I(t+\tau)\,dt$$

$$\langle I(t)\rangle_{T_0} = \langle I(t+\tau)\rangle_{T_0} = \frac{1}{T_0} \int_{-T_0/2}^{T_0/2} I(t)\,dt, \tag{3.12}$$

where the corresponding normalized correlation function is

$$g_{T_0}^{(2)}(\tau) = \frac{\langle I(t)I(t+\tau)\rangle_{T_0}}{\langle I(t)\rangle_{T_0}^2}. \tag{3.13}$$

Here $|\tau| < T_0$, and $I(t)$ is assumed to be non-zero only in the interval $[-T_0/2, T_0/2]$. How is this $g_{T_0}^{(2)}(\tau)$ related to the correlation function for the stationary process that is being sampled, i.e., to $g^{(2)}(\tau)$ evaluated in the interval $\tau \in [-T_0, T_0]$? The example of constant intensity we considered above now becomes a square pulse, with $I(t) = I_0$ for $|t| < T_0/2$, and zero elsewhere. From (3.13), we find that the finite-interval correlation function is

$$g_{T_0}^{(2)}(\tau) = 1 - |\tau|/T_0. \tag{3.14}$$

Thus the finite sampling time has the effect of putting a triangular shape on an inherently constant correlation function, as shown in Fig. 3.2. Because of that, one will often compensate for this triangle effect, by multiplying a measured correlation function by the factor $T_0/(T_0 - |\tau|)$. The result then has the asymptotic behavior one would expect from a stationary process (see Eqn. 3.11), albeit with increasing fluctuations as we near $|\tau| = T_0$ where the multiplication factor diverges.

So far we have dealt with analog, continuous signals. In the lab, however, we have single-photon counters, which give us a time stamp for each photon arrival at the detectors. If we have the time record corresponding to a single light pulse of duration T_0, we can divide T_0 into N bins of duration δ each. Now let the number of clicks recorded in the kth bin be a_k, with $k = 1, \ldots, N$, and let $\tau = j\,\delta$, with

$j = -N + 1, \ldots, N - 1$. The discretized version of Eqn. (3.12) is:

$$\langle I(t)I(t + \tau)\rangle_N = \frac{1}{N}\sum_{k=1}^{N} a_k a_{k+j}$$

$$\langle I(t)\rangle_N = \langle I(t + \tau)\rangle_N = \frac{1}{N}\sum_{k=1}^{N} a_k\,, \tag{3.15}$$

with normalized intensity correlation function given by

$$g_N^{(2)}(\tau) = \frac{\langle I(t)I(t + \tau)\rangle_N}{\langle I(t)\rangle_N^2}\,. \tag{3.16}$$

Ideally one single-photon detector would suffice for measuring the autocorrelation of the incoming light field. However, real detectors have non-trivial autocorrelations (see Sec. 2.3.1 of Ref. [1]). First, there is the dead time: after recording a photocount, our detectors take about $\tau_{DT} = 53$ ns to recover before they can detect the next photon. This means that if one is interested in correlations for times shorter than the dead time $|\tau| < \tau_{DT}$, one needs two detectors. Secondly, there is the problem of after-pulsing, whereby about 1.2% of the time, the detector records not one, but two counts per incoming photon. This means that, for accurate field intensity autocorrelation measurements, one should only consider the cross-correlation of the click times coming from two different detectors, and ignore those coincidences corresponding to one and the same detector.

By extension of the single-detector picture, let the number of clicks in the kth bin coming from each of the two detectors be a_k and b_k. Then Eqn. (3.15) can be updated for the two-detector, cross-correlation case:

$$\langle I_A(t)I_B(t + \tau)\rangle = \frac{1}{N}\sum_{k=1}^{N} a_k b_{k+j}$$

$$\langle I_A(t)\rangle = \frac{1}{N}\sum_{k=1}^{N} a_k \tag{3.17}$$

$$\langle I_B(t)\rangle = \frac{1}{N}\sum_{k=1}^{N} b_k\,.$$

Then the normalized correlation function becomes

$$g^{(2)}(\tau) = \frac{\langle I_A(t) I_B(t+\tau) \rangle}{\langle I_A(t) \rangle \langle I_B(t) \rangle} = N \frac{\sum a_k b_{k+j}}{(\sum a_k)(\sum b_k)} = N \frac{C(\tau)}{AB}, \tag{3.18}$$

where we have defined the total number of clicks recorded by each detector in the T_0 interval, and the coincidences in the jth bin, as:

$$A = \sum_k a_k \qquad B = \sum_k b_k \qquad C(j\delta) = \sum_k a_k b_{k+j}, \tag{3.19}$$

respectively. So there are three main ingredients in $g^{(2)}(\tau)$. First is the number of bins N into which we have chosen to divide the T_0 interval. Then, there are the "raw" coincidences, i.e., the unnormalized correlation function, $C(\tau) = C(j\delta)$. Finally, there is the product AB, a normalization constant representing the total number of coincidences in the data set (ignoring triangle effects as discussed around Eqn. (3.2)), i.e., $C(\tau)$ integrated over all values of τ:

$$\sum_j C(j\delta) = \sum_{j=-N+1}^{N-1} \sum_{k=1}^{N} a_k b_{k+j} = \sum_{k=1}^{N} a_k \sum_{j=1-k}^{N-k} b_{k+j} = \sum_{k=1}^{N} a_k \sum_{i=1}^{N} b_i = AB. \tag{3.20}$$

One can always pick δ small enough that each bin contains at most one click from each detector. For instance, since our detectors produce no clicks in the dead time interval, for any $\delta < \tau_{DT}$, we know that a_k and b_k can only take the values 0 or 1. In this case, the coincidence function $C(j\delta)$ is just a histogram of time separations between clicks in the two channels, which makes it easier to compute in data analysis (see Sec. 3.5).

Often the recorded counts come not only from the field for which we are interested in measuring the correlation function, but also from some additional background signal. In that case, one might wish to extract the correlation function $g_s^{(2)}(\tau)$ corresponding to the underlying signal from the measured coincidences $C(\tau)$. This can be easily done if the background comes in at a constant rate, without nontrivial correlations, as is the case with, for instance, detector dark counts. If the background

is responsible for A_b and B_b clicks in the interval T_0 from each of the two detectors, evenly distributed among the N bins, then in terms of the measured counts a_k and b_k, the expected counts associated with the signal are:

$$a_k^s = a_k - \frac{A_b}{N} \qquad\qquad b_k^s = b_k - \frac{B_b}{N}. \qquad (3.21)$$

For notational simplicity, let us for the moment restrict ourselves to $\tau = 0$, so that the desired normalized correlation is

$$g_s^{(2)}(0) = N\,\frac{C^s(0)}{(\sum a_k^s)(\sum b_k^s)}, \qquad (3.22)$$

where $C^s(0) = \sum a_k^s b_k^s$ gives the coincidences associated with the underlying signal alone, in the absence of background. Then if the measured, raw coincidences from the recorded counts are given by $C(0) = \sum a_k b_k$, using (3.21) we find:

$$
\begin{aligned}
C^s(0) &= C(0) - \frac{A_b}{N}\sum_k b_k - \frac{B_b}{N}\sum_k a_k + N\frac{A_b}{N}\frac{B_b}{N} \\
&= C(0) - \frac{1}{N}(A_b B + A B_b - A_b B_b) \qquad (3.23) \\
&= \frac{1}{N}(NC(0) - C_b).
\end{aligned}
$$

Here we have defined the quantity $C_b = A_b B + B_b A - A_b B_b$, which is related to the contribution background counts have to the measured correlations. Again with the help of (3.21), we can rewrite the denominator of $g_s^{(2)}(0)$ as follows:

$$\left(\sum_k a_k^s\right)\left(\sum_k b_k^s\right) = (A - A_b)(B - B_b) = AB - C_b. \qquad (3.24)$$

Putting together the results from (3.23) and (3.24) into (3.22), and generalizing to non-zero delays, we now know how to compensate for the background contribution to the correlation function. We get that the normalized correlation function $g_s^{(2)}(\tau)$ corresponding to the signal alone, inferred from the measured coincidences including

background $C(\tau)$, is:

$$g_s^{(2)}(\tau) = \frac{NC(\tau) - C_b}{AB - C_b}.$$ (3.25)

Note that if we set $A_b = B_b = 0$, then $C_b = 0$ as well, and we recover the expression for the normalized second-order correlation function of the recorded clicks, in the absence of any background compensation, consistent with (3.18).

It is easy to show, based on (3.25) and (3.18), that the following must hold true:

$$g^{(2)}(\tau) = 1 \quad \Longrightarrow \quad g_s^{(2)}(\tau) = 1$$
$$g^{(2)}(\tau) < 1 \quad \Longrightarrow \quad g_s^{(2)}(\tau) < g^{(2)}(\tau)$$ (3.26)
$$g^{(2)}(\tau) > 1 \quad \Longrightarrow \quad g_s^{(2)}(\tau) > g^{(2)}(\tau).$$

In other words, removing the contribution of a Poissonian background does not change the value of $g^{(2)}$ when the latter corresponds to uncorrelated statistics. However, the sub- and super-Poissonian character of the statistics are enhanced after the background correlations are compensated for.

So far we have dealt with a single data record of duration T_0, which in our experiment would correspond to a single probe trial, typically on the order of 500μs long. The counting rates per trial are rather low, typically a few kHz per detector, meaning only a few counts per pulse. Thus to obtain a statistically significant $g^{(2)}$, we would need to take data for many such probe pulses, and somehow average them all up. How would one go about computing the correlation function, based on many uncorrelated trials?

One proposed way of solving this problem, suggested by Jeff Kimble, would be to formally concatenate all the pulses into one long time record. So if we have N_p square pulses of length T_0 each, we would obtain one interval of length N_pT_0, and go about computing $g^{(2)}$ as outlined above in Eqn. (3.25). I have not yet used this method for analyzing the data in Sec. 3.6, though it sounds like a reasonable thing to try in the near future.

Another possibility, suggested by Kevin Birnbaum, would be to compute a sepa-

rate normalized $g^{(2)}(\tau)$ for each of the N_p trials, and then average the results. Ignoring background for the moment, let the number of clicks in the kth bin in the ith trial from the two detectors be a_k^i and b_k^i. Then the unnormalized correlation function for the ith interval is $C^i(\tau = j\delta) = \sum_k a_k^i b_{k+j}^i$, whereas the normalized correlation for that same interval is, as in Eqn. (3.18)

$$g_i^{(2)}(\tau) = \frac{NC^i(\tau)}{A_i B_i}, \tag{3.27}$$

where we have defined the total number of clicks in each interval as A^i and B^i:

$$A^i = \sum_k a_k^i \qquad\qquad B^i = \sum_k b_k^i. \tag{3.28}$$

Then the normalized correlation function for the entire data set made up of N_p trials would be computed as

$$g^{(2)}(\tau) = \frac{1}{N_p} \sum_{i=1}^{N_p} g_i^{(2)}(\tau). \tag{3.29}$$

The problem with doing this is that, due to the sparsity of the count record, for each of the correlation functions $g_i^{(2)}(\tau)$ to be averaged, we take the ratio of two small numbers: $C^i(\tau)$ and $A_i B_i$, hence the fluctuations will be large, washing out the interesting signal in $g^{(2)}(\tau)$.

An alternative would be to first compute the unnormalized correlation function for each of the N_p intervals, add them all up, and only then divide by an appropriate normalization constant. The coincidences for the entire data set are given by

$$C(\tau) = \sum_{i=1}^{N_p} C^i(\tau). \tag{3.30}$$

As for the normalization constant, the discussion around Eqn. (3.18) suggests that we should use the total number of coincidences that get histogrammed by the various $C^i(\tau)$ functions, or equivalently the integral of $C(\tau)$ over all values of τ, which is
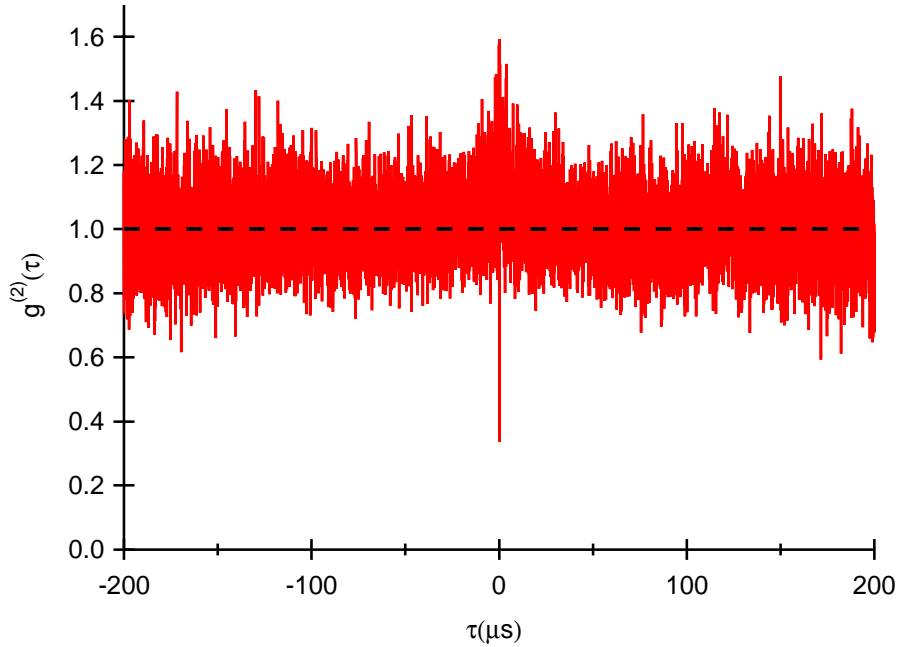
Figure 3.3: $g^{(2)}(\tau)$ on a long time scale for dark-mode up-goer data, where the asymptotic value is used as a check of the normalization method.

$\sum_i A_i B_i$. Then the normalized correlation function is given by

$$g^{(2)}(\tau) = N \frac{C(\tau)}{\sum A_i B_i} . \tag{3.31}$$

There is a different, but equivalent way of arriving at the above formula (3.31). We start out with the normalized intensity correlation functions $g_i^{(2)}(\tau)$ for each of the N_p intervals, defined in (3.27). But instead of doing an unweighted average as in (3.29), we can weigh each $g_i^{(2)}$ by the total number of coincidences in the ith trial, namely $A_i B_i$. Since more weight is given to those trials that have more data, we don't run into the problem of large fluctuations any more. The normalized correlation function for the entire data set, obtained through this weighted averaging, is:

$$g^{(2)}(\tau) = \frac{\sum A_i B_i \, g_i^{(2)}(\tau)}{\sum A_i B_i} , \tag{3.32}$$

which one can easily check is the same as the expression in (3.31).
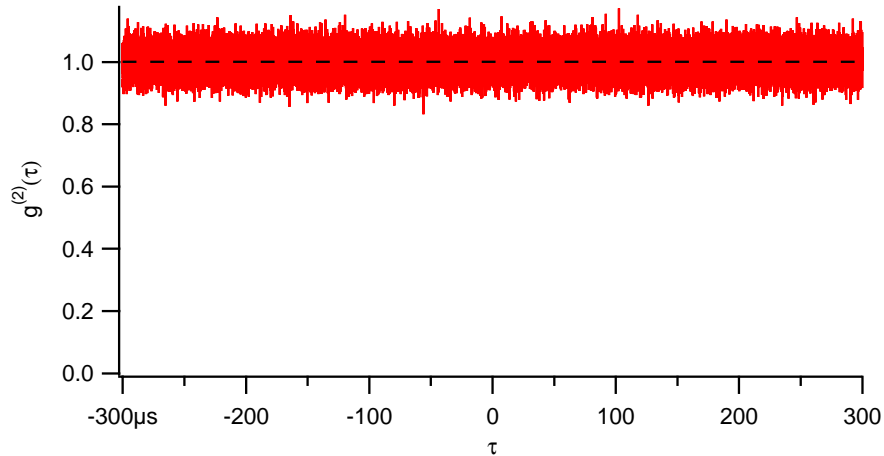
Figure 3.4: $g^{(2)}(\tau)$ on a long time scale, for flashlight data, with the asymptotic value used as a check of the normalization method.

One way to confirm that the above-outlined normalization does indeed make sense is to check that the asymptotic value of $g^{(2)}(\tau)$ is 1. As an example, Fig. 3.3 shows $g^{(2)}(\tau)$ computed for the data set[2] discussed in Sec. 3.6. The bin size used here is $\delta = 40$ ns, and the trial duration is $T_0 = 500$ μs. The correlation function has been adjusted for the finite trial duration effect, by multiplying it by a $T_0/(T_0 - |\tau|)$ factor – see Eqn. (3.14). For the purposes of this section, we are not interested in how exactly the data was acquired, or in the structure around $\tau = 0$; instead, we want to check that $g^{(2)}(\tau) \rightarrow 1$ as $\tau \rightarrow \infty$. And indeed, for the displayed data, the average value of $g^{(2)}(\tau)$ over the interval $\tau = 100 - 200$ μs is 1.000 ± 0.002, consistent with the expected value of unity.

Another example, for a quieter light source, is shown in Fig. 3.4. The detectors were illuminated by a flashlight[3], which for the purposes of this discussion is a thermal light source of extremely short correlation time. The bin size is $\delta = 10$ ns, and again we compensated for the triangle effect. Perhaps more convincingly than in Fig. 3.3, $g^{(2)}(\tau)$ asymptotes to unity, with the long-timescale value, as given by the average between $\tau = 200$ μs and $\tau = 300$ μs, being 1.0000 ± 0.0004.

We are now in the position to subtract the contribution of a Poissonian background

---

[2]Measurement date: 3/10/05.
[3]Measurement date: 1/24/05.

in the many-trial case. As before, we can assume that the number of clicks recorded in the ith trial by each of the two detectors is A_i and B_i; however, part of those are background counts, which are assumed to be recorded by each detector at constant rates A_b and B_b per trial. We are interested in the normalized intensity correlation function $g_s^{(2)}$ associated with the underlying signal, whose contribution in the ith trial is $A_i^s = A_i - A_b$ and $B_i^s = B_i - B_b$ clicks per detector. We know from (3.23) that for each individual trial, the unnormalized correlation function $C_s^i(\tau)$ for the signal is given by $NC_s^i(\tau) = NC^i(\tau) - C_b^i$, where $C_b^i = A_b B_i + A_i B_b - A_b B_b$. Thus, from (3.31):

$$
\begin{aligned}
g_s^{(2)}(\tau) &= \frac{N \sum C_s^i(\tau)}{\sum A_i^s B_i^s} \\
&= \frac{\sum (NC^i(\tau) - C_b^i)}{\sum (A_i B_i - C_b^i)} \\
&= \frac{NC(\tau) - C_b}{\sum A_i B_i - C_b},
\end{aligned} \tag{3.33}
$$

where we have identified the quantity

$$
C_b = \sum_{i=1}^{N_p} C_b^i = A_b \sum_{i=1}^{N_p} B_i + B_b \sum_{i=1}^{N_p} A_i - N_p A_b B_b \tag{3.34}
$$

as the background contribution to the coincidences.

The error bars on $g^{(2)}(0)$ can be computed using standard error-propagation techniques [40]. If we denote by σ_x the standard deviation associated with the random variable x, then in general, for uncorrelated u and v, we have the following:

$$
\begin{aligned}
\sigma_{u+v}^2 &= \sigma_u^2 + \sigma_v^2 \\
\sigma_{uv}^s &= \sigma_u^2 v^2 + \sigma_v^2 u^2 \\
\sigma_{u/v}^2 &= (u/v)^2 ((\sigma_u/u)^2 + (\sigma_v/v)^2).
\end{aligned} \tag{3.35}
$$

For instance, from Eqn. (3.31), the normalized correlation function at zero delay,

without any background corrections, is given by

$$g^{(2)}(0) = \frac{NC(0)}{\sum A_i B_i},$$

(3.36)

so by applying rules (3.35) several times, we get:

$$\left(\sigma_{g^{(2)}(0)}/g^{(2)}(0)\right)^2 = \frac{1}{C(0)} + \frac{\sum A_i B_i (A_i + B_i)}{(\sum A_i B_i)^2},$$

(3.37)

where we have assumed that $C(0)$, A_i, and B_i are Poisson variables, hence with $\sigma_{C(0)}^2 = C(0)$, $\sigma_{A_i}^2 = A_i$, and $\sigma_{B_i}^2 = B_i$, and that they are all statistically independent. This latter assumption means that the calculated value of $\sigma_{g^{(2)}(0)}$ is only a first-order approximation, where a more careful treatment would also be taking into consideration the correlations between A_i and B_i.

If we now take into consideration the background contribution to the coincidences, and assume that at each detector, the measured background rate is $\gamma_A = A_b/T_0$ and $\gamma_B = B_b/T_0$ counts per second, then the error bar on C_b is, from (3.34) and (3.35):

$$\begin{aligned}
\sigma_{C_b}^2 &= T_0^2 (\gamma_A (\sum B_i)^2 + \gamma_A^2 \sum A_i + \gamma_B (\sum A_i)^2 + \gamma_B^2 \sum A_i \\
&\quad + N_p^2 T_0^2 \gamma_A \gamma_B (\gamma_A + \gamma_B)).
\end{aligned}$$

(3.38)

As for the normalized correlation function at zero delay with background contribution removed, we see from (3.33) that it is given by:

$$g_s^{(2)}(0) = \frac{NC(0) - C_b}{\sum A_i B_i - C_b},$$

(3.39)

so by repeated application of relations (3.35), we find:

$$\left(\sigma_{g_s^{(2)}(0)}/g_s^{(2)}(0)\right)^2 = \frac{N^2 C(0) + \sigma_{C_b}^2}{(NC(0) - C_b)^2} + \frac{\sum A_i B_i (A_i + B_i) + \sigma_{C_b}^2}{(\sum A_i B_i - C_b)^2}.$$

(3.40)

The final result for $g_s^{(2)}(\tau)$ in Eqn. (3.33), together with the error estimate in (3.40), are what we use in the data analysis program in Sec. 3.5 for computing the
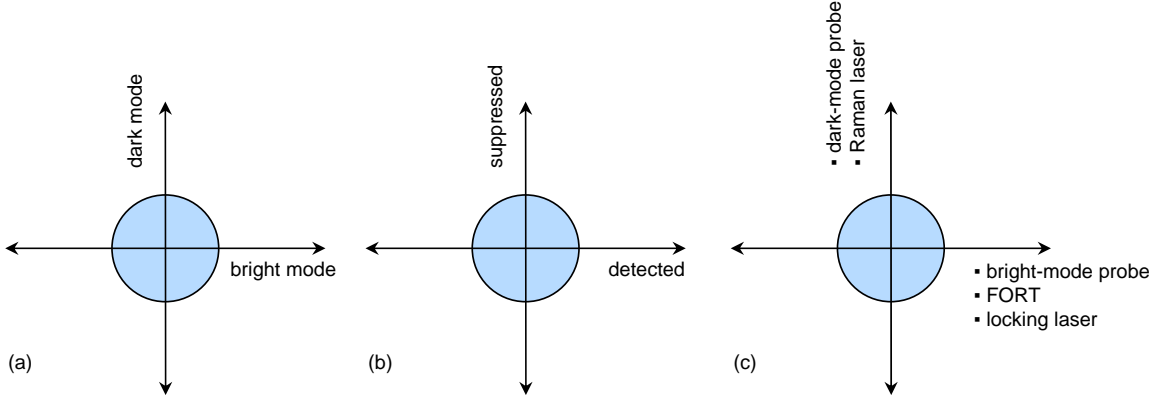
Figure 3.5: Cartoon representation of: (a) cavity eigenmode polarizations; (b) output polarizer axes; (c) beam polarizations at the cavity input.

normalized second order intensity correlation function and its standard deviation, as cited in Sec. 3.6.

3.3 Experimental protocol

Our cavity supports two independent eigenmodes with orthogonal polarization axes (also see Sec. 4.6), both of which couple to the atom within, but only one of which we select for detection with the output polarization optics. We refer to this detected mode as the "bright" mode, since when the empty cavity is on resonance, we detect a lot of light. We often speak of the orthogonal mode as the "dark" mode, since the polarizer at the cavity output prevents the empty cavity transmission in this mode from reaching the detectors. Fig. 3.5 shows an on-axis view of our cavity, including the directions of polarization for the various beams which get coupled into the cavity.

To start with, since the cavity is locked in transmission, the locking laser needs to go through the cavity and past the output polarizer, so we always align the locking beam's polarization with that of the bright mode. A second beam we use is a cavity QED probe on resonance with the $F = 4 \rightarrow F' = 5'$ atomic transition, i.e., with $\delta_{AP} = 0$. This beam drives the bright cavity mode, hence we have dubbed it the bright-mode probe. The cavity is locked in such a way as to maximize the bright-mode

probe transmission, therefore the cavity is also resonant with the atomic transition. In addition to the bright-mode probe, we use a second probe beam, typically red-detuned from $4 \rightarrow 5'$ by $\delta_{AP} = 2\pi \times 34$ MHz, and polarized so as to drive the orthogonal mode, hence referred to as the dark-mode probe. Finally, as shown in panel (c), the trapping and the Raman beams have polarizations orthogonal to one another. What do we expect the transmission of our atom-cavity system to be, when driven by either of the probe beams?

Recalling the Jaynes-Cummings model shown in Fig. 2.2, we see that for $\delta_{AP} = 0$ the presence of an atom in the cavity makes the probe transmission go down drastically compared with the empty-cavity value. This is why in cavity QED jargon we call this phenomenon a "down-goer." From Eqn. (2.16) it follows that for a two-level, single-mode system, the contrast between the transmission for the empty cavity with $g = 0$, and that when an atom is present, with $g \neq 0$, is $(1 + g^2/\kappa\gamma)^2$, which for $g \gg (\kappa, \gamma)$ is a large number. Thus a probe tuned to the down-goer setting, such as our bright-mode probe, is a good atom detector for our system.

If instead the probe were to be tuned near either of the vacuum-Rabi sidebands at $\delta_{AP} = \pm g$, its transmission in the presence of an atom would increase significantly compared to the empty-cavity value, hence the name "up-goer." Since the location of the vacuum-Rabi peaks depends on the value of the coupling strength g, the cavity transmission for a probe tuned for an up-goer is quite sensitive to changes in g. In particular, as the atom rolls around in the intra-cavity trap, it experiences a changing coupling constant (see Fig. 2.6), which will manifest itself as an amplitude modulation on the cavity output. So up-goers are a good way of sensing the atomic motion. In addition, as we saw in Sec. 3.1, this probe detuning is good for creating non-classical states of the light field via photon blockade.

So far in this chapter we have only considered a single-mode cavity, but as we shall see in Secs. 3.4 and 3.6, all the above features related to the up-goer setting still hold in a real, two-mode cavity. In addition, the predicted $g^{(2)}(0)$ value corresponding to driving one cavity mode and detecting the other is much lower than that corresponding to either a single-mode cavity, or to a two-mode cavity driven and detected in the
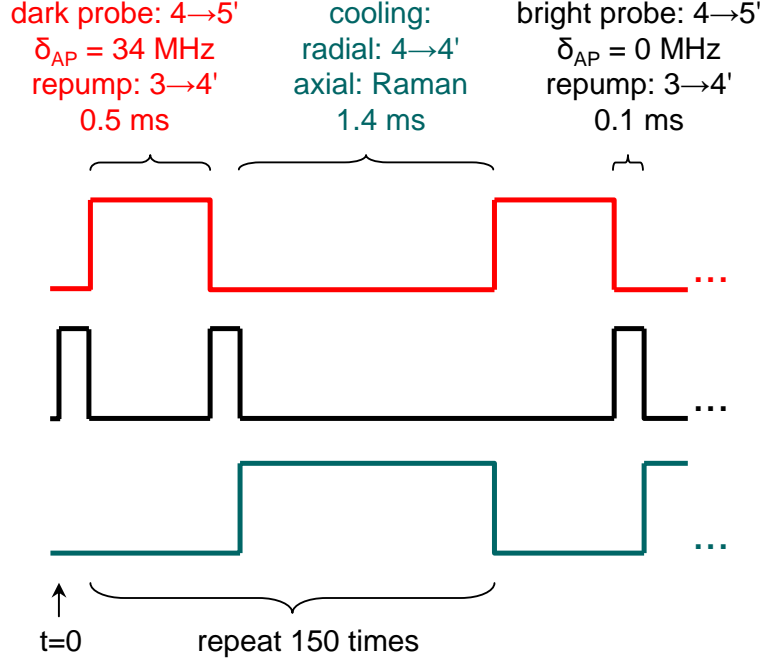
Figure 3.6: Typical timing diagram for a dark-mode up-goer experiment.

same mode [8]. The sub-Poissonian character of the photon statistics is hence much more robust in the former case, which is why, for our up-goer probe, we use the dark mode.

A typical timing scheme for the experiments outlined in this chapter is shown schematically in Fig. 3.6. We use brief 100 μs intervals of bright probing as a way of testing for down-goers, i.e., for atomic presence, throughout the observation period. Each bright-mode interval is called a "trial," which is considered successful if in data analysis it is determined that an atom was present during the trial (more on this topic below). The bright-mode pulses alternate with longer intervals of dark-mode probing, of duration $T_0 = 0.5 - 5$ ms, from which we extract photon statistics to construct the $g^{(2)}(\tau)$ function. Since all these probing intervals are likely to heat the atom, we try to compensate by cooling it both axially and radially, using the same scheme as in Ref. [7]. The particular timing diagram in Fig. 3.6 corresponds to the settings in Sec. 3.6; the most notable variations from one data set to another in this chapter, as far as the timing scheme is concerned, consist of omitting the interval devoted to

cooling, and leaving the dark probe on for longer, up to 5 ms.

We define $t = 0$ as the time when the P7888 data acquisition card in our computer is triggered to start counting incoming pulses. In addition to the pulses from the two single-photon detectors, we also use the P7888 to acquire a time stamp at the beginning of each dark-mode probing interval, in order to compensate for any drifts between the computer time and that of the rest of the experiment, the latter of which is set by the ADwin system.

The first bright-mode pulse starts at $t = 0$ and is used for determining the loading rate, i.e., the probability that one or more atoms are loaded into the trap each time the lower MOT is dropped onto the cavity. We sometimes call each such loading attempt a "drop." We have had some evidence [5, 3] that the loading process is Poissonian, in which case if the average number of atoms loaded per attempt is $\bar{n}$, then the probability to load n atoms is given by:

$$p_n = \frac{\bar{n}^n}{n!} e^{-\bar{n}}. \tag{3.41}$$

If the loading probability is α, then

$$\alpha = 1 - p_0 = 1 - e^{-\bar{n}} \implies \bar{n} = -\ln(1 - \alpha), \tag{3.42}$$

from which we find the probability to load n atoms, in terms of the loading rate α:

$$p_n = (1 - \alpha) \frac{(-\ln(1 - \alpha))^n}{n!}. \tag{3.43}$$

In order to illustrate our method for deciding whether a particular trial was successful or not, we show in Fig. 3.7 two examples[4] of click histograms for the bright-mode probing interval. For each total number of counts that has been detected by the two APDs over a 100 μs pulse, the histogram shows how many times that number of counts actually occurred throughout the given data set. For panel (a), the loading rate was later determined to be $\alpha = 0.098$, whereas for (b), $\alpha = 0.865$. Note first that

---

[4]Measurement date: 2/3/05.
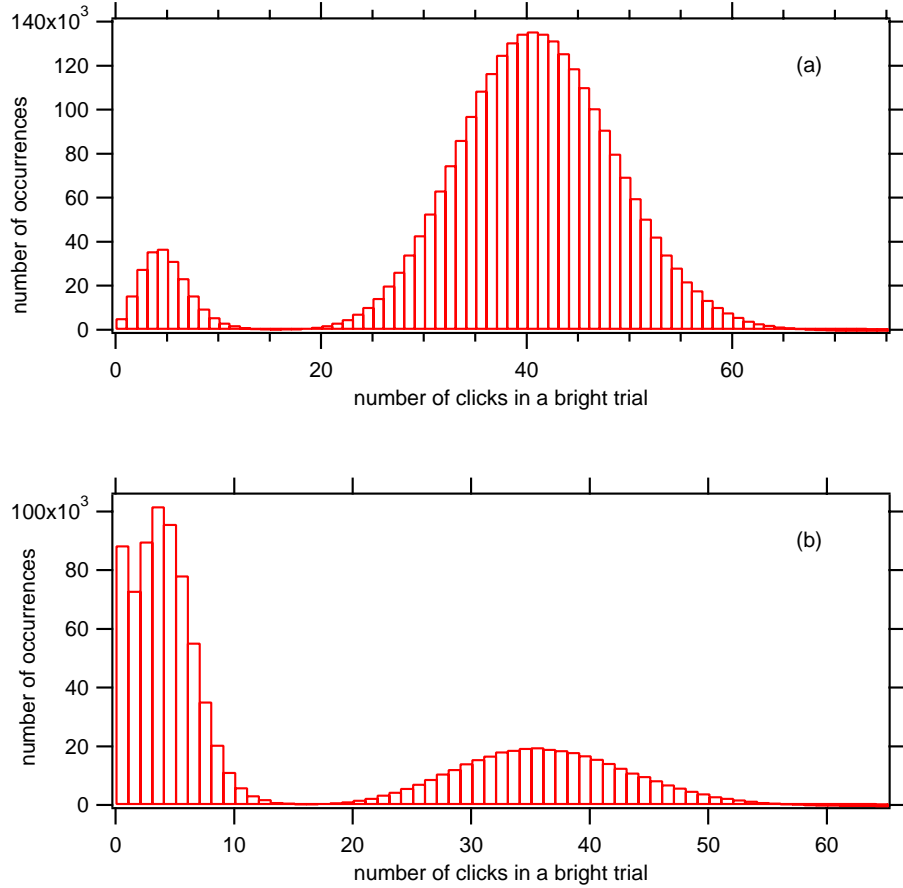
Figure 3.7: Histogram of counts per bright-mode probing pulse for (a) low and (b) high loading rate.

for the low loading rate case in (a), there are two well-resolved peaks, a taller one centered at about 40 counts per 100 μs, and another smaller one at about 4 counts per 100 μs. We identify the former as corresponding to the empty-cavity bright-mode probe transmission, and the latter to the coupled atom-cavity transmission. Clearly for this data set we can set an atom-detection threshold at about 25% of the empty-cavity transmission: if for a particular trial, and for all preceding trials within that drop, the transmission dipped below the threshold, the trial is considered to be successful, and the dark-mode interval following it is considered useful cavity QED data. This same threshold is subsequently used to determine the loading rate quoted above for panel (a), from which one can infer based on Eqn. (3.43) that about 9.3% of loading attempts result in a single atom being loaded, about 0.5% are two-atom
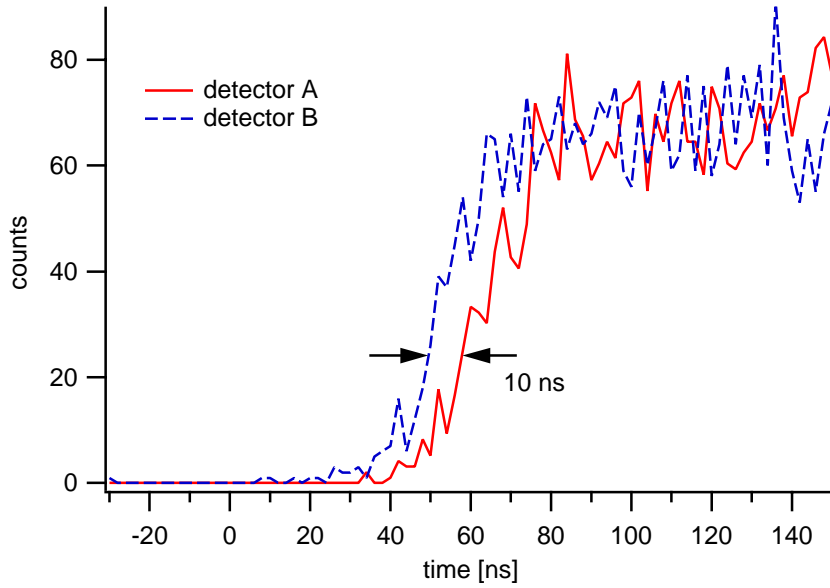
Figure 3.8: Clicks recorded by the P7888 card for channels A and B, given a laser pulse input for the fiber coupler.

loading events, and all other atom numbers are negligible. In panel (b) we notice the same separation between the empty and the full cavity, enabling us again to set a threshold for determining successful trials. However in this case the peak corresponding to low transmission has some structure, presumably associated with multi-atom events, which according to Eqn. (3.43) constitute almost 60% of all loading attempts.

The width of the empty-cavity peak in the histogram, as given by its best Gaussian fit, is somewhat larger than what one would expect from Poissonian statistics in the number of clicks per bright-mode trial. For instance, in Fig. 3.7 (a), the standard deviation is ~ 7.5, whereas the square root of the mean is about 6.3. This discrepancy is probably due to a slow drift in probe power at the cavity input, or in alignment of the cavity output into the detectors. Either way, this drift is taken into account by the data analysis program, which computes an average empty cavity transmission at least as often as once every 200 drops, for the purpose of setting atom-presence thresholds.

A technical issue worth mentioning here is a measured apparent delay between the two detectors, which needs to be taken into consideration in order to correctly set the

time axis on correlation functions. For a given incoming light pulse at the input of the fiber coupler leading to the single photon detectors A and B, the two corresponding channels of the P7888 pulse counting card will not record simultaneous time stamps. This offset is partly due to electronic delay in the cables leading from the detectors to the computer, and partly to a counting card offset between different channels. As shown in Fig. 3.8, the measured[5] overall apparent delay between detectors A and B is $\Delta_\tau = +10 \pm 1$ ns, with the A clicks coming in later than the B clicks. Our data analysis program computes correlations based on a histogram of the time separations between clicks in A versus B, which means that a feature occurring at $\tau = 0$ delay, in fact appears in our acquired data at $\tau = \Delta_\tau$. We compensate for this effect in our plots of correlation functions over small time scales, and for citing the value of $g^{(2)}(0)$ in Sec. 3.6.

For the purpose of extracting the value of $g_s^{(2)}(0)$ for the underlying signal coming from the atom-cavity system, in the manner outlined around Eqn. (3.33), we need to know the background counting rates due to the $3 \to 4'$ repumper and the detector dark counts. We measured[6] these total background rates to be $\gamma_A = 398 \pm 20$ cps for detector A, and $\gamma_B = 292 \pm 17$ cps for B, where the error bars assume Poissonian statistics. These numbers are used for computing the A_b and B_b rates per probing trial, which enter the background contribution to coincidences, from Eqn. (3.34).

3.4 Up-goer data as a motion detector for the atom

The spatial dependence of the AC-Stark shift caused by the FORT in our cavity is given by the Gaussian beam standing-wave profile:

$$U(z, \rho) = -2\pi\hbar U_0 \sin^2\left(\frac{2\pi z}{\lambda}\right) \exp\left(\frac{-2\rho^2}{w_0^2}\right) , \qquad (3.44)$$

where z and ρ are the axial and the radial dimension respectively, $\lambda = \lambda_{FORT} = 935.6$ nm and $w_0 = 24.8$ μm are the FORT wavelength and waist, as determined in

---

[5]Data taken on 3/24/05.
[6]Data taken on 3/25/05.

Secs. 4.1 and 4.2, and U_0 is the maximum trap depth in MHz, which in Sec. 4.5 is shown to be 40.9 MHz per mW of measured FORT cavity output power. The maximum trap depth is reached for z an odd multiple of $z_0 = \lambda/4$, and for $\rho = 0$.

Both the axial and the radial components of the trapping potential are anharmonic, with the spacing between the quantum levels, hence the vibrational frequencies, getting smaller as we ascend in energy. Since there are a finite number of levels, there is also a finite range that the vibrational frequencies are bounded by, with a largest frequency ν_0 at the bottom of the trap, and a smallest frequency $\nu_{\min}$ near the top.

For the axial direction, we can easily compute the upper bound frequency ν_0^{ax} by making the harmonic approximation for small-amplitude motion at the bottom of the trap, as follows:

$$\nu_0^{\mathrm{ax}} = \frac{1}{2\pi}\sqrt{\frac{1}{m}\frac{\partial^2 U(z,0)}{\partial z^2}}\bigg|_{z=z_0} = \sqrt{\frac{4\pi\hbar U_0}{m\lambda^2}}, \qquad (3.45)$$

where $m = 2.207 \times 10^{-25}$ kg is the mass of a Cesium atom. For typical parameters in our experiment, ν_0^{ax} is about 500 kHz.

Similarly, for the radial direction, the highest oscillation frequency ν_0^{rad} is given by:

$$\nu_0^{\mathrm{rad}} = \frac{1}{2\pi}\sqrt{\frac{1}{m}\frac{\partial^2 U(\lambda/4,\rho)}{\partial \rho^2}}\bigg|_{\rho=0} = \sqrt{\frac{2\hbar U_0}{m\pi w_0^2}}, \qquad (3.46)$$

which for us is typically about 5 kHz.

As mentioned before in Sec. 3.3, while the atom oscillates in the trap, so does the strength $|g|$ of its coupling to the cavity QED field. Axially, if the FORT and the probe mode are out of registration (see Fig. 2.6), then the modulation on $|g|$ that the atom experiences is predominantly at the same frequency as its oscillatory motion, as shown in Fig. 3.9 (a). Radially however, the two fields are always registered, since they are both radially symmetric, hence the atom will experience a particular value of $|g|$ twice in each period of oscillation, as shown in Fig. 3.9 (b). Thus the coupling strength modulation will occur at twice the frequency of the atom's radial motion.
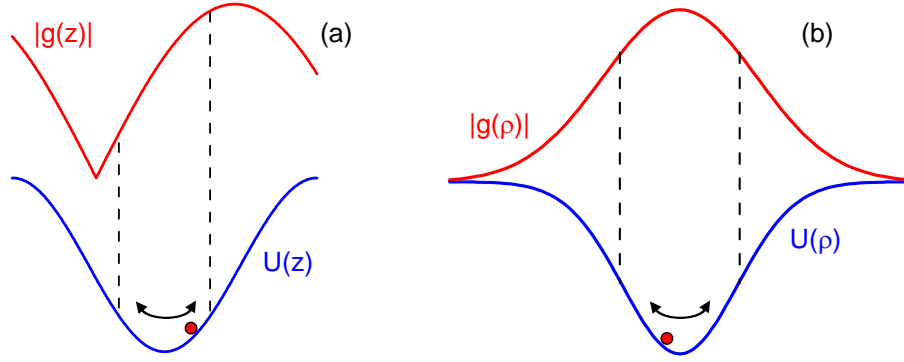
Figure 3.9: Modulation of the CQED coupling strength due to the (a) axial and (b) radial motion in the trapping potential.

As shown in Fig. 3.10, we were able to observe both these types of modulation[7] when driving the cavity with a dark-mode probe detuned $2\pi \times 34$ MHz to the red from the atomic resonance. The figure shows the Fourier transform of the click record corresponding to dark-mode probe pulses in the presence of an atom. The experiment is done as explained in Sec. 3.3; there is no cooling, the dark-mode pulses are 5 ms long each, the output FORT power is measured to be $P = 823\ \mu$W, the loading rate is about 65%, and the bright-mode transmission threshold for determining atom presence is set at 35% of the empty-cavity value. The dashed line in panel (a) indicates the predicted axial cutoff frequency $\nu_0^{\mathrm{ax}} \simeq 481$ kHz, obtained from Eqn. (3.45), which, as expected, bounds the peak on the right. For a smaller frequency resolution, we are also able to see the peak corresponding to the radial motion, as shown in panel (b). The dashed vertical line now denotes the predicted highest modulation frequency corresponding to radial motion, based on the known FORT parameters and Eqn. (3.46), namely $2\,\nu_0^{\mathrm{rad}} = 8.2$ kHz, where again the shown peak has a sharp edge on the high-frequency side, as expected.

Oscillation evidencing the trap frequencies can be seen in the time domain as well. Fig. 3.11 shows the raw coincidences, calculated based on Eqn. (3.30), corresponding to the data from Fig. 3.10. For panels (a) and (b) the bin size used for calculating $C(\tau)$ is $\delta = 40$ ns, whereas for panel (c) it is $\delta = 4$ ns. For the top panel only, the raw

---

[7]Measurement date: 1/18/05.
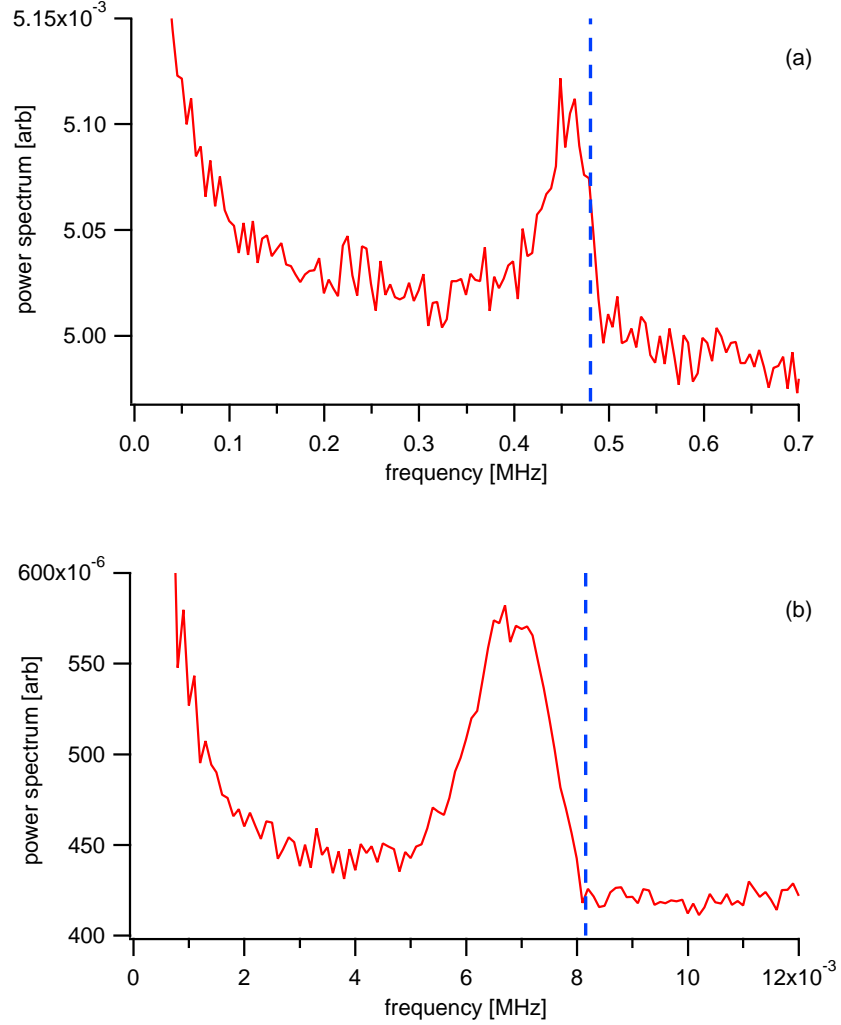
Figure 3.10: Fourier transform of the cavity transmission, showing modulation due to the (a) axial motion, near ν_0^{ax}; and (b) radial motion, near $2\,\nu_0^{\mathrm{rad}}$.

coincidences were multiplied by a $T_0/(T_0 - |\tau|)$ factor, with $T_0 = 5$ ms the probe pulse duration, in order to compensate for the finite-pulse triangle effect outlined around Eqn. (3.14). Clearly evident in the (a) panel is the slow oscillation corresponding to the radial peak in Fig. 3.10 (b). Zooming in on the central region of $C(\tau)$, we see in the middle panel the oscillations associated with the axial peak in Fig. 3.10 (a). Finally, on an even faster time scale, we notice the dip in coincidences near $\tau = 0$. This latter feature is known as photon anti-bunching, and can be shown (see Ref. [34], Sec. 14.7.3) to be a purely quantum effect.
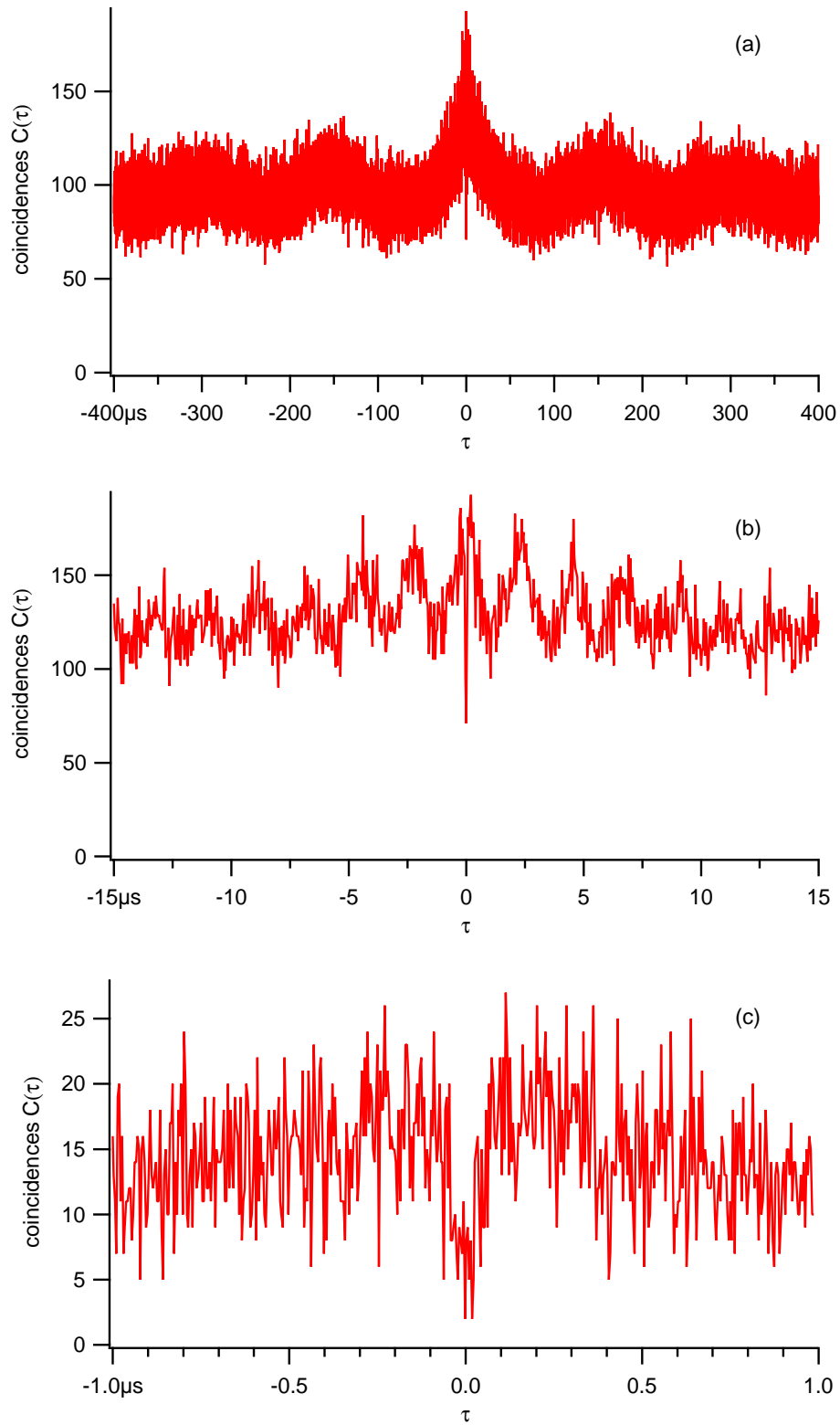
Figure 3.11: Un-normalized correlation function on three different time scales, showing (a) radial motion; (b) axial motion; (c) photon antibunching.
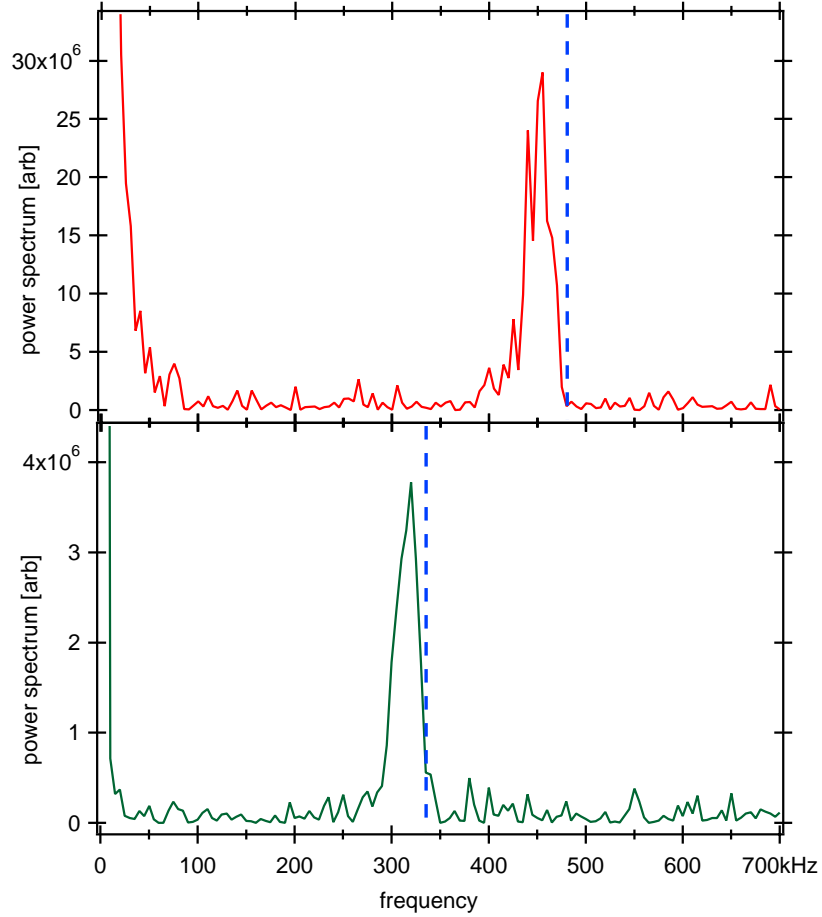
Figure 3.12: Fourier transform of the correlation function, showing a peak corresponding to axial motion for (a) full; (b) half FORT depth.

The observed non-classical character of the light is what Sec. 3.6 focuses on, so we will not dwell on this topic here. Rather, we will continue with our discussion of the motion-induced effects, as shown this time by the Fourier transform of the correlation function. Figs. 3.12 (a) and 3.13 (a) show the Fourier transform of the coincidences in Fig. 3.11, displaying the axial and the radial peaks. It is hard to understand quantitatively the exact shape of the correlation function Fourier transform, but by comparing with Fig. 3.10 we see that qualitatively it is very similar to the Fourier transform of the cavity transmission. For all the dark-mode up-goer data we have taken, it is in general true that the correlation function Fourier peak will tend to have better signal-to noise than its corresponding probe transmission peak, which is
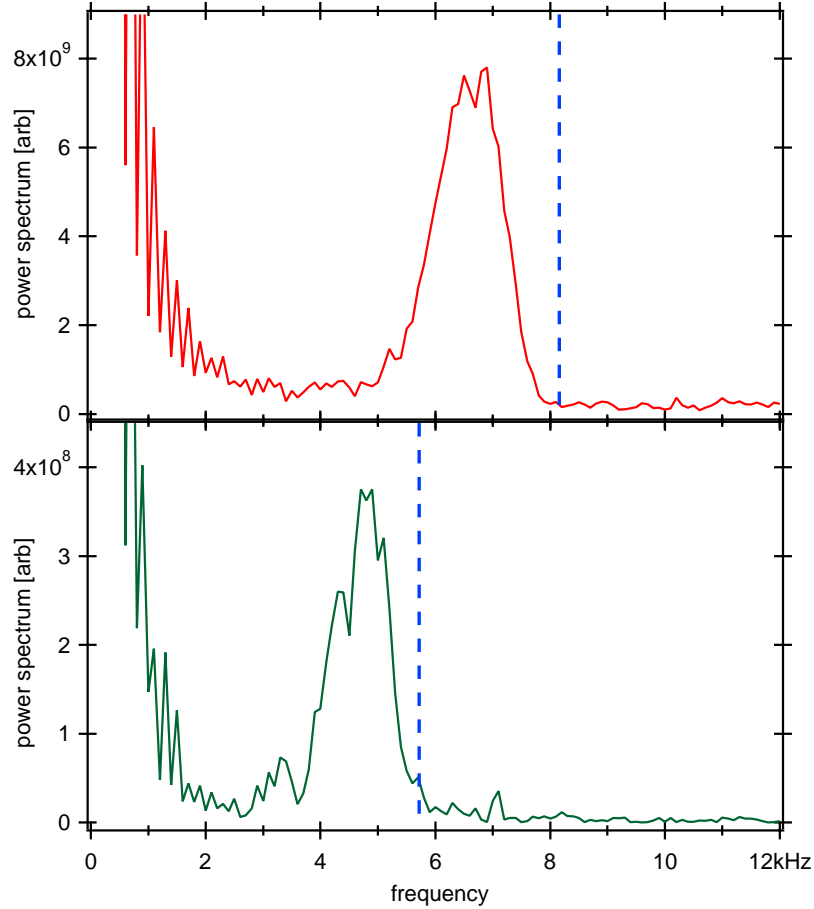
Figure 3.13: Fourier transform of the correlation function, showing a peak corresponding to radial motion for (a) full; (b) half FORT depth.

why we will usually prefer it to the click-record Fourier transform, for the purpose of making comparisons between different data sets.

In order to confirm the fact that the Fourier peaks in Figs. 3.12 (a) and 3.13 (a) do indeed correspond to motion-induced modulation on the cavity transmission, rather than some technical noise happening to be at just the right frequency, we decided to check that the peak location scales correctly with the trap depth. From Eqns. (3.45) and (3.46), we see that both the radial ν_0^{rad} and the axial ν_0^{ax} cutoff frequencies should scale like the square root of the FORT depth U_0. Thus if we were to reduce the FORT power from the original intensity corresponding to $P = 823\ \mu\mathrm{W}$ at the cavity output, to about half that, we would expect the motional peaks to move to the
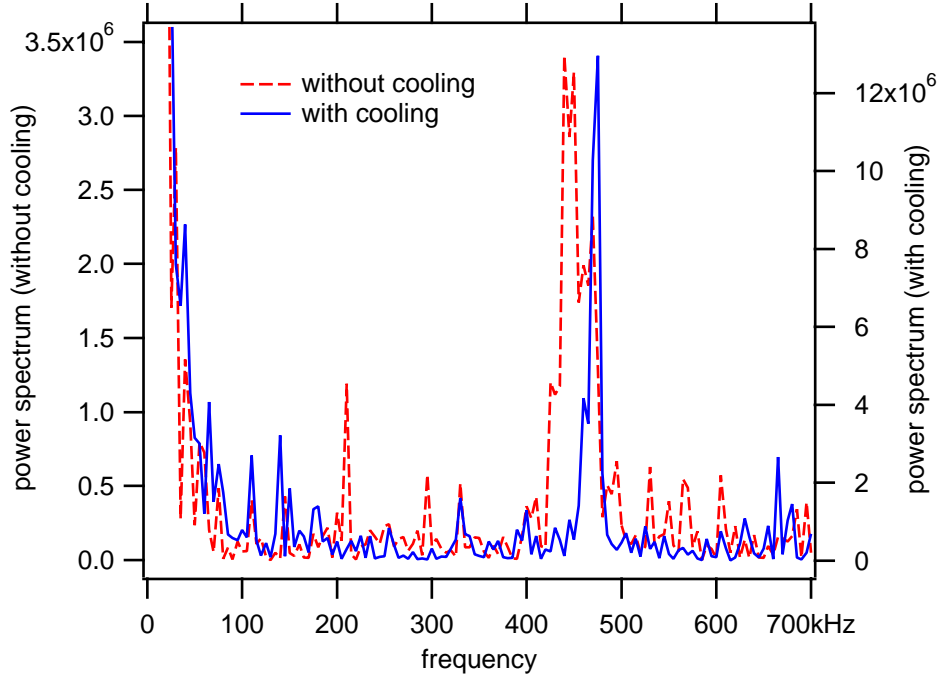
Figure 3.14: Fourier transform of the correlation function, showing the axial vibrational peak with and without cooling.

left, to frequencies reduced by approximately $\sqrt{2}$. Figs. 3.12 (b) and 3.13 (b) show the Fourier transform of the coincidence record obtained with such a reduced trap depth[8]. The experimental settings were all the same as in the (a) panels, except for the loading rate, which was 45%, and the measured FORT power at the cavity output, which in this case was $P = 405 \ \mu$W, leading to predicted axial and radial maximum frequencies of $\nu_0^{\mathrm{ax}} \simeq 337$ kHz and $2 \nu_0^{\mathrm{rad}} \simeq 5.7$ kHz. As before, these independently determined cutoff frequencies are indicated on the graphs by vertical dashed lines. The good agreement between the prediction and the data reassures us that we know how to correctly compute the trap depth, confirming that the observed peaks are indeed caused by atomic motion.

Our lab has already shown that tuning the Raman system to the red vibrational sideband achieves an increase in trap lifetime [6]. However, since the Raman beam also acts as a repumper for the radial cooling achieved by the $4 \rightarrow 4'$ lattice beams, one could argue that this increase is only due to extremely efficient radial cooling,

---

[8]Data taken on 1/19/05.

rather than to the radial and axial cooling working together. One way to settle this argument would be to somehow measure the axial temperature with and without Raman cooling. Since the Fourier peak shapes in the up-goer data depend on the energy distribution that the atom occupies within the potential well, one can in principle use them as a thermometer. Colder atoms will be closer to the bottom of the well, with little population in the higher-energy levels which correspond to lower vibrational frequencies. Thus the lower the atomic temperature, the narrower should the Fourier transform peak become, but without change in the cutoff frequency at the trap bottom.

We have some preliminary data which, based on the above argument, suggests that the effect of the Raman beam is indeed axial cooling. Fig. 3.14 shows the Fourier transform of coincidences obtained in two separate data sets. In the first[9], there is neither axial, nor radial cooling, and the dark-mode probe intervals are 5 ms long each, alternating with 100 μs long bright-mode probe pulses. In the second[10], the dark-mode probe is about twice as strong, but it is on in shorter intervals of 500 μs each. The bright-mode pulses are still 100 μs long, and the cooling pulses last 1.4 ms (see Fig. 3.6). Both data sets have loading rates of about 10%, and the same trap depth, hence the same maximal vibrational frequency, as is evident in Fig. 3.14. However, the widths of the two peaks are quite different: as expected, it seems that cooling makes the atomic population distribution narrower, and pushes it towards the bottom of the trap (i.e., towards the maximal vibrational frequency). The caveat is that, for the data set *with* cooling, it is possible that the stronger dark-mode probe might have kicked out of the trap those atoms which were hot before they got the chance to contribute significantly to the data, thus leading to the narrower distribution. Alternatively, the longer probe duration for the data *without* cooling would mean that there is also more heating, making the comparison unfair again. It ought to be easy to rule out both these scenarios in the near future, by taking cooling and no-cooling data with identical probe parameters.

---

[9]Measurement date: 1/19/05.
[10]Measurement date: 2/03/05.

3.5   C code for analyzing dark-mode data

The P7888 pulse counting card we use in our lab takes up to four inputs, and stores the pulse arrival times in a `specA*.lst` file, where the `*` denotes a four-digit integer. Each "stop" trigger is stored in this file as a 32-bit number, in the following format: the two most significant bits encode the input channel number, and the 30 least significant bits encode the time stamp, in units of the card's resolution. When the card is operating in single- or two-channel mode, its resolution is 1 ns, whereas when it is in three- or four-channel mode, the card resolution will be 2 ns. Recently, we have been operating the card in a three-channel mode, hence with a 2 ns resolution: one channel to acquire the pulses from each of the two APDs, and a third channel for acquiring the beginning of each dark-mode probe pulse. Every time it receives a "start" trigger, the P7888 resets its time stamp to zero; this happens once per experimental cycle, or "drop."

As a warm-up example, the following simple program called `all_clicks.c` takes a series of consecutive `specA*.lst` files and writes the time stamps corresponding to clicks from detectors A and B to two separate output files. The heart of the program is the `get_click()` function, written by David Boozer, which decomposes each data point acquired by the P7888 into a channel number and a time stamp expressed in ns. To compile the program, one can use for instance the JFE & GCC file editor and compiler combination [41], which upon pressing Ctrl+F9 will produce the executable `all_clicks.exe`. Here is the code for `all_clicks.c`, with comments in between the `\*` and `*/` signs. Whenever in doubt of what a pre-defined function does, please check the on-line manual pages, by typing `man <function_name>` at any ITS Unix prompt, or look it up in a textbook, such as the classic Ref. [42].

```
#include <stdio.h> /* library of input-output functions */

/* define constants */
#define A 0 /* card channel corresponding to detector A */
#define B 1 /* card channel for B */

/* global variables, shared by all functions */
FILE *input_file; /* current specA*.lst file */
```

```
FILE *outputA_file; /* time stamps for channel A */
FILE *outputB_file; /* time stamps from B */




/****************************************************************************
    get_click() function:
        turns next line in the input file into
            1) a channel number, from 0 to 3, and
            2) a time stamp in ns, assuming 2ns card resolution
        function arguments are pointers, so they can be written to
 ****************************************************************************/

void get_click (int *channel, unsigned long int *time) {

    char buffer[128]; /* stores a line from the input file */
    char *ptr;
    unsigned long int t; /* time stamp */
    int fields;

    ptr = fgets (buffer, 128, input_file);
    if (ptr != NULL) {
        fields = sscanf (buffer, "%lu\n", &t);
        if (fields != 1) {
            fprintf (stderr, "Error: format error in input file\n");
            exit (0);
        }
        /* efficient left << and right >> bit shift operators used below */
        *channel = (int) (t>>30); /* divide by 2^30 */
        /* t modulus 2^30, then multiply by card resolution, i.e. 2 ns */
        *time = (t % (1<<30)) << 1;
    }
    else { /* end of file reached, or error */
        *channel = -1;
        *time = 0;
    }
}



/****************************************************************************
    process_file() function:
        writes all time stamps in channel A to outputA.txt
        writes all time stamps in channel B to outputB.txt
 ****************************************************************************/

void process_file (char *filename) {

    unsigned long int t, t_old;
```

```c
    int channel;
    char buffer[128];

    input_file = fopen (filename, "r");
    if (input_file == NULL) {
        fprintf (stderr, "Error: cannot open file %s\n", filename);
        exit (0);
    }

    /* skip text at beginning of *.lst file */
    do fgets (buffer, 128, input_file); while (buffer[0] != '[');
    get_click (&channel, &t);

    while (channel != -1) {
        do { /* do-while loop processes one drop, i.e. one card trigger */

            if (channel == A) fprintf (outputA_file, "%lu\n", t);
            else if (channel == B) fprintf (outputB_file, "%lu\n",t);

            t_old = t; /* t_old is time when most recent click occurred */
            get_click (&channel, &t);

        /* 1e6 offset: rare glitches when card appears to go back in time */
        } while (t + 1e6 > t_old && channel != -1);
    }

    fclose (input_file);
}


/******************************************************************************
    main() function:
        syntax: all_clicks specA<num_start>.lst specA<num_end>.lst
        analyzes data in specA*.lst files with consecutive numbers
            between <num_start> and <num_end>
 ******************************************************************************/

int main (int argc, char *argv[]) {

    char filename[20];
    int spec_num, spec_num_start, spec_num_stop;

    if (argc != 3) {
        printf ("Error: wrong number of arguments");
        exit (0);
    }
```

```
    outputA_file = fopen ("outputA.txt", "w");
    if (outputA_file == NULL) {
        fprintf (stderr, "Error: cannot open outputA.txt file\n");
        exit (0);
    }

    outputB_file = fopen ("outputB.txt", "w");
    if (outputB_file == NULL) {
        fprintf (stderr, "Error: cannot open outputB.txt file\n");
        exit (0);
    }

    sscanf(argv[1],"specA%d.lst",&spec_num_start);
    sscanf(argv[2],"specA%d.lst",&spec_num_stop);
    spec_num = spec_num_start;

    while (spec_num <= spec_num_stop) { /* loop through all the files */
        sprintf(filename, "specA%d.lst\0",spec_num);
        printf ("processing file %s\n", filename);
        process_file(filename);
        spec_num++;
    }

    fclose (outputA_file);
    fclose (outputB_file);
}
```

The next C program, called `dark_mode.c`, is what we used for analyzing the dark-mode up-goer data in Sec. 3.6. Here is a broad outline of how the program works: for each `specA*.lst` file in the data set, based on a conservative estimate of which drops contain no atoms, the `transmission()` routine computes an average value for the empty-cavity transmission of the bright-mode probe. A threshold is then set as a fixed percentage of that value, which the `probes()` function uses to determine which of the trials do contain atoms. Once the code knows how to extract the trials with useful data, it uses them for incrementing various statistics for the entire data set, including the correlation function and its normalization, standard deviation, and background contribution.

I should also mention that this program is perhaps the ugliest quick and dirty C code I've ever written, its only redeeming virtue being that it seems to work. If one would wish to use it in the future, here is my advice: one should make the program

much more modular, with many functions each doing a small part, hence making it easy to leave out those which are not needed for a particular application. On a related note, those variables which are unnecessarily global should become local. Repeated code should be replaced by multiple calls to a simple function. Some of the constants, such as `DROPS` and `TRIALS`, should no longer be required from the user, since the program can extract them itself from the data. Finally, memory should be allocated dynamically, for instance for the `tA` and `tB` variables. Bearing the above words of caution in mind, here is the code:

```
#include <stdio.h>  /* declares input-output functions */
#include <math.h>       /* needed by e.g. the floor() function */

/* constants; customize according to the particular timing scheme,
    probe strength, background rates, etc. */
#define MIN_LIFE 0  /* minimum number of trials an atom must survive
                        to be counted in for G correlation function */
#define TRIALS 150  /* a trial is one bright probe turn-on; not counting
                        the first one, there are TRIALS trials per drop */
#define DROPS 200       /* number of loading attempts, i.e. of card
                        triggers per file */
#define PROBE_DURATION  5e5 /* dark-mode probe pulse duration in ns */
#define TRANS_THR 20 /* conservative (i.e., chosen rather high) threshold
                        for transmission() function */


#define GAMMA_A (397.9 * PROBE_DURATION * 1e-9) /* number of background
                        counts per trial in channel A */
#define GAMMA_B (291.8 * PROBE_DURATION * 1e-9) /* number of background
                        cts per trial in channel B */


#define ALPHA .35   /* percent of empty cavity bright probe transmission
                        below which a trial is considered successful, i.e.
                        an atom was present during previous dark trial  */


#define GTIME 1000000 /* tau axis range in ns, for correlation function */
#define BINSIZE 6   /* resolution for correlation function, aka delta */
#define GSIZE (GTIME/BINSIZE) /* bandwidth for correlation function, i.e.
                        size of the G array */


#define A 0             /* P7888 channel number for detector A */
#define B 1             /* P7888 channel number for detector B */
#define C 2             /* P7888 channel for time stamps at the beginning
                            of each dark-mode probe pulse */
```

```
#define MAXCLICKS 1000 /* size of tA and tB arrays in probes() function,
                i.e. max number of cts per dark trial per detector */


FILE *input_file; /* current specA*.lst file being analyzed */


int G[GSIZE]; /* array storing coincidences */
int counts[TRIALS+1][DROPS]; /* number of counts for each bright-mode probe
                               trial (0 to TRIALS) for a given a file */
int dcounts[TRIALS+1][DROPS]; /* number of counts for each dark-mode trial
                               (from 1 to TRIALS) in a file */


/* variables storing totals for all analyzed files */
float good_trials_total = 0; /* number of trials with atom present */
float good_counts_totalA = 0; /* clicks in channel A corresponding to
                                atom-present data */
float good_counts_totalB = 0; /* clicks in channel B corresponding to
                                good data, i.e. in the presence of an atom */
int num_loaded_total = 0; /* total number of atoms loaded */
int num_survived_total = 0; /* total number of atoms which survived the
                              entire observation interval */
float background_countsA = 0; /* counts from detector A in the absence of
                                any atoms */
float background_countsB = 0; /* background counts, i.e. with no atom
                                present, from detector B */
float background_trials = 0; /* number of trials which we know for sure
                               contain no atoms */


float click_prods_total = 0; /* sum of Ai Bi over all trials, used for
                               normalizing the correlation function */
float click_errs_total = 0; /* sum of Ai^2 Bi + Ai Bi^2, which is
                              sigma^2 of click_prods_total */



/***************************************************************************
    get_click() function:
        turns next line in the input file into
            1) a channel number, from 0 to 3, and
            2) a time stamp in ns, assuming 2ns card resolution
        function arguments are pointers, so they can be written to
 ***************************************************************************/

void get_click (int *channel, unsigned long int *time) {
  char buffer[128], *ptr;
  unsigned long int t;
  int fields;

  ptr = fgets (buffer, 128, input_file);
```

```
  if (ptr != NULL) {
    fields = sscanf (buffer, "%lu\n", &t);
    if (fields != 1) {
      fprintf (stderr, "Error: format error in input file\n");
      exit (0);
    }
    *channel = (int) (t>>30);
    *time = (t % (1<<30)) << 1;
  }
  else {
    *channel = -1;
    *time = 0;
  }
}


/****************************************************************************
    transmission() function:
      returns average bright probe empty cavity transmission for one file,
          which is useful for alignment-drift compensation
      loads up the counts[] and dcounts[] arrays, which contain the number
          of clicks for each bright and dark trial, respectively
      writes the number of clicks in each bright trial to the
          bright_histo.txt file, which can be inported to Igor for making
          a histogram; helpful for deciding the value of constant ALPHA
****************************************************************************/

double transmission (char *filename, double threshold) {

    unsigned long int t, t_C, t_old;
    int k, channel;
    int trial_num, drop_num;
    int num_noatoms, counts_probe;
    char buffer[128];
    FILE *bhisto_file;

    input_file = fopen (filename, "r");
    if (input_file == NULL) {
        fprintf (stderr, "Error: cannot open file %s\n", filename);
        exit (0);
    }

    bhisto_file = fopen ("bright_histo.txt", "a");
    if (bhisto_file == NULL) {
        fprintf (stderr, "Error: cannot open bright_histo.txt file\n");
        exit (0);
    }
```

```
/* skip text at beginning of *.lst file */
do fgets (buffer, 128, input_file); while (buffer[0] != '[');
get_click (&channel, &t);

num_noatoms = 0; /* number of drops with no atoms loaded, used for
                            averaging empty cavity transmission */
counts_probe = 0; /* bright-mode counts when no atom was loaded,
                       used for averaging empty cavity transmission */
drop_num = 0; /* current loading attempt */

while (channel != -1) {

    if (drop_num >= DROPS) {
        printf ("error: more drops than DROPS\n");
        exit(0);
    }

    for (k = 0; k <= TRIALS; k++) { /* initializations for next drop */
        counts[k][drop_num] = 0;
        dcounts[k][drop_num] = 0;
    }
    trial_num = 0; /* current trial */
    t_C = t; /* time when most recent click occurred in channel C */

    do { /* do-while loop processes one drop */
        if (channel == C) {
                    trial_num++;
                    t_C = t;
        }
        else /* count bright and dark probe clicks for each trial */
            if (trial_num > 0 && trial_num <= TRIALS) {
                if (t > t_C + PROBE_DURATION &&
                        t <= t_C + PROBE_DURATION + 1e5)
                    /* bright probe pulses last 100 us = 1e5 ns */
                    counts[trial_num][drop_num]++;
                else if (t > t_C && t <= t_C + PROBE_DURATION)
                    dcounts[trial_num][drop_num]++;
            }
            else /* trial 0: "did we load?" bright pulse only */
                if (trial_num == 0 && t <= 1e5) counts[0][drop_num]++;

        t_old = t; /* t_old is time when most recent click occurred */
        get_click (&channel, &t);

    } while (t + 1e6 > t_old && channel != -1);
```

```c
        if (trial_num == TRIALS) { /* done with this drop */
            if (counts[0][drop_num] > threshold) {
                num_noatoms++;
                for (k = 0; k <= TRIALS; k++)
                    counts_probe += counts[k][drop_num];
            }
            for (k = 0; k <= TRIALS; k++)
                fprintf (bhisto_file, "%d\n", counts[k][drop_num]);
            drop_num++;
        }
        else fprintf (stderr, "glitch after trial %d\n", trial_num);
    }

    fclose (input_file);
    fclose (bhisto_file);
    return ((double) counts_probe/((TRIALS+1.0)*num_noatoms));
}


/****************************************************************************
    probes() function:
        loads into the G[] array the histogram  of time separations
        writes all time stamps corresponding to an atom being present
            to the fft.txt file, which can be loaded into Matlab for
            computing the Fourier transform of the probe transmission
        writes the cavity transmission for each dark-mode trial when an
            atom was present to the dark_histo.txt file, which can be used
            by Igor to make a histogram of dark probe transmission
        writes the trial number, for each drop when an atom was loaded,
            into the file atom_left.txt, which can be loaded into Igor to
            make a histogram and infer a lifetime
        measures loading & survival probability
        measures background rates, i.e. click rate in the absence of
            an atom, as derived from the data (not to be confused with
            separately measured rates GAMMA_A and GAMMA_B)
****************************************************************************/

void probes(char *filename, double threshold) {

    unsigned long int t, t_C, t_old;
    int channel, i, j, k, m, n;
    int trial_num, drop_num;
    char buffer[128];
    int clicksA = 0, clicksB = 0; /* how full the tA and tB arrays are */
    int num_loaded, num_survived;
    unsigned long int tA[MAXCLICKS], tB[MAXCLICKS];
    int atom_left[DROPS]; /* for each loading attempt, stores the first
```

```c
                                         trial number without an atom */
int noatom[DROPS]; /* TRUE if no atom was loaded in that attempt,
                                         FALSE otherwise */
FILE *fft_file, *dhisto_file, *atomleft_file;

input_file = fopen (filename, "r");
if (input_file == NULL) {
    fprintf (stderr, "Error: cannot open file %s\n", filename);
    exit (0);
}

fft_file = fopen ("fft.txt", "a");
if (fft_file == NULL) {
    fprintf (stderr, "Error: cannot open fft.txt file\n");
    exit (0);
}

dhisto_file = fopen ("dark_histo.txt", "a");
if (dhisto_file == NULL) {
    fprintf (stderr, "Error: cannot open dark_histo.txt file\n");
    exit (0);
}

atomleft_file = fopen ("atom_left.txt", "a");
if (atomleft_file == NULL) {
    fprintf (stderr, "Error: cannot open atom_left.txt file\n");
    exit (0);
}

for (k = 0; k < DROPS; k++) {

    j = 0;
    while (j <= TRIALS && counts[j][k] < threshold) {
        if (j > 0) fprintf (dhisto_file, "%d\n", dcounts[j][k]);
        j++;
    }
    atom_left[k] = j; /* present during trial j-1, gone during j */
    if (j>0) fprintf (atomleft_file, "%d\n", j);
    if (j > MIN_LIFE)  good_trials_total += (float) j-1;

    j=0;
    while (j <= TRIALS && counts[j][k] > threshold) j++;
    if (j == TRIALS+1) { /* no atom was loaded */
        background_trials += (float) TRIALS;
        noatom[k] = 1; /* this is a flag: no atom in this drop */
    }
    else noatom[k] = 0;
```

```
}

do fgets (buffer, 128, input_file); while (buffer[0] != '[');
get_click (&channel, &t);

num_loaded = 0;
num_survived = 0;
drop_num = 0;

while (channel != -1) {

    trial_num = 0;
    t_C = t;

    do { /* do-while processes one drop */
        if (channel == C) { /* new dark trial coming up next */
            t_C = t;
            trial_num++;

            /* now process data accumulated during previous trial */
            click_prods_total += (float) clicksA*clicksB;
            click_errs_total +=
                (float) clicksA*clicksB*(clicksA+clicksB);
            good_counts_totalA += (float) clicksA;
            good_counts_totalB += (float) clicksB;
            for (i = 0; i < clicksA; i++) {
                /* does nothing if e.g. clicksA=0 */
                for (j = 0; j < clicksB; j++) {
                    /* update histogram of time separations */
                    m = (int) tA[i] - tB[j] + GTIME/2;
                    n = (int) floor ((double) m/BINSIZE);
                    if (n >= 0 && n < GSIZE) G[n]++;
                }
            }
            clicksA = 0;    /* counts clicks in channel A for current
                                    dark trial */
            clicksB = 0;    /* counts clicks from B for current
                                    dark-mode probe trial */
        }

        else  if (t > t_C && t <= t_C + PROBE_DURATION &&
                trial_num > 0) {
            if (trial_num < atom_left[drop_num] &&
                    atom_left[drop_num] > MIN_LIFE) {
                if (channel == A && clicksA < MAXCLICKS)
                    tA[clicksA++] = t;
                else if (channel == B && clicksB < MAXCLICKS)
```

```
                        tB[clicksB++] = t;
                    fprintf(fft_file, "%lu\n", t);
                }
                else if (noatom[drop_num]) {
                    if (channel == A) background_countsA += 1.0;
                    else if (channel == B) background_countsB += 1.0;
                }
            }
            t_old = t;
            get_click (&channel, &t);

        } while (t + 1e6 > t_old && channel != -1);

        if (trial_num == TRIALS) {   /* done with this drop */
            if (counts[0][drop_num] < threshold) {
                num_loaded++;
                if (atom_left[drop_num] == TRIALS+1) num_survived++;
            }
            drop_num++;
        }
        else fprintf (stderr, "glitch after trial %d\n", trial_num);
    }

    num_loaded_total += num_loaded;
    num_survived_total += num_survived;
    printf ("%d loaded, %d survived\n", num_loaded, num_survived);
    fclose (input_file);
    fclose (fft_file);
    fclose (dhisto_file);
    fclose (atomleft_file);
}


/****************************************************************************
    main() function:
        syntax: dark_mode specA<num_start>.lst specA<num_end>.lst
        analyzes data in specA*.lst files with consecutive numbers
            between <num_start> and <num_end>
        writes data statistics both to the standard output, and to the file
            output_stats.txt
        writes the unnormalized correlation function to file corr.txt
        writes the normalized correlation function, with no background
            contribution taken into account, to file g2_1.txt
        writes normalized correlation function, with background contribution
            subtracted, to file g2_2.txt
****************************************************************************/
```

```c
int main (int argc, char *argv[]) {

    double trans;
    char filename[20];
    int k, spec_num, spec_num_start, spec_num_stop;
    double gammaA, gammaB, RA, RB, g2_background, g2_norm, T;
    FILE *corr_file, *g2_file1, *g2_file2, *out_file;
    double background_prods;

    if (argc != 3) {
        printf ("Error: wrong number of arguments");
        exit (0);
    }

    out_file = fopen ("output_stats.txt", "w"); /* various statistics,
                      compiled for the entire data set */
    if (out_file == NULL) {
        printf ("Error: cannot open output_stats.txt file.\n");
        exit (0);
    }

    corr_file = fopen ("corr.txt", "w"); /* unnormalized coincidences */
    if (corr_file == NULL) {
        printf ("Error: cannot open corr.txt file.\n");
        exit (0);
    }

    g2_file1 = fopen("g2_1.txt", "w"); /* no background subtraction */
    if (g2_file1 == NULL) {
        printf ("Error: cannot open g2_1.txt file.\n");
        exit (0);
    }

    g2_file2 = fopen("g2_2.txt", "w"); /* background subtracted */
    if (g2_file2 == NULL) {
        printf ("Error: cannot open g2_2.txt file.\n");
        exit (0);
    }

    sscanf(argv[1],"specA%d.lst",&spec_num_start);
    sscanf(argv[2],"specA%d.lst",&spec_num_stop);
    spec_num = spec_num_start;

    for (k = 0; k < GSIZE; k++) G[k] = 0;

    while (spec_num <= spec_num_stop) {
```

```
        sprintf(filename, "specA%d.lst\0",spec_num);
        printf ("processing file %s\n", filename);
        trans = transmission(filename, TRANS_THR);
        printf ("bright transmission %4.2f clicks per 100us\n", trans);
        probes (filename, ALPHA * trans);
        spec_num++;
}


fprintf (out_file, "\n\n%d total loaded, %d total survived out of "
    "%d drops\n", num_loaded_total, num_survived_total,
    (spec_num_stop-spec_num_start+1)*DROPS);
printf ("\n\n%d total loaded, %d total survived out of %d drops\n",
    num_loaded_total, num_survived_total,
    (spec_num_stop-spec_num_start+1)*DROPS);


fprintf (out_file, "%4.3f trials average lifetime\n",
    (double) good_trials_total/num_loaded_total);
printf ("%4.3f trials ave lifetime\n",
    (double) good_trials_total/num_loaded_total);


fprintf(out_file, "%4.2f good trials, %4.2f good counts A, "
    "%4.2f good counts B\n",
    good_trials_total, good_counts_totalA, good_counts_totalB);
printf("%4.2f good trials, %4.2f good counts A, %4.2f good counts B\n",
    good_trials_total, good_counts_totalA, good_counts_totalB);


fprintf (out_file, "%4.3f A cts per trial, %4.3f B cts per trial\n",
    (double) good_counts_totalA/good_trials_total,
    (double) good_counts_totalB/good_trials_total);
printf ("%4.3f A cts per trial, %4.3f B cts per trial\n",
    (double) good_counts_totalA/good_trials_total,
    (double) good_counts_totalB/good_trials_total);


fprintf (out_file, "no atom data A: %4.3f cts/trial, B: "
    "%4.3fcts/trial\n", (double) background_countsA/background_trials,
    (double) background_countsB/background_trials);
printf ("no atom data A: %4.3f cts/trial, B: %4.3fcts/trial\n",
    (double) background_countsA/background_trials,
    (double) background_countsB/background_trials);


T = good_trials_total * PROBE_DURATION * 1.0e-9;
fprintf (out_file, "total data time:\n\t%4.2fs\n", T);
printf ("total data time:\n\t%4.2fs\n", T);


gammaA = (double) background_countsA/
    (background_trials*PROBE_DURATION*1.0e-9);
gammaB = (double) background_countsB/
```

```
    (background_trials*PROBE_DURATION*1.0e-9);
fprintf (out_file,"average rate when no atom is present:\n"
    "\t%4.2fcps in A, %4.2fcps in B\n", gammaA, gammaB);
printf ("average rate when no atom is present:\n"
    "\t%4.2fcps in A, %4.2fcps in B\n", gammaA, gammaB);


RA = (double) good_counts_totalA/T - gammaA;
RB = (double) good_counts_totalB/T - gammaB;
fprintf (out_file, "average signal rate (detected, minus average"
    " background):\n\t%4.2fcps in A, %4.2fcps in B\n", RA, RB);
printf ("average signal rate (detected, minus average background):\n"
    "\t%4.2fcps in A, %4.2fcps in B\n", RA, RB);


g2_background = (RA*gammaB + RB*gammaA + gammaA*gammaB)/(RA*RB);
g2_norm = RA*RB*T*BINSIZE*1.0e-9;
fprintf(out_file, "based on averaged rates:\n\tg2_norm = %4.2f, "
    "g2_bkgnd = %4.2f\n", g2_norm, g2_background);
printf("based on averaged rates:\n\tg2_norm = %4.2f, g2_bkgnd=%4.2f\n",
    g2_norm, g2_background);


fprintf (out_file, "%4.4f old-school normalization factor\n",
    (double) good_counts_totalA * good_counts_totalB * BINSIZE/
    (good_trials_total * PROBE_DURATION));
printf ("%4.4f old school normalization factor\n",
    (double) good_counts_totalA * good_counts_totalB * BINSIZE/
    (good_trials_total * PROBE_DURATION));


fprintf (out_file, "Ai*Bi sum, aka click_prods_total:\n\t%4.2f\n",
    (float) click_prods_total);
printf ("Ai*Bi sum, aka click_prods_total:\n\t%4.2f\n",
    (float) click_prods_total);


fprintf (out_file, "Ai*Bi*(Ai+Bi) sum, aka click_errs_total:\n"
    "\t%4.2f\n", (float) click_errs_total);
printf ("Ai*Bi*(Ai+Bi) sum, aka click_errs_total:\n\t%4.2f\n",
    (float) click_errs_total);


background_prods = GAMMA_A*good_counts_totalB +
    GAMMA_B*good_counts_totalA - GAMMA_A*GAMMA_B*good_trials_total;
fprintf (out_file, "backgrnd products: %4.2f, click products: %4.2f\n",
    background_prods, click_prods_total);
printf ("backgrnd products: %4.2f, click products: %4.2f\n",
    background_prods, click_prods_total);


for (k = 0; k < GSIZE; k++) {
    fprintf (corr_file, "%d\n", G[k]);
    fprintf (g2_file1, "%4.4f\n",
```

```
        (double) G[k]*PROBE_DURATION/(click_prods_total*BINSIZE));
    fprintf (g2_file2, "%4.4f\n", (double) (G[k]*PROBE_DURATION/BINSIZE
        - background_prods)/(click_prods_total-background_prods));
}


fclose (corr_file);
fclose (g2_file1);
fclose (g2_file2);
fclose (out_file);
}
```

3.6 Photon blockade in an optical cavity with one trapped atom

This section is reproduced almost verbatim from Ref. [8].

Sufficiently small metallic [43] and semiconductor [44] devices at low temperatures exhibit "Coulomb blockade," whereby charge transport through the device occurs on an electron-by-electron basis. For example, a single electron on a metallic island of capacitance C can block the flow of another electron if the charging energy $e^2/2C \gg k_B T$ and the tunneling resistance $R \gg h/4e^2$. In 1997, Imamoḡlu et $al.$ proposed that an analogous effect might be possible for photon transport through an optical system by employing photon-photon interactions in a nonlinear optical cavity [45]. In this scheme, strong dispersive interactions enabled by electromagnetically induced transparency (EIT) cause the presence of a "first" photon within the cavity to block the transmission of a "second" photon, leading to an ordered flow of photons in the transmitted field.

After resolution of an initial difficulty [46], subsequent work has confirmed that such photon blockade is indeed feasible for a single intracavity atom by way of a multi-state EIT scheme [47, 48, 49]. Photon blockade is possible in other settings, including in concert with Coulomb blockade [50] and via tunneling with localized surface plasmons [51]. Photon blockade has also been predicted for a two-state atom coupled to a cavity mode [52, 36, 53].

As illustrated in Fig. 3.15, the underlying mechanism is the anharmonicity of the

Jaynes-Cummings ladder of eigenstates [13, 54]. Panel (a) shows the level diagram corresponding to the lowest energy states for a two-state atom of transition frequency ω_A coupled (with single-photon Rabi frequency g_0) to a mode of the electromagnetic field of frequency ω_C, with $\omega_A = \omega_C \equiv \omega_0$ [13]. Resonant absorption of a photon of frequency $\omega_- = \omega_0 - g_0$ (arrow) to reach the state $|1, -\rangle$ (where $|n, +(-)\rangle$ denotes the higher (lower) energy eigenstate with n excitations) "blocks" the absorption of a second photon at ω_- because transitions to $|2, \pm\rangle$ are detuned from resonance. Thus two-photon absorption is suppressed for the probe field, leading to $g^{(2)}(0) < 1$ [53].

Scattering from a single atom in free space also provides a fundamental example of photon blockade [55], albeit with the fluorescent field distributed over 4π and the flux limited by the rate of spontaneous decay γ. By contrast, cavity-based schemes offer the possibility for photon emission into a collimated spatial mode with high efficiency and at a rate set by the cavity decay rate κ, which can be much larger than γ. Achieving photon blockade for a single atom in a cavity requires operating in the regime of strong coupling, for which the frequency scale g_0 associated with reversible evolution of the atom-cavity system exceeds the dissipative rates (γ, κ) [16].

In this section, we report observations of photon blockade in the light transmitted by an optical cavity containing one atom strongly coupled to the cavity field. For coherent excitation at the cavity input, the photon statistics for the cavity output are investigated by measurement of the intensity correlation function $g^{(2)}(\tau)$, which demonstrates the manifestly nonclassical character of the transmitted field. Explicitly, we find $g^{(2)}(0) = (0.13 \pm 0.11) < 1$ with $g^{(2)}(0) < g^{(2)}(\tau)$, so that the output light is both sub-Poissonian and anti-bunched [34]. We find that $g^{(2)}(\tau)$ rises to unity at a time $\tau = \tau_B \simeq 45$ns, which is consistent with the lifetime $\tau_- = 2/(\gamma + \kappa) = 48$ ns for the state $|1, -\rangle$ associated with the blockade. Over longer time scales, cavity transmission exhibits modulation arising from the oscillatory motion of the atom trapped within the cavity mode. We utilize this modulation to make an estimate of the energy distribution for the atomic center-of-mass motion and infer a maximum energy $E/k_B \sim 250$ μK.

The schematic of our experiment in Fig. 3.15(c) illustrates the Fabry-Perot cavity
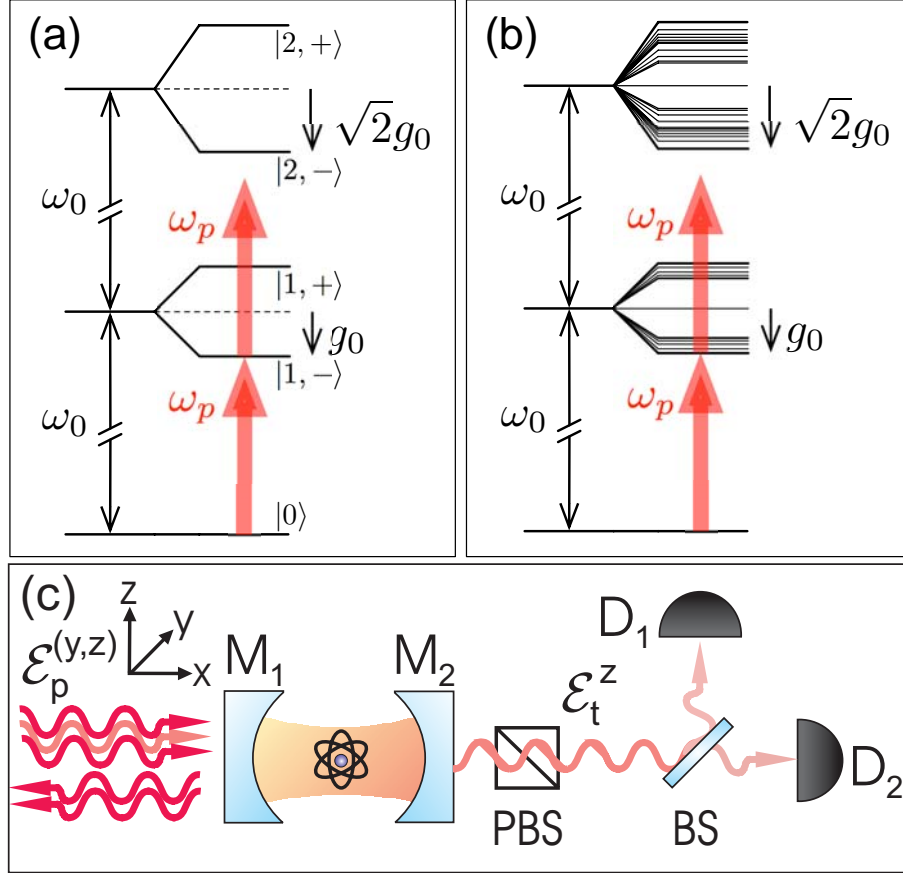
Figure 3.15: Level diagram for (a) a two-state atom and (b) the $4 \to 5'$ transition in Cesium, coupled to a single cavity mode; (c) simple schematic of the experiment.

formed by mirrors (M_1, M_2) into which single optically cooled Cesium atoms are loaded. The physical length of the cavity is 42.2 μm and the finesse is 4.3×10^5. The cavity length is independently stabilized such that a TEM_{00} longitudinal mode at λ_{C_1} is resonant with the free-space atomic transition at λ_A and another TEM_{00} mode at λ_{C_2} is resonant at λ_F. At the cavity center $x = 0$, the mode waists $w_{C_{1,2}} = \{23.4, 24.5\}$ μm at $\lambda_{C_{1,2}} = \{852.4, 935.6\}$ nm. Atoms are trapped within the cavity by a far-off-resonance trap (FORT) which is created by exciting a TEM_{00} cavity mode at $\lambda_F = 935.6$ nm [2]. To achieve strong coupling, we utilize the $6S_{1/2}, F = 4 \to 6P_{3/2}, F' = 5'$ transition of the D2 line in Cesium at $\lambda_A = 852.4$ nm, for which the maximum rate of coherent coupling is $g_0/2\pi = 34$ MHz for $(F = 4, m_F = \pm 4) \to (F' = 5', m'_F = \pm 5)$. The transverse decay rate for the $6P_{3/2}$ atomic states is

$\gamma/2\pi = 2.6$ MHz while the cavity field decays at rate $\kappa/2\pi = 4.1$ MHz.

A variety of factors make our atom-cavity system more complex than the simple situation described by the Jaynes-Cummings eigenstates, including most significantly that (1) the cavity supports two modes $l_{y,z}$ with orthogonal linear polarizations $(\hat{y}, \hat{z})$ near $\lambda_A = 852.4$ nm and (2) a multiplicity of Zeeman states are individually coupled to these modes for transitions between the manifolds $(F = 4, m_F) \leftrightarrow (F' = 5', m'_F)$. An indication of the potential for this system to achieve photon blockade is provided in Fig. 3.15 (b), which displays the actual eigenvalue structure for the first two excited manifolds obtained by direct diagonalization of the interaction Hamiltonian. As for the basic two-state system, excitation to the lowest energy state in the one-excitation manifold "blocks" subsequent excitation because the transitions to the two-excitation manifold are out of resonance.

To substantiate this picture quantitatively, we present in Fig. 3.16 theoretical results from the steady-state solution to the master equation in various situations. All calculations shown are for the case of coincident atomic and cavity resonances $\omega_A = \omega_{C_1} \equiv \omega_0$ for parameters $(g_0, \kappa, \gamma)/2\pi = (33.9, 4.1, 2.6)$ MHz, and the probe strength is such that the intracavity photon number on resonance without an atom is 0.05. The blue dotted lines indicate Poissonian statistics. Beginning with the ideal setting of a two-state atom coupled to a single cavity mode, we display in Fig. 3.16 (a) results for the probe transmission spectrum $T(\omega_p)$ and the intensity correlation function $g^{(2)}(0)$ of the field $\mathcal{E}_t$ transmitted by mirror M_2 for excitation by a coherent-state probe $\mathcal{E}_p$ of variable frequency ω_p incident upon the cavity mirror M_1. $T(\omega_p)$ is proportional to the ratio of photon flux $\langle \mathcal{E}_t^\dagger \mathcal{E}_t \rangle$ transmitted by M_2 to the flux $|\mathcal{E}_p|^2$ incident upon M_1, and normalized such that a cavity without an atom has a resonant transmission of unity, i.e., $T(\omega_p = \omega_{C_1}) = 1$. For a field with intensity operator $\hat{I}(t)$, $g^{(2)}(\tau) \equiv \langle : \hat{I}(t)\hat{I}(t + \tau) : \rangle / \langle : \hat{I}(t) : \rangle \langle : \hat{I}(t + \tau) : \rangle$, where the colons denote time and normal ordering [34].

Clearly evident in $T(\omega_p)$ are two peaks at $\omega_p = \omega_\pm \equiv \omega_0 \pm g_0$ associated with the vacuum-Rabi splitting for the states $|1, \pm\rangle$. At these peaks, $\mathcal{E}_p$ is detuned for excitation $|1, \pm\rangle \rightarrow |2, \pm\rangle$, resulting in $g^{(2)}(0) < 1$ for $\mathcal{E}_t$. The Poissonian photon
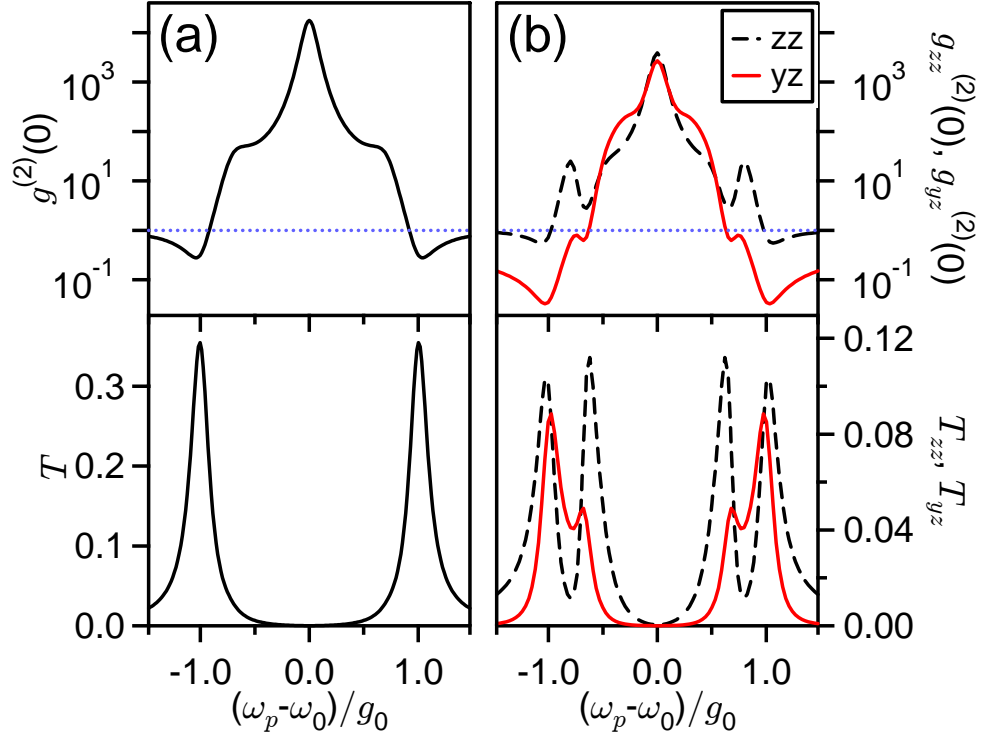
Figure 3.16: Theoretical results for the transmission spectrum and intensity correlation functions: (a) $T(\omega_p)$, $g^{(2)}(0)$; (b) $T_{zz}(\omega_p)$, $g_{zz}^{(2)}(0)$ (dashed) and $T_{yz}(\omega_p)$, $g_{yz}^{(2)}(0)$.

statistics of the incident probe are thereby converted to sub-Poissonian statistics for the transmitted field by way of the photon blockade effect illustrated in Fig. 3.15 (a). For strong coupling in the weak-field limit, $g^{(2)}(0) \propto (\kappa + \gamma)^2/g_0^2$ for $\omega_p = \omega_\pm$ [36], hence the premium on achieving $g_0 \gg (\kappa, \gamma)$. By contrast, for $\omega_p = \omega_0 \pm g_0/\sqrt{2}$, $\mathcal{E}_p$ is resonant with the two-photon transition $|0\rangle \rightarrow |2, \pm\rangle$, resulting in super-Poissonian statistics with $g^{(2)}(0) \gg 1$. For $\omega_p = \omega_0$, there is extremely large bunching due to quantum interference between $\mathcal{E}_p$ and the atomic polarization [36, 35].

In Fig. 3.16 (b) we examine the more complex situation relevant to our actual experiment, namely a multi-state atom coupled to two cavity modes with orthogonal polarizations $\hat{y}, \hat{z}$. Most directly related to the simple case of Fig. 3.16 (a) is to excite one polarization eigenmode with the incident probe, taken here to be $\mathcal{E}_p^z$, and to detect the transmitted field $\mathcal{E}_t^z$ for this same polarization, with the transmission spectrum and intensity correlation function denoted by $T_{zz}(\omega_p)$, $g_{zz}^{(2)}(0)$, respectively. Included

in the model are all transitions $(F = 4, m_F) \leftrightarrow (F' = 5', m'_F)$ with their respective coupling coefficients $g_0^{(m_F, m'_F)}$, as well as the two cavity modes $l_{y,z}$ here assumed to be degenerate in frequency. Even for this full multiplicity of states, $T_{zz}(\omega_p)$ displays a rather simple structure, now with a multiplet structure in place of the single vacuum-Rabi peak around $\omega_p \simeq \omega_0 \pm g_0$. For a probe frequency tuned to the eigenvalues $\omega_p = \omega_0 \pm g_0$, $g_{zz}^{(2)}(0) \simeq 0.7$, once again dropping below unity as in Fig. 3.16 (a).

An alternate scheme is to detect along $\hat{z}$, but excite along orthogonal polarization $\hat{y}$, with the respective transmission and correlation functions $T_{yz}(\omega_p)$, $g_{yz}^{(2)}(0)$ also shown in Fig. 3.16 (b). Similar to $T_{zz}(\omega_p)$, $T_{yz}(\omega_p)$ exhibits a multiplet structure in the vicinity of $\omega_p \simeq \omega_0 \pm g_0$ due to the nature of the first excited states of the atom-cavity system. At the extremal $\omega_p = \omega_0 \pm g_0$, $g_{yz}^{(2)}(0)$ reaches a value $g_{yz}^{(2)}(0) = 0.03$ much smaller than for either $g^{(2)}(0)$ in (a) or $g_{zz}^{(2)}(0)$ in (b) for the same values of (g_0, κ, γ). Our preliminary hypothesis is that this reduction relates to the absence of the superposed driving field $\mathcal{E}_p^y$ for the transmitted field $\mathcal{E}_t^z$ with orthogonal polarization $\hat{z}$ [56]; photons in the mode l_z derive only from emissions associated with the atomic components of atom-field eigenstates.

Tuning the probe to $\omega_p = \omega_0 \pm g_0$ has the additional benefit of reducing sensitivity to atomic position, which varies experimentally due to atomic motion and the multiplicity of trapping sites within the cavity [7]. The atomic position affects the transmission via the position dependence of the coupling $g = g_0 \psi(\vec{r})$, where ψ is the TEM_{00} spatial mode at λ_{C_1} with maximum $|\psi| = 1$ and $\vec{r}$ is the position of the atom. Since $T_{yz}(\omega_p)$ is small when $|\omega_p - \omega_0| \gtrsim g$, atoms which have a lower than expected value of g will have a reduced contribution to the photon statistics.

An important step in the implementation of this strategy is our recent measurement of the vacuum-Rabi spectrum $T_{zz}(\omega_p)$ for one trapped atom [7]. In that work we obtained quantitative agreement on an atom-by-atom basis between our observations and an extension of the theoretical model employed to generate the various plots in Fig. 3.16 (b). The extended model incorporates ac-Stark shifts from the FORT as well as cavity birefringence.

The TEM_{00} longitudinal mode for the FORT is driven by a linearly polarized

input field $\mathcal{E}_{FORT}$, resulting in nearly equal ac-Stark shifts for Zeeman states in the $6S_{1/2}, F = 3, 4$ manifold. At an antinode of the field, the peak value of the trapping potential for these states is $U_0/h = -43$ MHz for all our measurements. Zeeman states of the $6P_{3/2}, F' = 5'$ manifold experience a similar trapping potential, but with a weak dependence on m'_F [2]. Stress-induced birefringence in the cavity mirrors leads to a mode splitting $\Delta\omega_{C_1}/2\pi = 4.4 \pm 0.2$ MHz of the two cavity modes $l_{y,z}$ with orthogonal linear polarizations $(\hat{y}, \hat{z})$. $\mathcal{E}_{FORT}$ is linearly polarized and aligned along $\hat{z}$, the higher frequency mode. The extended model predicts that corrections to $g_{yz}^{(2)}(0)$ due to these effects are small for our parameters.

With these capabilities in hand, we now report measurements[11] of $g_{yz}^{(2)}(\tau)$ for the light transmitted by a cavity containing a single trapped atom. We tune the probe $\mathcal{E}_p^y$ to $(\omega_p - \omega_0)/2\pi = -34$ MHz, near $-g_0$, and acquire photoelectric counting statistics of the field $\mathcal{E}_t^z$ by way of two avalanche photodiodes (D_1, D_2), as illustrated in Fig. 3.15(c). From the record of these counts, we are able to determine $g_{yz}^{(2)}(\tau)$ by way of the procedures discussed in Ref. [5]. The efficiency for photon escape from the cavity is $\alpha_{e2} = 0.6 \pm 0.1$. The propagation efficiency from M_2 to detectors (D_1, D_2) is $\alpha_P = 0.41 \pm .03$, with then each detector receiving half of the photons. The avalanche photodiodes (D_1, D_2) have quantum efficiencies $\alpha_P = 0.49 \pm 0.05$.

Data are acquired for each trapped atom by cycling through probing, testing, and cooling intervals (of durations $\Delta t_{probe} = 500$ μs, $\Delta t_{test} = 100$ μs and $\Delta t_{\text{cool}} = 1.4$ ms, respectively) using a procedure similar to that of Ref. [7]. The test beam is polarized along $\hat{z}$ and resonant with the cavity. All probing/cooling cycles end after an interval $\Delta t_{tot} = 0.3$ s, at which point a new loading cycle is initiated. We select for the presence of an atom by requiring that $T_{zz}(\omega_p \simeq \omega_{C_1}) \lesssim 0.35$ for the test beam. We employ only those data records associated with probing intervals after which the presence of an atom was detected. The intracavity photon number in mode l_y due to the probe field $\mathcal{E}_p^y$ on resonance, in the absence of an atom, is 0.21, and the polarizing beam splitter at the output of the cavity (PBS in Fig. 3.15(c)) suppresses detection of this resonant light by a factor of ~ 94. A repumping beam transverse to the cavity

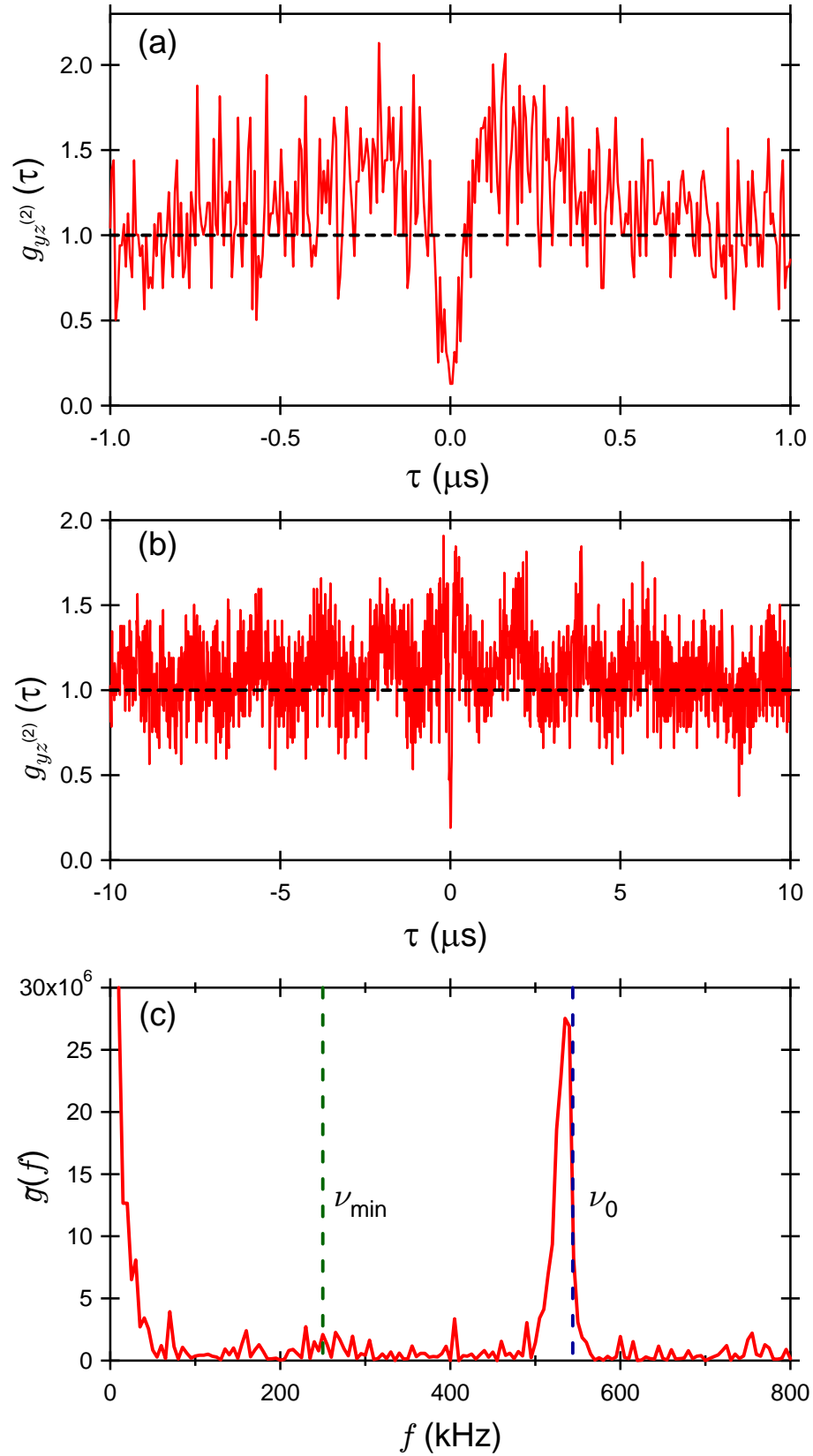---

[11]Data presented here was taken on 3/10/05.

Figure 3.17: Intensity correlation function (a) zoomed in on nonclassical features; (b) zoomed out to show the modulation due to axial motion; (c) Fourier transform.

axis and resonant with $6S_{1/2}, F = 3 \to 6P_{3/2}, F' = 4'$ also illuminates the atom during the probe and test intervals. This beam prevents accumulation of population in the $F = 3$ ground state caused by the probe off-resonantly exciting the $F = 4 \to F' = 4'$ transition.

Fig. 3.17 presents an example of $g_{yz}^{(2)}(\tau)$ determined from the recorded time-resolved coincidences at (D_1, D_2), for incident excitation with polarization along $\hat{y}$ and detection with orthogonal polarization $\hat{z}$. In Fig. 3.17 (a), the manifestly nonclassical character of the transmitted field is clearly observed with a large reduction in $g_{yz}^{(2)}(0)$ below unity, $g_{yz}^{(2)}(0) = (0.13 \pm 0.11) < 1$, corresponding to the sub-Poissonian character of the transmitted field, and with $g_{yz}^{(2)}(0) < g_{yz}^{(2)}(\tau)$ as a manifestation of photon antibunching [34]. The intensity correlation function $g_{yz}^{(2)}(\tau)$ displayed in Fig. 3.17 is shown with a resolution of 6 ns for panel (a), and 12 ns for (b), and has been corrected for background counts due to detector dark counts and scattered light from the repumping beam. Absent this correction, $g_{yz}^{(2)}(0) \simeq (0.18 \pm 0.10)$ is directly derived from the recorded counts. We find that $g^{(2)}(\tau)$ rises to unity at a time $\tau = \tau_B \simeq 45$ns, which is consistent with a simple estimate $\tau_- = 2/(\gamma + \kappa) = 48$ ns based upon the lifetime for the state $|1, -\rangle$.

Although for small $|\tau|$ our observations of $g_{yz}^{(2)}(\tau)$ are in reasonable accord with the predictions from our theoretical model, there are significant deviations on longer time scales. Evident in Fig. 3.17 (b) is a pronounced modulation that is not present in the model and which arises from the center-of-mass motion of the trapped atom. In support of this assertion, Fig. 3.17(c) displays the Fourier transform $\tilde{g}(f)$ of $g_{yz}^{(2)}(\tau)$ which exhibits a narrow peak at frequency $f_0 \simeq 535$ kHz just below the independently determined frequency $\nu_0 \simeq 544$ kHz for harmonic motion of a trapped atom about an antinode of the FORT in the axial direction x, which is indicated by one of the vertical dotted lines . This modulation is analogous to that observed in Ref. [57] for $g^{(2)}(\tau)$ for the light from a single ion, which arose from micro-motion of the ion in the RF trap. Here, $U(\vec{r}) = U_0 \sin^2(2\pi x/\lambda_{C_2}) \exp(-2\rho^2/w_{C_2}^2)$ is the FORT potential, which gives rises to an anharmonic ladder of vibrational states with energies $\{E_m\}$. There are $\simeq 100$ bound states in the axial dimension for radial coordinate

$\rho \equiv \sqrt{y^2 + z^2} = 0$. The anharmonicity leads to the observed offset $f_0 < \nu_0$ due to the distribution of energies for axial motion in the FORT well. Indeed, the frequency $\nu_{\min} = (E_{m_{\max}} - E_{m_{\max}-1})/h$ at the top of the well is approximately half that at the bottom of the well, $\nu_0 = (E_1 - E_0)/h$. By comparing the measured distribution of frequencies exhibited by $\tilde{g}(f)$ with the calculated axial frequencies $\{\nu_m\}$, we estimate that those atoms from which data was obtained are trapped in the lowest lying axial states $m \lesssim 10$, which corresponds to a maximum energy $E/k_B \sim 250~\mu$K. This energy estimate is consistent with other measurements of $g_{yz}^{(2)}(\tau)$ that we have made, as well as the Fourier transform of the record of the transmitted intensity and the transmission spectra of Ref. [7].

We have demonstrated photon blockade for the transmission of an optical cavity strongly coupled to a single trapped atom [45, 46, 47, 48, 52, 36, 53]. The observed nonclassical photon statistics for the transmitted field result from strong nonlinear interactions at the single-photon level, in analogy with the phenomena of Coulomb blockade for electron transport [43, 44, 58]. Extensions of our work include operation in a pulsed mode as was analyzed in Ref. [45], thereby realizing a source for single photons "on demand." As we improve the effectiveness of our cooling procedure, we should be able to explore the dependence of $g_{yz}^{(2)}(\tau)$ on probe detuning, $\omega_p - \omega_0$, as well as to move to higher levels of excitation to increase the output flux.

Chapter 4

Simple auxiliary measurements

This chapter lists the few basic measurements which determine some of the parameters relevant to our experiment. The values given here are the most recently measured ones.

4.1 Cavity length

Knowing the separation between the mirrors that form our physics cavity is important for being able to predict the mode orders of the various beams, as well as their associated mode structure. The mode orders, in turn, set the axial registration, i.e., the degree of overlap between the "pancake" structures of fields with different wavelengths, such as the FORT and the cavity QED field.

To determine the length l of a Fabry-Perot optical cavity, one usually measures the frequency spacing between consecutive longitudinal modes, also known as the free spectral range ν_{FSR} (see Ref. [59], Sec. 11.5). In practice, this amounts to finding the frequencies of a few axial modes that come into resonance at the same cavity length.

For an ideal cavity, the wavelength λ_n associated with mode order n is related to the physical mirror separation l by the simple relation $l = n(\lambda_n/2)$, whereas its frequency ν_n is an integer multiple of the free spectral range: $\nu_n = n\nu_{FSR} = n(c/2l)$. These relations become only approximately true for real mirrors, with the approximation getting worse the farther we get from the wavelength λ_C with optimal mirror reflectivity, also known as the center of the coating curve, in our case specified at

λ [nm]	ν_n [THz]	n	laser
827.685	362.206	102	locking
835.750	358.711	101	locking
852.357	351.722	99	probe
935.586	320.433	90	FORT

Table 4.1: Measured cavity resonances, and inferred mode orders.

$\lambda_C \simeq 850$ nm. The free spectral range is no longer independent of wavelength, since dispersion in the mirror coatings introduces frequency dependent phase shifts on the light. For each pair of consecutive modes, the frequency separation ν_{FSR} between them is given by $\nu_{FSR} = c/(2l_{\text{eff}})$. Here l_{eff} is an effective, "measured" cavity length derived from the free spectral range, and larger than the actual physical separation between the mirrors since some light penetrates the first few dielectric layers of the coatings. Near the coating curve center, where the free spectral range variation with wavelength is slow, the physical mirror separation l and the effective length l_{eff} are related by [60]:

$$l \simeq l_{\text{eff}} - \frac{\lambda_C}{2(n_H - n_L)} \simeq l_{\text{eff}} - 1.633 \, \frac{\lambda_C}{2} \,, \tag{4.1}$$

where n_H and n_L are the high and low index materials of the dielectric stacks that form the mirrors, in our case $n_H = 2.0564$ and $n_L = 1.4440$.

To find the cavity resonances, we first tune the probe laser as usual to the $F = 4 \rightarrow F' = 5'$ line. We then adjust the FORT and locking lasers' frequencies so that their cavity transmission peak centers overlap with that of the probe, while keeping track of all the wavelengths on a Burleigh WA-10 wavemeter. The dominant source of error here is the wavemeter precision, of about 450 MHz. Note that the only laser in our lab with enough tunability to scan over an entire free spectral range is the locking laser, a Newfocus 6227 diode, which we normally use for cavity length stabilizing. Table 4.1 lists the measured wavelengths, and their associated frequencies.[1]

The first two rows of Table 4.1 represent consecutive modes, so their frequency

---
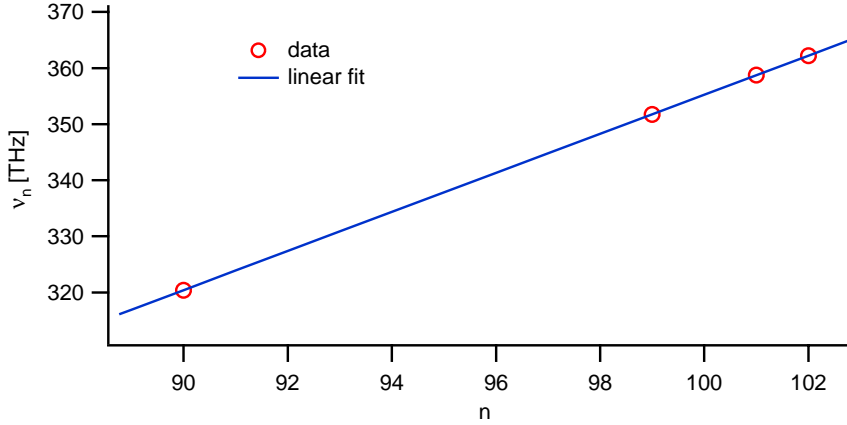
[1]Measured on 8/25/04 and 9/22/04.

Figure 4.1: Measured cavity resonances and their respective mode orders

separation is actually the free spectral range at or near those wavelengths, $\nu_{FSR}(\lambda \simeq 832$ nm$) = 3495.3$ GHz. Since the next two frequencies are separated by nearly twice that number, we infer that they must be two mode orders apart, and that the free spectral range in that region is $\nu_{FSR}(\lambda \simeq 844$ nm$) = 3494.5$ GHz. Hence the effective cavity length is $l_{\text{eff}}(\lambda \simeq 844$ nm$) \simeq l_{\text{eff}}(\lambda = \lambda_C) = 42.895 \pm 0.007$ μm, where the error bars come from the wavemeter resolution. Plugging this number into (4.1), we arrive at the physical mirror separation $l = 42.201 \pm 0.007$ μm. Now the frequencies in the second column are close to integer multiples of $c/2l$, which integers we infer to be the associated mode orders, and we list in the third column.

Fig. 4.1 shows a linear fit to the measured mode frequencies, versus their inferred mode numbers. The good agreement between the fit and the data shows that the free spectral range ν_{FSR} and the effective cavity length l_{eff} do not vary significantly over the range of our measurement.

A more careful estimation of the cavity length and mode orders is done by Kevin Birnbaum in his thesis (Ref. [9], Appendix A). Using the same data, he finds $l = 42.207 \pm 0.005$ μm, and the same mode orders as those listed in Table 4.1.

4.2   Cavity mode waist

To estimate the intensity of cavity-coupled light at the atom's location, for instance for calculating the maximal FORT depth or atom-cavity coupling, it is important to know what the mode spot size is. The mode waist w_0 for a particular wavelength λ is completely determined by the cavity geometry, since the boundary condition at the mirror surface enforces a match between the radius of curvature of the mirror and that of the Gaussian wavefront. For a symmetric cavity of length l and with mirror radius of curvature R, the waist spot size at the cavity center is (Sec. 19.2 of [59]):

$$w_0 = \sqrt[4]{\frac{l}{2}\left(R - \frac{l}{2}\right)\left(\frac{\lambda}{\pi}\right)^2}.$$ (4.2)

The cavity length l (and the associated l_{eff}) can be figured out from the free spectral range, as in Sec. 4.1 above, while the mirror curvature R can be estimated from a measurement of the transverse mode spacing ν_T ([59], Sec. 19.3):

$$R = \frac{l_{\text{eff}}}{1 - \cos(2\pi\nu_T\ l_{\text{eff}}/c)}.$$ (4.3)

This expression comes from evaluating the phase that a transverse mode accumulates as it propagates through the cavity, including the part of the mode volume which lives within the mirror coatings. Hence, we use here the effective length, rather than the physical separation between the mirrors ([61], Sec. 7.5).

For a probe beam that is properly aligned, modes with odd spatial symmetry or with a high mode index have low coupling efficiency, so in order to determine the transverse mode spacing it is easiest to measure the frequency spacing $2\nu_T$ between the TEM_{00} and the TEM_{02} modes. The probe is tuned to the $F = 4 \rightarrow F' = 5'$ transition at $\lambda_p = 852.356$ nm, which at first is on a TEM_{00} mode. We lock the cavity length as usual to the locking laser's blue sideband, ν_{s1} above the carrier, whose wavelength λ_{1l} is measured with a wavemeter. Next, we adjust the locking laser wavelength so that the cavity length, when locked, now comes into resonance with the probe's TEM_{02} mode. If the new carrier-to-sideband spacing and locking

laser	λ [nm]	w_0 [μm]
locking	836	23.5 ± 0.2
probe	852	23.7 ± 0.2
FORT	936	24.8 ± 0.2

Table 4.2: Estimated mode waists at cavity center.

laser wavelength are ν_{s2} and λ_{2l}, then the transverse mode spacing is

$$\nu_T = \frac{1}{2} \frac{\lambda_{1l}}{\lambda_p} \left(\frac{c}{\lambda_{1l}} + \nu_{s1} - \frac{c}{\lambda_{2l}} - \nu_{s2} \right). \tag{4.4}$$

For $\lambda_{1l} = 835.749$ nm, $\nu_{s1} = 505.7$ MHz, $\lambda_{2l} = 835.858$ nm, and $\nu_{s2} = 622.7$ MHz[2], (4.4) gives $\nu_T = 22.9 \pm 0.4$ GHz, where the uncertainty comes from the wavemeter resolution of 1 pm. Now to compute the mirror radius of curvature we can use Eqn. (4.3) to find $R = 20.3 \pm 0.8$ cm. Note that the specified radius of curvature is 20 cm, with error bars of a few percent (but less than 10%) according to the manufacturer, REO. Finally, Eqn. (4.2) leads to our estimate of the mode waist, for each of the wavelengths we are interested in, shown in Table 4.2.

Alternatively, one could use the measurement result for ν_T as a different way of estimating the cavity length l_{eff}, considering $R = 20$ cm to be a given, known quantity ([61], Sec. 7.5). We have to invert Eqn. (4.3), i.e., to solve for l_{eff} in

$$\nu_T = \frac{c}{2\pi l_{\text{eff}}} \cos^{-1} \left(1 - \frac{l_{\text{eff}}}{R} \right) \simeq \frac{c}{\pi \sqrt{2 l_{\text{eff}} R}}, \tag{4.5}$$

where the approximation is valid for $l_{\text{eff}}/R \ll 1$, giving $l_{\text{eff}} = 43.5 \pm 1.6$ μm. Note that this result is consistent with the value obtained from the free spectral range measurement in Sec. 4.1.
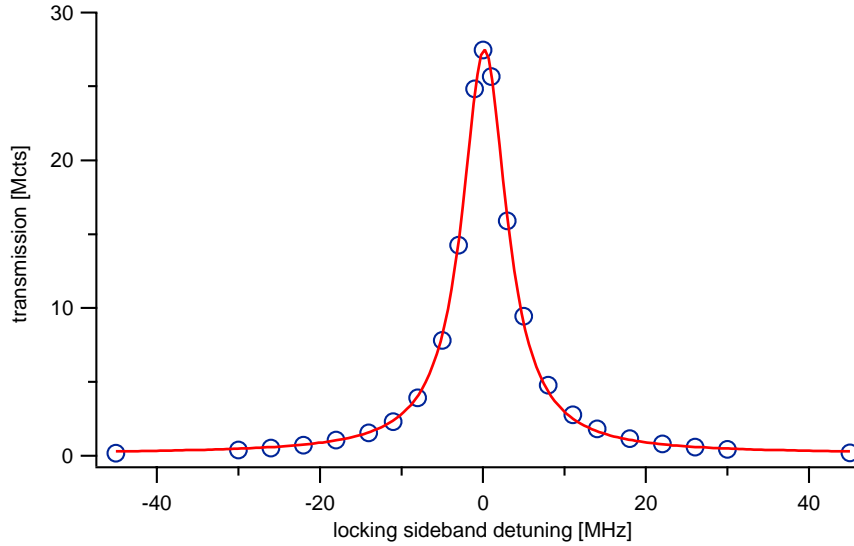
---

[2]Measured on 9/2/04.

Figure 4.2: Cavity transmission as a function of the locking laser detuning from its value on resonance. Fit yields $\kappa = 2\pi \times 3.3$ MHz.

4.3 Cavity linewidth

The cavity linewidth κ at the probe wavelength is an essential parameter for the master equation describing our system. Also, knowing the finesse of our cavity at the FORT and locking laser wavelengths is important for estimating the AC Stark shifts that these beams create. There are several different ways one can determine the linewidth in the lab [61], of which we will see a few examples below.

First, let us consider measuring the cavity linewidth at 852 nm, the probe wavelength. To see a simple Lorentzian transmission profile of the cavity versus detuning from resonance, it is important to excite only one of the two orthogonal cavity modes (see Sec. 4.6), so the probe needs to be polarized along one of the birefringent axes. Then one can keep the probe at a fixed frequency, and detune the cavity by a known, variable amount. We do this by changing the carrier-to-sideband spacing for our locking laser. While the carrier stays locked to a fixed frequency with respect to the probe and to Cesium, the cavity tracks along with the locking laser's movable sideband. For each value to which the sideband frequency is incremented, we record the cavity transmission, as measured in clicks from the photon counters. A Lorentzian fit
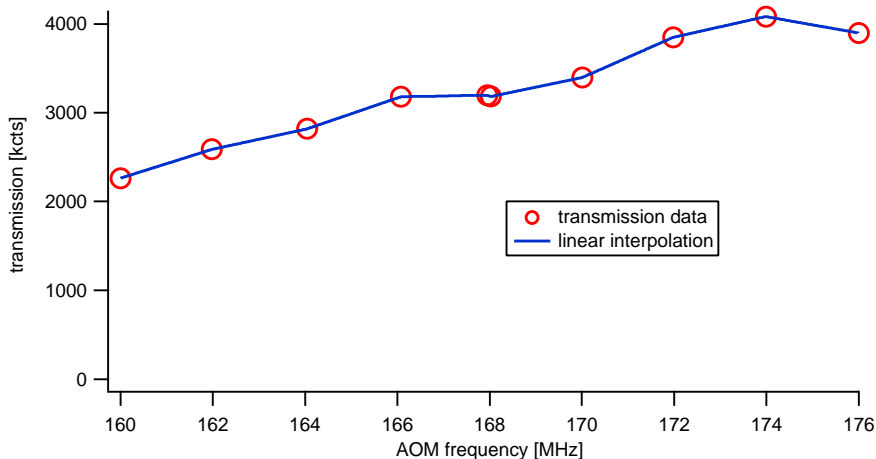
Figure 4.3: Normalization curve for cavity transmission.

to the probe transmission averaged over the two detectors, versus the locking laser's sideband frequency, will have half width at half maximum $(\kappa/2\pi)(\lambda_p/\lambda_l)$.

Fig. 4.2 shows the result of such a measurement[3], where each point represents the sum over 50 sweeps, about 330 ms per sweep. We get $\kappa = 2\pi \times (3.27 \pm 0.04)$ MHz, where the error bars reflect a 68% confidence interval for the fit.

A different way of measuring κ at this wavelength is to keep the cavity at a fixed length, and vary the probe detuning. This is complicated by the fact that to change the probe beam detuning, we use an AOM, the efficiency and steering of which, even when double-passed, will depend on the frequency. So one would have to readjust both the RF power going to the AOM, and the probe alignment into the cavity, for each probe detuning. Or instead, to make things easier, one can obtain a normalization curve, reflecting how the transmission changes due to the varying cavity alignment and input power alone, decoupled from the effect of the cavity-probe detuning.

Fig. 4.3 shows such a calibration curve[4]. The probe beam frequency was varied with a double-passed, down-shifting AOM resonant at 200 MHz, and for each point the cavity was retuned to be in resonance with the probe. The AOM frequency of 168 MHz corresponds to the $F = 4 \rightarrow F' = 5'$ transition. As the AOM gets closer to its

---

[3]Measured on 10/12/04.
[4]Measured on 6/21/04.
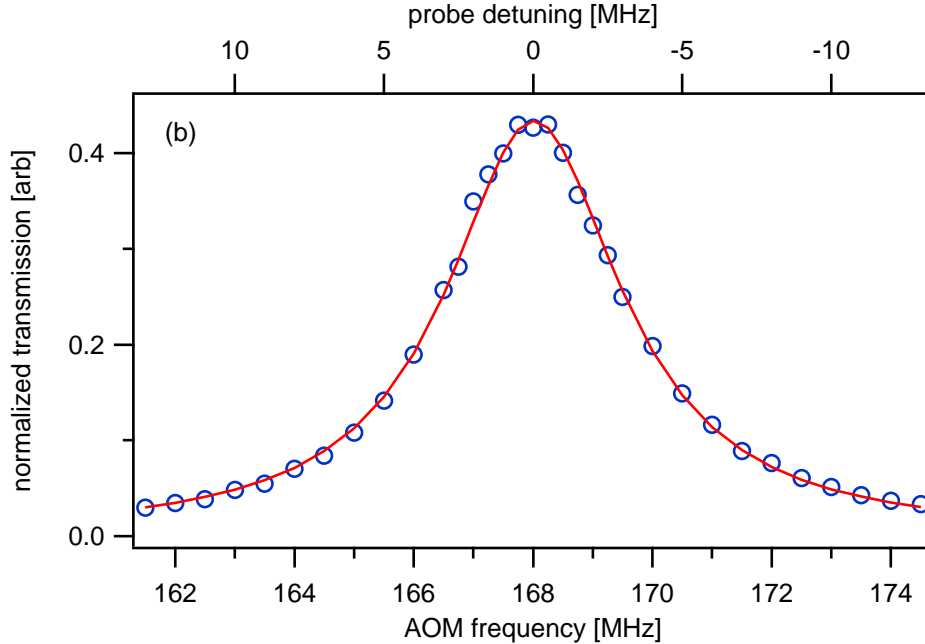
Figure 4.4: Lorentzian fit to the calibrated cavity transmission as a function of probe detuning, yielding $\kappa = 2\pi \times 3.6$ MHz.

center frequency, it outputs more optical power for the same RF input power, leading to the positive slope evident in the figure. Given this calibration data (circles), we can linearly extrapolate (line) a normalization factor for any frequency in its range.

The next step is to vary the probe frequency again, this time keeping the cavity locked in resonance with the $F = 4 \rightarrow F' = 5'$ atomic line. The resulting transmission versus frequency, as recorded with the APDs, needs to be divided by the normalization extracted from a curve of the type in Fig. 4.3, before fitting a Lorentzian to it. Such a measurement[5] is shown in Fig. 4.4, and the corresponding fit gives $\kappa = 2\pi \times (3.56 \pm 0.06)$ MHz.

We have so far shown measurements of κ done by detuning the cavity and keeping the probe at a fixed frequency, or by detuning the probe and keeping the cavity at fixed length; yet another type of measurement, similar to the latter, is described in Sec. 2.4. Depending on how they were measured, the different values for κ can differ by as much as 20%, but we do not have any good explanation for this inconsistency.

[5]Measured on 6/10/04.

A candidate culprit was the possibility that those measurements which appear to yield a larger κ are done with the input polarization tilted away from the intended birefringent axis (see Sec. 4.6). Indeed, if the input angle θ_i is about $30°$ off axis, the output line shape still gives a good fit to a Lorentzian, with linewidth greater than the real κ by about 10%. However, a larger discrepancy in linewidth cannot be explained away in this fashion, as it would give blatantly non-Lorentzian output shapes.

As for the cavity linewidth at the FORT wavelength $\lambda_{\text{FORT}} = 936$ nm, one easy way of estimating it is by using the $\lambda_l = 836$ nm locking laser's sidebands as yardsticks. One can scan the cavity and watch both the FORT and the locking laser transmission peaks on the same oscilloscope. The locking laser's sidebands will be separated by a known frequency $2\nu_s$, which on the scope will correspond to a time delay t_s. This effectively calibrates the time axis in frequency units, assuming that the piezo scan is roughly linear over the voltage range relevant for the measurement. If the FORT half-maximum points are separated by a time delay $t_{1/2}$, then the cavity decay rate is $(\lambda_l/\lambda_{\text{FORT}})(\nu_s/t_s)\,t_{1/2}$. We used $2\nu_s = 1.0$ GHz and got $t_s = 4.25 \pm 0.25$ ms and $t_{1/2} = 7.50 \pm 0.25$ ms for our particular scanning speed, where the uncertainty is the smallest time division for the chosen scope setting[6]. So the cavity decay rate (half width at half maximum) is 0.79 ± 0.07 GHz at the FORT wavelength.

4.4   Mirror transmission and losses

The finesse $\mathcal{F}$ of a cavity is given by

$$\mathcal{F} \equiv \frac{\nu_{FSR}}{2(\kappa/2\pi)} = \frac{2\pi}{T_1 + T_2 + A_1 + A_2} \,, \tag{4.6}$$

where ν_{FSR} is the cavity's free spectral range, κ is the linewidth, T_1 and T_2 are the two mirror transmission coefficients, and A_1 and A_2 are the losses associated with absorption and scattering by the mirror coatings. For nominally identical mirrors,
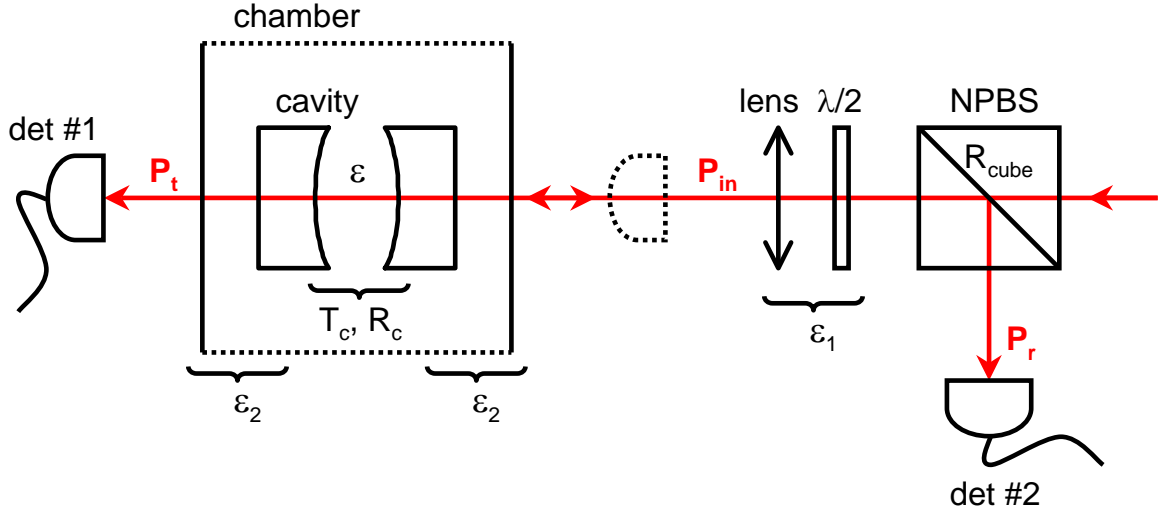
---

[6]Measured on 1/10/04.

Figure 4.5: Setup for measuring the ratio of absorption to transmission for our physics cavity mirrors.

such as those in our physics cavity, the finesse is simply given by $\mathcal{F} = \pi/(A + T)$, where A and T are the loss and the transmission coefficients per mirror.

Thus our previous measurements of the free spectral range (Sec. 4.1) and of the cavity linewidth (Sec. 4.3) are sufficient to specify the sum of the losses and transmission:

$$A + T = \frac{\kappa}{\nu_{FSR}} \, . \tag{4.7}$$

If $\kappa = 2\pi \times 3.6$ MHz for the probe, and $\nu_{FSR} = 3.495$ THz, we get a finesse of about 485000, hence $A + T = 6.5 \ 10^{-6} = 6.5$ ppm. For the FORT, the 0.79 GHz linewidth implies a finesse of about 2200.

However, knowledge of A and T individually, or equivalently of their ratio, is also needed, for instance for the purpose of estimating the cavity escape efficiency, and hence of inferring the intracavity photon number from a given detection rate.

Fig. 4.5 schematically depicts the setup one can use for measuring the A/T ratio, which basically duplicates the one used for Ref. [60]. The probe beam polarization is set with a half wave plate to match one of the two birefringent cavity axes (see Sec. 4.6), and the light is coupled into the cavity as usual with a mode-matching lens. The combined transmission coefficient of the lens and waveplate is ϵ_1, which can be

independently measured. The vacuum chamber window and the mirror substrate have a combined unknown transmission coefficient ϵ_2, one on each side of the cavity. The mode matching efficiency ϵ to the cavity is also unknown at this stage. For measuring a calibrated fraction of the power reflected by the cavity, one can place on the input side a non-polarizing beam splitter of known reflectivity R_{cube}. Furthermore, assume P_{in} is the input power to the cavity right outside the vacuum chamber; P_t is the height of the cavity transmission peak on resonance; and the power reflected back by the cavity and the non-polarizing cube is P_r^{off} off resonance, and P_r^{on} on resonance at the bottom of the reflection dip.

The cavity transmission and reflection coefficients on resonance can be expressed in terms of the mode matching ϵ and the ratio of losses to transmission (see Refs. [60] and [59] Sec. 11.4):

$$T_{cav} = \frac{\epsilon}{(1 + A/T)^2} \tag{4.8}$$

$$R_{cav} = \frac{\epsilon(A/T)^2}{(1 + A/T)^2} + (1 - \epsilon), \tag{4.9}$$

whereas the reflection coefficient off resonance is 1. The reflected and transmitted powers can thus be related to the input power as follows:

$$P_r^{on} = P_{in}\epsilon_1\epsilon_2^2 R_{cav} R_{cube} \tag{4.10}$$

$$P_r^{off} = P_{in}\epsilon_1\epsilon_2^2 R_{cube} \tag{4.11}$$

$$P_t = P_{in}\epsilon_2^2 T_{cav} . \tag{4.12}$$

From (4.11) we get $\epsilon_2 = \sqrt{P_r^{off}/P_{in}\epsilon_1 R_{cube}}$, so we just need to solve Eqns. (4.10) and (4.12), for ϵ and A/T as the two remaining unknowns, yielding

$$\epsilon = \frac{(P_r^{off} - P_r^{on} + P_t R_{cube}\epsilon_1)^2}{4P_r^{off} P_t R_{cube}\epsilon_1}, \tag{4.13}$$

$$\frac{A}{T} = \frac{P_r^{off} - P_r^{on} - P_t R_{cube}\epsilon_1}{2P_t R_{cube}\epsilon_1}. \tag{4.14}$$

In a measurement of this type[7], we got $R_{cube} = 0.48$, $P_{in} = 3.87\,\mu$W, $P_t = 0.74\,\mu$W, $P_r^{off} = 1.71\,\mu$W, and $P_r^{on} = 0.97\,\mu$W. All these values are measured with fluctuations of about 1%, which we will take to be the uncertainty. We assume $\epsilon_1 = 0.99$ since both the lens and the waveplate are anti-reflection coated. We then get $\epsilon_2 = 0.96 \pm 0.02$, $\epsilon = .49 \pm 0.10$ and $A/T = 0.55 \pm 0.21$.

Since we already know the sum $A+T = 6.5$ ppm, we can now estimate the loss and transmission coefficients at the probe's wavelength, $A = 2.3$ ppm, and $T = 4.2$ ppm.

4.5   Ground state AC Stark shifts

Of the dipole-allowed transitions connecting the Cesium ground state to its excited states, the most relevant ones for our experiments are the D_2 line, $6S_{1/2} \rightarrow 6P_{3/2}$ at $\lambda_{D2} = 852.3$ nm, and the D_1 line, $6S_{1/2} \rightarrow 6P_{1/2}$ at $\lambda_{D1} = 894.6$ nm. Considering only these two transitions, the AC Stark shift of the atomic ground state in a linearly polarized, far detuned light trapping field of intensity I_0 and wavelength λ is well approximated by [33, 62]:

$$U_0 = \frac{(\gamma/2\pi)^2 I_0}{6 I_{sat}} \left(\frac{1}{\delta_{D1}} + \frac{2}{\delta_{D2}} \right),\qquad (4.15)$$

where $\gamma = 2\pi \times 2.6$ MHz is the D_2 linewidth, $I_{sat} = 8\pi^3 \hbar c(\gamma/2\pi)/3\lambda_{D2}^3 = 1.1$ mW/cm^2 is its saturation intensity, and

$$\delta_{D1,2} = \frac{c(\lambda - \lambda_{D1,2})}{\lambda \lambda_{D1,2}}\qquad (4.16)$$

are the frequency detunings of the trapping field with respect to the two relevant transitions. If the light at λ is coupled to a cavity mode with waist w_0, then for an optimally coupled input power P, the peak intracavity intensity is

$$I_0 = \frac{8P}{\pi T w_0^2}\ ,\qquad (4.17)$$
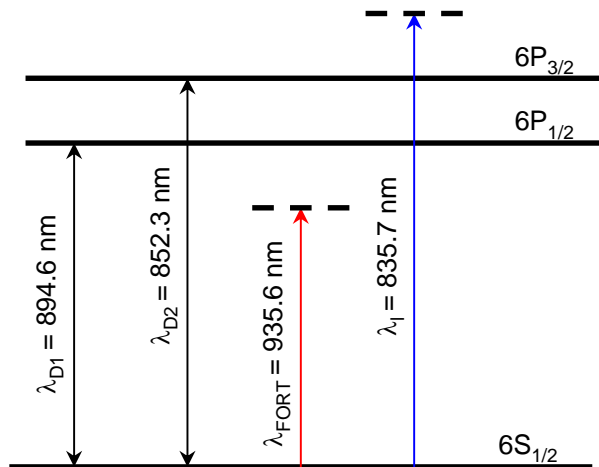
---

[7]Measured on 12/21/03.

Figure 4.6: Relevant dipole transitions for the Cesium ground state; wavelengths shown for the FORT and locking laser, for comparison (not to scale).

where as before T denotes the transmission coefficient per mirror, at wavelength λ.

As an example, let us compute the ground state potential depth of our FORT, knowledge of which is important for predicting and cooling the atomic motion in the trap. Suppose we measure the height of the FORT transmission peak on resonance right outside our chamber window, at the FORT wavelength, to be $P = 1.0$ mW, a value typical of what we use in the lab. A separate measurement[8] of the power transmission through two consecutive vacuum chamber windows, bypassing the cavity, yielded 92% at $\lambda = \lambda_{\mathrm{FORT}} = 935.6$ nm, which as an aside we should note that it is the same as the value for $(\epsilon_2)^2$ at 852 nm found in Sec. 4.4. This means that the cavity output power inside the chamber is $P_t = P/\epsilon_2 \simeq 1.04$ mW. From this, we need to infer the quantity ϵP_{in}, which is the useful part of the input power that gets coupled into the cavity (note that we need to find neither ϵ nor P_{in} separately). Since we are far from the mirror coating curve center, we can assume that at this wavelength the mirror transmission far exceeds the losses caused by absorption and scattering, so that the finesse $\mathcal{F} = \pi/(T + A) \simeq \pi/T$, which for $\mathcal{F} = 2200$ (see Sec. 4.4) implies $T = 1.4 \times 10^{-3}$. From (4.8) we see that $P_t = \epsilon P_{in}/(1 + (A/T)^2) \simeq \epsilon P_{in}$ for $T \gg A$; in other words, far from the coating curve optimum the output power nearly equals the

---

[8]Measured on 10/8/04.

mode-matched power. Sec. 4.2 gives the FORT waist $w_0 = 24.8$ μm, so from (4.17) we can obtain the intracavity intensity, a toasty $I_0 = 3.0 \times 10^8$ mW/cm^2! Finally, (4.15) gives our estimate of the trap depth per mW of cavity output power measured outside the chamber, namely $U_0 = 40.9$ MHz, or about 2 mK.

Another wavelength of interest is that of the locking laser, which ideally should not significantly affect the atom's trapping potential. Since $\lambda_l \neq \lambda_{\text{FORT}}$, this laser adds a bump, out of axial registration with the trapping potential wells. Note that we are talking about a repulsive potential "bump" as opposed to an attractive "dip," because the locking laser is blue detuned from both the D_1 and the D_2 lines (see Fig. 4.5). Is this extra potential energy significant?

If the locking laser's carrier transmission peak height is P_c, and the carrier-to-sideband power ratio is k, then the sideband power coupled into the cavity is $P = (P_c/k)(1 + (A/T)^2)$, from (4.8). We have no measurement of A/T at this wavelength, so let us assume, pessimistically, that the transmission is only slightly larger than at 852 nm, and that the losses stayed roughly the same, so that we would roughly estimate $A/T \sim 0.5$ at 836 nm. We measure $P_c = 0.39$ μW at the cavity output[9], and $k = 25.0$ from the voltage output ratio given by the photodetector we normally use for locking the cavity, assuming voltage to power linearity. Then we can use (4.15) to find $U_0 \simeq -650$ kHz, in this worst case scenario. So the potential bump created by the locking laser's sideband is only at most about 1.5% of the typical FORT well depth. Note that the carrier is completely negligible, since it is separated from the sideband, and hence from the cavity resonance, typically by about $\Delta = 2\pi \times 500$ MHz; so the cavity resonance profile suppresses it by a factor of the order $(\Delta/\kappa)^2 \simeq 1.5 \times 10^4$.

Much more information about the various AC Stark shifts the Cesium levels experience in a dipole trap, including the excited states and the effects of elliptical FORT polarization, can be found in Jason McKeever's and David Boozer's theses ([6, 1]).

---

[9]Measured on 8/24/04.

4.6 Cavity birefringence

Our physics cavity supports two orthogonal, non-degenerate modes. The difference between their resonance frequencies is called the birefringent splitting, and is presumably due to stress on the dielectric coatings, caused by the glue used for holding down the mirror substrates.

If we pick polarization basis vectors parallel to the two birefringent axes:

$$u_1 = \begin{pmatrix} 1 \\ 0 \end{pmatrix}, \text{ and } u_2 = \begin{pmatrix} 0 \\ 1 \end{pmatrix}, \tag{4.18}$$

then the cavity response to an incoming field of frequency ν (relative to the center of the cavity resonance feature) and of arbitrary polarization is given by the matrix

$$M_c = \begin{pmatrix} \dfrac{\kappa_1}{i\kappa_1 - \delta_B - \nu} & 0 \\ 0 & \dfrac{\kappa_2}{i\kappa_2 + \delta_B - \nu} \end{pmatrix}. \tag{4.19}$$

Here $\kappa_{1,2}$ are the linewidths of the two modes, and δ_B is half the birefringent splitting. One can easily see that, if the input to the cavity is along one of the birefringent axes, the output power spectrum, given by the absolute value squared of the electric field, will be a Lorentzian of half width κ_1 (κ_2) centered at $\nu = -\delta_B$ ($\nu = +\delta_B$).

The birefringent splitting is a parameter needed for precise predictions of the cavity output spectrum [7]. There are several different ways to measure the birefringence, and Theresa Lynn mentions many of them in her thesis [61]. Here I will give two examples.

First, let us consider the case when the input to the cavity is linearly polarized light, tilted at an angle θ_i with respect to birefringent axis u_1. Suppose we look at the cavity output through an analyzer, which selects out the polarization component tilted at an angle θ_f with respect to that same axis. The electric field coming out of this system will then be:

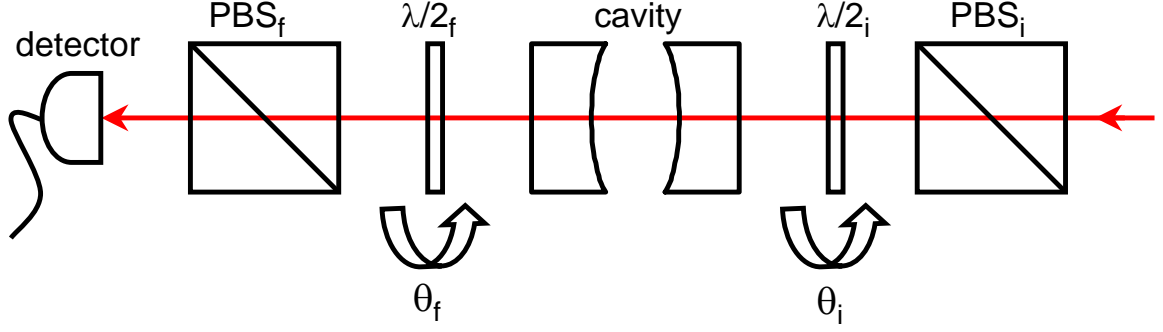$$E_l \sim P_1 R_{\theta_f} M_c R_{\theta_i} u_1, \tag{4.20}$$

Figure 4.7: Setup for measuring birefringence by injecting linearly polarized light to the cavity.

where P_1 is the projection onto u_1, and R_θ is a polarization rotation by angle θ:

$$P_1 = \begin{pmatrix} 1 & 0 \\ 0 & 0 \end{pmatrix}, \ R_\theta = \begin{pmatrix} \cos\theta & -\sin\theta \\ \sin\theta & \cos\theta \end{pmatrix}. \tag{4.21}$$

Putting Eqns. (4.18 – 4.21) together, we get the following expression for the output spectrum:

$$|E_l|^2 \ \sim \ \frac{\kappa_1^2 \cos^2\theta_f \cos^2\theta_i}{\kappa_1^2 + (\nu + \delta_B)^2} + \frac{\kappa_2^2 \sin^2\theta_f \sin^2\theta_i}{\kappa_2^2 + (\nu - \delta_B)^2} - \\ \frac{\kappa_1\kappa_2 \sin(2\theta_f)\sin(2\theta_i)(\nu^2 - \delta_B^2 + \kappa_1\kappa_2)}{2(\kappa_1^2 + (\nu + \delta_B)^2)(\kappa_2^2 + (\nu - \delta_B)^2)} \ . \tag{4.22}$$

Note that the first two terms recover the familiar Lorentzians associated with the modes $u_{1,2}$ and centered at $\mp\delta_B$, whereas the third term is an interference of the two.

One can measure such a spectrum with the setup shown schematically in Fig. 4.7. As a first step, one should identify one of the birefringent axes. This amounts to finding one of the two input axes for which the cavity output is closest to linear polarization. A convenient measure of polarization is the ellipticity ϵ, which reflects the maximum contrast one can obtain from light of given polarization:

$$\epsilon = \frac{P_{max} - P_{min}}{P_{max} + P_{min}}, \tag{4.23}$$

where P_{max} and P_{min} are the maximum and minimum power obtained after passing
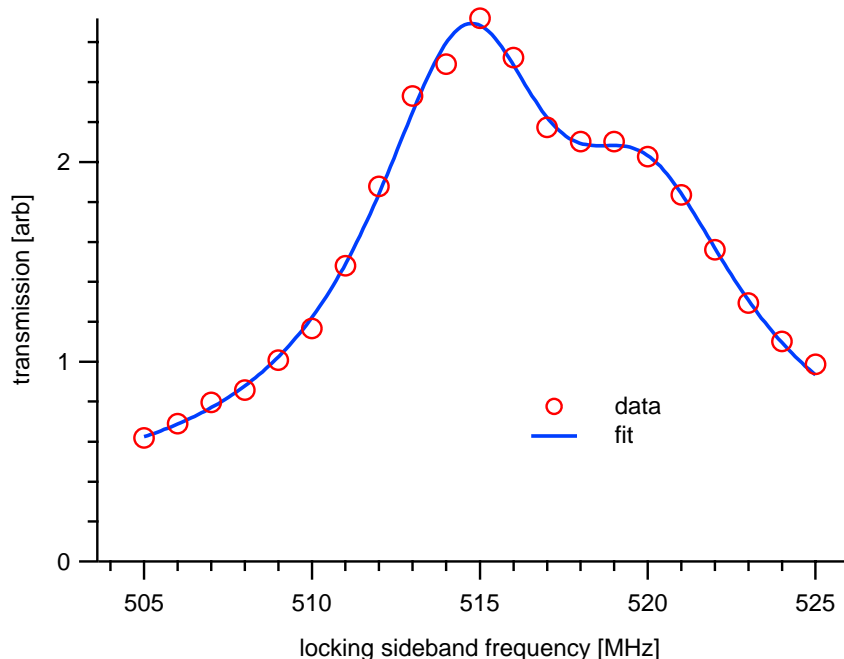
Figure 4.8: Example of a probe spectrum obtained for linearly polarized light at the cavity input.

the light through a rotatable polarizer, such as the one formed by the $\lambda/2_f$ waveplate and the PBS_f polarizer in the figure. One can easily show that perfectly linear light has $\epsilon = 1$, whereas circularly polarized light has $\epsilon = 0$. In our lab, the best measured ellipticity for 852 nm light coming out of the cavity was $\epsilon \simeq 0.995$, with the rule of thumb being that the input polarization needs readjustment if the ellipticity drops below 0.97.

Now once the angle settings for the input and output waveplates which give the maximal elipticity have been determined, one sets the polarizer and analyzer to different, but known angles. The resulting spectrum for the probe emerging from the cavity can be then used to infer the birefringent splitting $2\delta_B$. An example[10] is shown in Fig. 4.8, which plots the cavity transmission versus the carrier-to-sideband frequency separation for our locking laser (see Sec. 4.3 for an analogous measurement of κ). The solid curve shows a fit to the data with expression (4.22), up to a proportionality constant, with the constraint $\kappa_1 = \kappa_2$, and with the known output angle set

---

[10]Measured on 10/12/04.
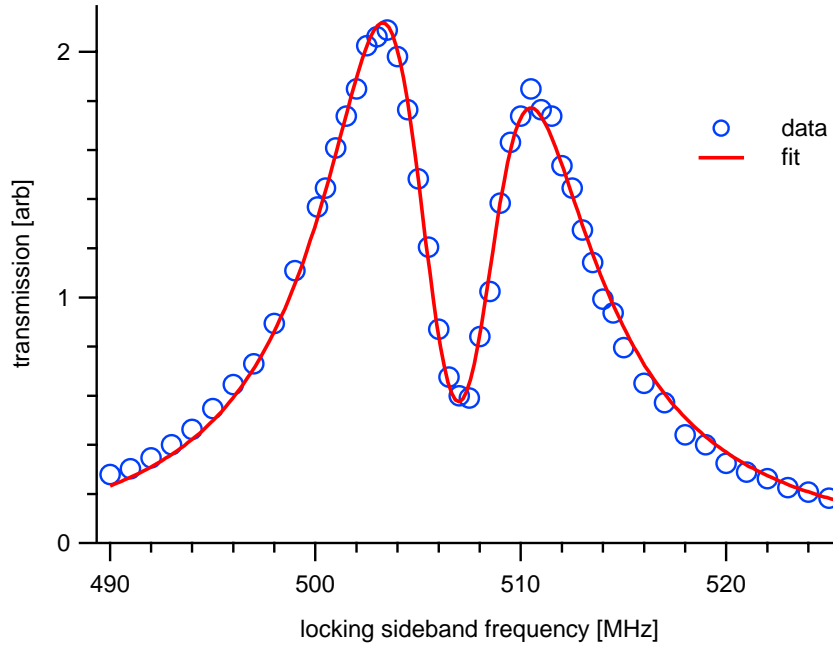
Figure 4.9: Example of a probe spectrum obtained for circularly polarized light at the cavity input.

to $\theta_f = -54°$. Unfortunately, the input angle was not independently measured for this example, so θ_i becomes an additional fit parameter. After adjusting by the usual λ_l / λ_p factor, the fit yields $\kappa = 2\pi \times 3.3 \pm 0.1$ MHz, and $2\delta_B = 2\pi \times 4.6 \pm 0.1$ MHz.

As a second example, let us see what happens when the input light is circularly, rather than linearly polarized. The analog of (4.20) for this case is:

$$E_c \sim P_1 R_{\theta_f} M_c u_+, \tag{4.24}$$

where u_+ is the vector representing σ^+ circularly polarized light,

$$u_+ = \begin{pmatrix} 1 \\ i \end{pmatrix}. \tag{4.25}$$

The power at the output is then proportional to

$$
\begin{aligned}
\mid E_c \mid^2 \quad \sim \quad & \frac{\kappa_1^2 \cos^2 \theta_f}{\kappa_1^2 + (\nu + \delta_B)^2} + \frac{\kappa_2^2 \sin^2 \theta_f}{\kappa_2^2 + (\nu - \delta_B)^2} + \\
& \frac{\kappa_1 \kappa_2 \sin(2\theta_f)(\nu(\kappa_2 - \kappa_1) + \delta_B(\kappa_1 + \kappa_2))}{(\kappa_1^2 + (\nu + \delta_B)^2)(\kappa_2^2 + (\nu - \delta_B)^2)} \; .
\end{aligned} \tag{4.26}
$$

The setup for measuring the birefringence in this configuration is very similar to the one in Fig. 4.7, the only difference being that the input half waveplate $\lambda/2_i$ is replaced by a quarter waveplate. An example of the spectrum measured this way[11] is shown in Fig. 4.9, where as before we varied the locking laser's sideband, and monitored the transmission. Fitting expression (4.26) to the data, with $\kappa_1 = \kappa_2$ as before, yields $\kappa = 2\pi \times 3.4$ MHz and $2\delta_B = 2\pi \times 4.0$ MHz.

The two measurements we talk about here were made some four months apart, and we think that the cavity birefringence might be slowly drifting over that kind of timescale. This would explain the $\sim 15\%$ discrepancy between the two different values of δ_B given above, though at this point we have not looked into the issue carefully enough to be sure.

4.7   Detection efficiency

Knowing the detection efficiency for photons emitted from the cavity is necessary for inferring from the detected rates the intracavity photon number, which governs the atom-cavity evolution. There are several different factors that contribute to the overall efficiency, i.e., to the probability that an intracavity photon eventually gets recorded by the P7888 card which acquires the pulses from our avalanche photodetectors (APDs). The cavity escape efficiency α_e is the probability that a photon created within the cavity will be transmitted out through one of the two mirrors. Also, the fact that we have a symmetric cavity means that photons can leave through either mirror, whereas we monitor the output on one side only, leading to another cut in efficiency, $\alpha_{2s} = 0.5$. There are also losses on the path from the cavity output to the

---

[11]Measured on 6/7/04.

name	symbol	value
escape	α_e	0.65 ± 0.09
two-sided	α_{2s}	0.5
propagation	α_p	0.40 ± 0.03
detector	α_d	0.53 ± 0.05
total	α	0.068 ± 0.015

Table 4.3: Efficiencies associated with probe propagation and detection.

inputs of the APDs, which we will call the propagation efficiency α_p. Finally, the detectors have a measurable quantum efficiency α_d.

To start with, let us consider the escape efficiency α_e. Of the photons within the cavity mirrors, a fraction proportional to the losses coefficient A will be scattered or absorbed, whereas a fraction proportional to the transmission coefficient T will escape to the outside world. So the escape efficiency is simply

$$\alpha_e = \frac{T}{A+T} = \frac{1}{1+A/T} = 0.65 \pm 0.09\,, \tag{4.27}$$

where we have used the A/T value found in Sec. 4.4.

Let us now turn to the "propagation" efficiency, i.e., the efficiency with which probe light just outside the output cavity mirror makes it to the two outputs (A and B) of the fiber coupler. The light attenuation along this path is mostly due to coupling from free space into the fiber mode, though the other optics also have non-trivial efficiencies. It is easier to make this measurement with much more probe power than we would normally use while running the whole experiment, say about 1 μW at the cavity input; the fiber coupler output powers P_A and P_B can then be measured with a sensitive power meter, such as the Newport 1830-C/818-SL, with the cavity locked on resonance with the probe. Now for the power right at the cavity output P_c, if we place a power meter against the chamber window, we will block the locking laser's path to its detector, so we will no longer be able to lock the cavity. But the transmitted probe

power can still be measured accurately, by turning the cavity scan off, and manually tuning the cavity in and out of resonance. The on- and off-resonant levels are most easily monitored on an oscilloscope connected to the calibrated analog output of the detector. Doing all that[12], we measured $P_c = 32.7 \pm 0.5$ nW, $P_A = 6.8 \pm 0.5$ nW, and $P_B = 6.6 \pm 0.4$ nW. The error bars reflect fluctuations in the detected power level, which are much greater after the fiber beam splitter, presumably due to an interference effect with light reflected off of the fiber input surface. We should also adjust the efficiency by the non-unity value for the window and substrate transmission coefficient ϵ_2 found in Sec. 4.4. The propagation efficiency is thus:

$$\alpha_P = \epsilon_2 \frac{P_A + P_B}{P_c} = 0.40 \pm 0.03 \,. \tag{4.28}$$

Once the photon has emerged from either fiber coupler output, what is the probability that our computer will register that event? We call this the detector efficiency, which incorporates any losses at the fiber connection to the APD, as well as the detector's quantum efficiency. The manufacturer (Perkin Elmer) specifies the typical detector efficiency for the SPCM-AQR-13-FC to be 0.5 at 830 nm. The trick to measuring this number is bridging the gap between the lowest power that a typical calibrated detector will go to, and the highest power the APDs will accept before saturation effects come into play. Specifically, our power meter has 100 fW resolution, whereas the APDs saturate at 10^6 counts/s (cps), which at 852 nm is about 230 fW. The solution is to first use a power meter to measure a relatively high power P_A at one of the fiber outputs, and then attenuate it by a known factor k before measuring the counting rate R_A with the APDs and the P7888. Upon doing such a measurement[13], we got $P_A = 4.5 \pm 0.4$ nm, $k = (68 \ \mu\text{W})/(3.4 \ \text{nW}) = 20000$, and $R_A = 513$ kcps. Thus the detector efficiency is:

$$\alpha_{APD} = \frac{R_A k}{P_A} \frac{hc}{\lambda} = 0.53 \pm 0.05 \,. \tag{4.29}$$

---

[12]Measured on 10/6/04.
[13]Measured on 6/3/03.

The various efficiencies are summarized in Table 4.3, which also includes the overall efficiency, $\alpha = \alpha_e \alpha_{2s} \alpha_p \alpha_d = 0.068 \pm 0.015$.

Appendix A

Current MOT setup

Over the past few years, several upgrades have been made to the cavity lab, in our continuing effort to make it more and more user-friendly, robust and customizable, hence able to withstand the increasing level of complexity in the experiments we needed to do. To enumerate a few of these new and improved components: the ADwin timing controller; the phase-locked Raman diode laser and the associated axial sideband cooling setup; the switchable bias coil power supplies for magnetic field nulling at the cavity location; and the robust injection-locked laser setup providing trapping light[1] for both MOTs in our experiment. This appendix focuses on the latter.

A.1   Brief note on magneto-optical traps

The magneto-optical trap (MOT), first realized experimentally in 1987 [63], has since become the standard source of cold atoms for our field. It is robust and relatively easy to set up, and it captures atoms from a room-temperature cloud, bringing them down close to the Doppler temperature, which for Cesium is $\hbar\Gamma/2k_B = 125\mu$K. We deliver atoms to our cavity by collecting about 10^5 of them in a MOT, from which the atoms are cooled to sub-Doppler temperatures, and then allowed to fall under gravity towards the slit between the cavity mirrors.

---

[1]In this appendix, "trapping" will refer to the MOTs above the cavity, not to be confused with the dipole-force intra-cavity trap mentioned elsewhere in the thesis.

A MOT is made of an inhomogeneous magnetic field and three intersecting pairs of counter-propagating trapping beams, one along each of three independent directions in space [64]. The magnetic field gradient can be provided by a pair of coils in an anti-Helmholtz configuration, with a magnetic zero in the region of overlap of the six beams, and linear variation close to the trap center, along all three axes. The trapping light is usually tuned about 1-2 natural linewidths below resonance with a cycling atomic transition, i.e., one for which the dipole selection rules prevent the atom from escaping to levels other than the two which form the transition. The closed transition we use is at $\lambda = 852.356$ nm, between the $6S_{1/2}, F = 4$ and $6P_{3/2}, F' = 5'$ levels of the $D2$ line of Cesium (see Fig. 2.4). In addition to the trapping light, a repumping beam is also needed, to ensure that in the rare event (about one excitation in 1000) that an atom decays to $F = 3$, it is returned to the useful $F = 4$ ground state in resonance with the trapping light. Our MOT repumper is tuned to the $6S_{1/2}, F = 3 \rightarrow 6P_{3/2}, F' = 3'$ transition at $\lambda = 852.335$ nm.

Since the trapping light is red-detuned, atoms moving towards an incoming laser beam are Doppler-shifted into resonance with it. Hence, the atoms will preferentially scatter light which opposes their motion, which leads to cooling. In addition to this damping mechanism known as "optical molasses," a MOT also provides, through its magnetic component, a position-dependent restoring force which holds the atoms in place. Namely, if the two beams in each trapping pair have opposite circular polarizations of appropriate handedness, the selection rules enforce preferential absorption of those photons which kick the atoms towards the trap's center. For more information on how a MOT works, please read Refs. [63, 65], for instance.

For obtaining sub-Doppler temperatures, the laser cooling technique that is most natural to use after having already collected the atoms in a MOT cloud is Sisyphus cooling in the $\sigma^+\sigma^-$ configuration. As an atom moves through the polarization gradient formed by the beam pair, the population gets distributed among its ground state sublevels in such a way that the atom scatters more counterpropagating than copropagating photons, leading to an unbalanced radiation pressure and hence to cooling. A good description of this polarization gradient (PG) cooling mechanism can be found

in Ref. [66]. Operationally, it merely amounts to turning off the magnetic fields, turning down the power in the trapping beams, and detuning them farther to the red from resonance than they were in the MOT.

So to make cold atoms, one needs magnetic field gradients and trapping and repumping light. Prior to my joining the cavity lab, the magnetic coils were working well enough, however all but one of the lasers providing the light were unreliable. A lot of time was wasted on maintenance on a daily basis just to keep them close to the necessary wavelength. There were four different diode lasers for providing the 40 mW of trapping light and 10 mW of repumping light in the two MOTs: three masters, each of them independently locked to Cesium, and one injection-locked slave, which nevertheless also had its own external cavity. Considering that each SDL-5421 laser diode can provide about 100 mW of power if grating-stabilized, and 150 mW when free-running, one can tell that the old setup was highly inefficient, even if taking into account the various propagation losses.

The MOT laser setup was then greatly simplified. We kept the only working laser to provide all the repumping light for both MOTs as well as the $F = 3$ lattice light. As for the trapping light, as well as the $F = 4$ lattice light, it is now all provided by just one laser: an injection-locked slave to the probe laser.

A.2   Injection locking

For a detailed treatment of injection locking, please see Ref. [59], Chapter 29. From a black-box point of view, injection locking can be thought of as just a way of effectively amplifying the power in an existing laser beam. More specifically, if one injects a small amount of light from a master laser into a free-running slave laser diode, the slave will begin lasing at the same frequency and phase as the injected light, provided that it is close enough to the free-running slave in frequency and spatial mode shape. For locking the 852 nm laser diodes we have tested in our lab, the capture range is hundreds of MHz, while the injected power can go as low as 1 μW and as high as a few hundred μW. An injection lock easily lasts for months without any adjustments,
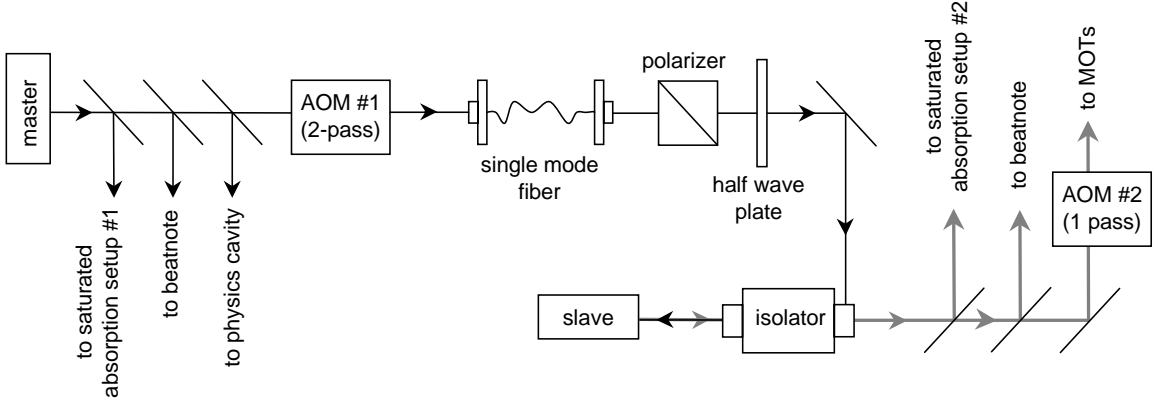
Figure A.1: Injection lock setup for delivering trapping light to our MOTs.

making it one of the few painless ways to provide a lab with moderate amounts of laser light. If a few hundreds of mW are ever needed in a lab, at an already available frequency, I would highly recommend several injection-locked slaves as a preferable alternative to a single high-power system such as a Ti-Saph, which typically requires weekly maintenance and at least daily locking.

An injection-locked slave is also the ideal power source for a system that requires the light to be shifted between several different frequencies without a change in alignment. Such a system is our MOT, which requires the trapping beams to stay put, while their frequency is shifted from the small detuning associated with the MOT loading, to the larger detuning for PG cooling. Frequency shifting of optical beams is usually done with acousto-optic modulators (AOMs), with the side effect of steering the beams more for larger drive frequencies, which in our case would lead to misalignment. The solution to this problem is illustrated in Fig. A.1, which depicts a type of system first set up by David Boozer for the atomic ensemble lab, then replicated by me for the cavity lab.

The basic idea is to use to our advantage the fact that an injection lock, though quite sensitive to the alignment of the input light, has a large dynamic range in input power. We start out with the master laser, which also provides the light for our cavity QED probe, and which is normally locked to the $4-5$ crossover of the $F=4$ line, i.e., to a frequency midway between $F=4 \rightarrow F'=4'$ and $F=4 \rightarrow F'=5'$, hence 125.5 MHz red detuned from the $F=4 \rightarrow F'=5'$ transition (see Fig. 2.4). For

shifting the light between the MOT and PG frequencies, we use AOM #1, which has a large 25 MHz bandwidth and is double passed to minimize beam steering and hence maximize fiber throughput. For the MOT setting, AOM #1 up-shifts the light by 2×114.15 MHz, and for the PG cooling by 2×99.0 MHz. The single-mode fiber converts the change in alignment between the two settings to a change in power, to which the injection lock is highly insensitive. To minimize feedback, we couple the light through the rejection port belonging to the output polarizer of the slave's optical isolator. The amount of light reaching the slave can be varied with a polarization rotator. AOM #2, down-shifting by 110 MHz, switches the trapping beams on and off, and turns down the power for the PG setting. The overall detunings thus achieved are about -7 MHz for the MOT, and -35.5 MHz for PG cooling. Note that all the frequency tuning is done on the injection beam, whereas all the power adjustments are made on the slave's output beam.

It is convenient to monitor the slave's saturated absorption signal while scanning the master's piezo across the Cesium transition. A locked slave will track along with the master, hence a clean absorption signal from the slave is a good indication that locking has been achieved. Another useful monitor for the lock is a beatnote between the master and its slave, which is significantly narrower and higher up above the noise floor when the slave is locked, as opposed to free-running.

A small fraction of the slave's light is used for the lattice beams' $F = 4 \rightarrow F' = 4'$ component. Specifically, we pick off some light before AOM #2, and put it through a third AOM (not shown in the figure) downshifting by 344 MHz, which for the MOT setting of AOM #1 leads to a blue detuning of $+10$ MHz from $4 \rightarrow 4'$.

Replacing the light source for the MOT and side beams was done while maintaining their alignment at the vacuum chamber, hence with a minimum of down time for the experiment. This was made possible by the fact that the MOT light source on the one hand, and the beams at the chamber on the other, are decoupled from one another by single-mode fibers. Thus our MOT setup comes close to being ideal as far as robustness and easy upgradability. The one improvement I would suggest for the future would be to couple the repumper into the fiber that delivers the trapping

light to the chamber, thus eliminating the now-frequent problem of MOT-repumper misalignment.

Bibliography

[1] J. McKeever. *Trapped atoms in cavity QED for quantum optics and quantum information; http://etd.caltech.edu/etd/available/etd-06032004-163753/.* PhD thesis, California Institute of Technology, 2004.

[2] J. McKeever, J. R. Buck, A. D. Boozer, A. Kuzmich, H.-C. Nägerl, D. M. Stamper-Kurn, and H. J. Kimble. State-insensitive cooling and trapping of single atoms in an optical cavity. *Phys. Rev. Lett.*, 90:133602, 2003.

[3] J. McKeever, J. R. Buck, A. D. Boozer, and H. J. Kimble. Determination of the number of atoms trapped in an optical cavity. *Phys. Rev. Lett.*, 93:143601, 2004.

[4] J. McKeever, A. Boca, A. D. Boozer, J. R. Buck, and H. J. Kimble. Experimental realization of a one atom laser in the regime of strong coupling. *Nature*, 425:268, 2003.

[5] J. McKeever, A. Boca, A. D. Boozer, R. Miller, J. R. Buck, A. Kuzmich, and H. J. Kimble. Deterministic generation of single photons from one atom trapped in a cavity. *Science*, 303:1992, 2004.

[6] A. D. Boozer. *Raman transitions in cavity QED*. PhD thesis, California Institute of Technology, 2005.

[7] A. Boca, R. Miller, K. M. Birnbaum, A. D. Boozer, J. McKeever, and H. J. Kimble. Observation of the vacuum Rabi spectrum for one trapped atom. *Phys. Rev. Lett.*, 93:233603, 2004.

[8] K. M. Birnbaum, A. Boca, R. Miller, A. D. Boozer, T. E. Northup, and H. J. Kimble. Photon blockade in an optical cavity with one trapped atom. *Nature*, 2005.

[9] K. M. Birnbaum. *Cavity QED with multilevel atoms.* PhD thesis, California Institute of Technology, 2005.

[10] L.-M. Duan and H. J. Kimble. Scalable photonic quantum computation through cavity-assisted interactions. *Phys. Rev. Lett.*, 92:127902, 2004.

[11] J. I. Cirac, P. Zoller, H. J. Kimble, and H. Mabuchi. Quantum state transfer and entanglement distribution among distant nodes in a quantum network. *Phys. Rev. Lett.*, 78:3221, 1997.

[12] H.-J. Briegel, S. J. van Enk, J. I. Cirac, and P. Zoller. Quantum networks I: Entangling particles at separate locations. In D. Bouwmeester, A. Ekert, and A. Zeilinger, editors, *The Physics of Quantum Information*, page 192. Springer-Verlag, Berlin, 2000.

[13] E. T. Jaynes and F. W. Cummings. Comparison of quantum and semiclassical radiation theories with application to the beam maser. *Proc. IEEE*, 51:89, 1963.

[14] H. Carmichael. *An open systems approach to quantum optics.* Springer-Verlag, Berlin, 1993.

[15] D. Boiron, A. Michaud, P. Lemonde, Y. Castin, and C. Salomon. Laser cooling of cesium atoms in gray optical molasses down to 1.1 μK. *Phys. Rev. A*, 53:R3734, 1996.

[16] H. J. Kimble. Strong interactions of single atoms and photons in cavity QED. *Physica Scripta*, T76:127, 1998.

[17] J. J. Sanchez-Mondragon, N. B. Narozhny, and J. H. Eberly. Theory of spontaneous-emission line shape in an ideal cavity. *Phys. Rev. Lett.*, 51:550, 1983.

[18] G. S. Agarwal. Vacuum-field Rabi splittings in microwave absorption by Rydberg atoms in a cavity. *Phys. Rev. Lett.*, 53:1732, 1984.

[19] T. Pellizzari, S. A. Gardiner, J. I. Cirac, and P. Zoller. Decoherence, continuous observation, and quantum computing: A cavity QED model. *Phys. Rev. Lett.*, 75:3788, 1995.

[20] H. Mabuchi and A. C. Doherty. Cavity quantum electrodynamics: Coherence in context. *Science*, 298:1372, 2002.

[21] P. Berman, editor. *Cavity Quantum Electrodynamics*. Academic Press, San Diego, 1994.

[22] R. J. Thompson, G. Rempe, and H. J. Kimble. Observation of normal-mode splitting for an atom in an optical cavity. *Phys. Rev. Lett.*, 68:1132, 1992.

[23] J. J. Childs, K. An, M. S. Otteson, R. R. Dasari, and M. S. Feld. Normal-mode line shapes for atoms in standing-wave optical resonators. *Phys. Rev. Lett.*, 77:2901, 1996.

[24] R. J. Thompson, Q. A. Turchette, O. Carnal, and H. J. Kimble. Nonlinear spectroscopy in the strong-coupling regime of cavity QED. *Phys. Rev. A*, 57:3084, 1998.

[25] M. Brune, F. Schmidt-Kaler, A. Maali, J. Dreyer, E. Hagley, J. M. Raimond, and S. Haroche. Quantum Rabi oscillation: A direct test of field quantization in a cavity. *Phys. Rev. Lett.*, 76:1800, 1996.

[26] C. J. Hood, M. S. Chapman, T. W. Lynn, and H. J. Kimble. Real-time cavity QED with single atoms. *Phys. Rev. Lett.*, 80:4157, 1998.

[27] J. Ye, D. W. Vernooy, and H. J. Kimble. Trapping of single atoms in cavity QED. *Phys. Rev. Lett.*, 83:4987, 1999.

[28] P. Maunz, T. Puppe, I. Schuster, N. Syassen, P. W. H. Pinkse, and G. Rempe. Normal-mode spectroscopy of a single bound atom-cavity system. *quant-ph/0406136*, 2004.

[29] M. Riebe, H. Haeffner, C. F. Roos, W. Haensel, J. Benhelm, G. P. T. Lancaster, T. W. Koerber, C. Becher, F. Schmidt-Kaler, D. F. V. James, and R. Blatt. Deterministic quantum teleportation with atoms. *Nature*, 429:734, 2004.

[30] M. D. Barrett, J. Chiaverini, T. Schaetz, J. Britton, W. M. Itano, J. D. Jost, E. Knill, C. Langer, D. Leibfried, R. Ozeri, and D. J. Wineland. Deterministic quantum teleportation of atomic qubits. *Nature*, 429:737, 2004.

[31] A. Wallraff, D. I. Schuster, A. Blais, L. Frunzio, R.-S. Huang, J. Majer, S. Kumar, S. M. Girvin, and R. J. Schoelkopf. Strong coupling of a single photon to a superconducting qubit using circuit quantum electrodynamics. *Nature*, 431:162, 2004.

[32] I. Chiorescu, P. Bertet, K. Semba, Y. Nakamura, C. J. P. M. Harmans, and J. E. Mooij. Coherent dynamics of a flux qubit coupled to a harmonic oscillator. *Nature*, 431:159, 2004.

[33] K. L. Corwin, S. J. M. Kuppens, D. Cho, and C. E. Wieman. Spin-polarized atoms in a circularly polarized optical dipole trap. *Phys. Rev. Lett.*, 83:1311, 1999.

[34] L. Mandel and E. Wolf. *Optical Coherence and Quantum Optics*. Cambridge Univ. Press, Cambridge, 1995.

[35] H. J. Carmichael, R. J. Brecha, and P. R. Rice. Quantum interference and collapse of the wavefunction in cavity QED. *Opt. Comm.*, 82:73, 1991.

[36] R. J. Brecha, P. R. Rice, and M. Xiao. N two-level atoms in a driven optical cavity: Quantum dynamics of forward photon scattering for weak incident fields. *Phys. Rev. A*, 59:2392, 1999.

[37] Wolfram Research, Inc. *Mathematica 5.0.* Champaign, IL, 2003.

[38] The MathWorks, Inc. *Matlab 6.5.* Natick, MA, 2002.

[39] S. M. Tan. A computational toolbox for quantum and atomic optics. *J. Opt. B*, 1:424, 1999.

[40] P. Bevington and D. K. Robinson. *Data Reduction and Error Analysis for the Physical Sciences.* McGraw-Hill, New York, NY, 2002.

[41] J. Altmann. *Jens' file editor, and GNU C compiler.* Massey University, Albany, New Zealand, 1999.

[42] B. W. Kernighan and D. M. Ritchie. *The C programming language.* Prentice Hall, Englewood Cliffs, NJ, 1988.

[43] T. A. Fulton and G. J. Dolan. Observation of single-electron charging effects in small tunnel junctions. *Phys. Rev. Lett.*, 59:109, 1987.

[44] M. A. Kastner. The single-electron transistor. *Rev. Mod. Phys.*, 64:849, 1992.

[45] A. Imamoḡlu, H. Schmidt, G. Woods, and M. Deutsch. Strongly interacting photons in a nonlinear cavity. *Phys. Rev. Lett.*, 79:1467, 1997.

[46] P. Grangier, D. F. Walls, and K. M. Gheri. Comment on "Strongly interacting photons in a nonlinear cavity". *Phys. Rev. Lett.*, 81:2833, 1998.

[47] M. J. Werner and A. Imamoḡlu. Photon-photon interactions in cavity electromagnetically induced transparency. *Phys. Rev. A*, 61:011801, 1999.

[48] S. Rebić, S. M. Tan, A. S. Parkins, and D. F. Walls. Large kerr nonlinearity with a single atom. *J. Opt. B*, 1:490, 1999.

[49] S. Rebić, A. S. Parkins, and S. M. Tan. Polariton analysis of a four-level atom strongly coupled to a cavity mode. *Phys. Rev. A*, 65:043806, 2002.

[50] J. Kim, O. Bensen, H. Kan, and Y. Yamamoto. A single-photon turnstile device. *Nature*, 397:500, 1999.

[51] I. I. Smolyaninov, A. V. Zayats, A. Gungor, and C. C. Davis. Single-photon tunneling via localized surface plasmons. *Phys. Rev. Lett.*, 88:187402, 2002.

[52] S. Rebìc, A. S. Parkins, and S. M. Tan. Photon statistics of a single-atom intracavity system involving electromagnetically induced transparency. *Phys. Rev. A.*, 65:063804, 2002.

[53] C. J. Hood. *Real-time Measurement and Trapping of Single Atoms by Single Photons.* PhD thesis, California Institute of Technology, 2000.

[54] L. Tian and H. J. Carmichael. Quantum trajectory simulations of two-state behavior in an optical cavity containing one atom. *Phys. Rev. A*, 46:R6801, 1992.

[55] H. J. Kimble, M. Dagenais, and L. Mandel. Photon antibunching in resonance fluorescence. *Phys. Rev. Lett.*, 39:691, 1977.

[56] H. J. Carmichael. Photon antibunching and squeezing for a single atom in a resonant cavity. *Phys. Rev. Lett.*, 55:2790, 1985.

[57] F. Diedrich and H. Walther. Nonclassical radiation of a single stored ion. *Phys. Rev. Lett.*, 58:203, 1987.

[58] K. K. Likharev. Single-electron devices and their applications. *Proc. IEEE*, 87:606, 1999.

[59] A. E. Siegman. *Lasers.* University Science Books, Sausalito, CA, 1986.

[60] C. H. Hood, H. J. Kimble, and J. Ye. Characterization of high-finesse mirrors: Loss, phase shifts, and mode structure in an optical cavity. *Phys. Rev. A*, 64:033804, 2001.

[61] T. W. Lynn. *Measurement and control of individual quanta in cavity QED; http://etd.caltech.edu/etd/available/etd-04082003-111058/.* PhD thesis, California Institute of Technology, 2003.

[62] D. Boiron, A. Michaud, J. M. Fournier, L. Simard, M. Sprenger, G. Grynberg, and C. Salomon. Cold and dense cesium clouds in far-detuned dipole traps. *Phys. Rev. A*, 57:R4106, 1998.

[63] E. L. Raab, M. Prentiss, A. Cable, S. Chu, and D. E. Pritchard. Trapping of neutral sodium atoms with radiation pressure. *Phys. Rev. Lett.*, 59:2631, 1987.

[64] H. J. Metcalf and P. van der Straten. *Laser cooling and trapping.* Springer-Verlag, New York, 1999.

[65] A. M. Steane, M. Chowdhury, and C. J. Foot. Radiation force in the magneto-optical trap. *J. Opt. Soc. Am. B*, 9:2142, 1992.

[66] J. Dalibard and C. Cohen-Tannoudji. Laser cooling below the Doppler limit by polarization gradients: Simple theoretical models. *J. Opt. Soc. Am. B*, 6:2023, 1989.